Physikalisches Institut

University of Heidelberg

Ph.D. admission thesis

in Physics

submitted by

Jianshun Gao

born in Jilin, Jilin, China

2022

A First Two-Dimensional Magneto-Optical Trap

for Dysprosium

This Ph.D. admission thesis has been carried out by Jianshun Gao

at the

Physikalisches Institut

in

University of Heidelberg

under the supervision of

Prof. Dr. Lauriane Chomaz

Abstract

Over the past three decades, quantum gas systems have experienced rapid progression and emerged as an ideal platform for studying quantum phenomena with exquisite degrees of control. Especially, a sequence of novel many-body quantum states was discovered with Bose-Einstein Condensates (BECs) of magnetic elements. In our group in Heidelberg, a novel experimental apparatus aiming to create the BEC of Dysprosium, the most magnetic atom, is under construction. We replace the Zeeman slower with a two-dimensional magneto-optical trap (2D-MOT) as the slow atomic source, which offers a much more compact design, a potential to achieve a high cycling rate with fully optical control, and less noise introduced by the hot background atoms. In this thesis, we will review the basic theory of the atomic beam emerging from an effusion oven and the working principle of a MOT. We also introduce the experimental implementation of our setup including the mechanical design, the building of the vacuum, as well as the optical setup used for our MOTs. We then will explain the ideas of our design based on Monte-Carlo simulations of the MOT loading process, from the oven, going through the 2D-MOT, and loading into the 3D-MOT. Based on this simulation, the geometry of the collimating apertures in the oven is re-designed and the ranges of our MOT parameters are determined. Finally, the first experimental results will be presented. Up to now, 2D-MOT and 3D-MOT have been successfully achieved and optimization is ongoing.

Contents

1 | Introduction

Reaching lower temperatures is one of the most important subjects in contemporary experimental physics, since the quantum behaviors of atoms emerge and become controllable when the thermal motion is inhibited. Nowadays, after decades of extensive research laser cooling is generally used to cool atoms and molecules from room temperature to micro kelvin regime [1, 2] and even fractions of micro kelvin [3]. Combine with a further trapping and cooling mechanism, thousands of million atoms can be compressed into a small volume where a macroscopic system approaches the absolute ground state and shows the quantum behavior [4]. Such ultracold atoms offer an ideal platform to explore new quantum phenomena due to their great experimental controllability and a high degree of isolation. Plenty of new technologies have already been developed with ultracold atoms: the atomic clock is presented whose error is smaller than 1 second over the lifetime of the universe [5]; the atom interferometers can accurately measure the acceleration even potentially observing the gravity wave [6, 7]; the quantum computers can solve complex problems with a speed much higher than the classical computer [8]; the quantum memories can slow down and store the information of photon for several days [9], etc. Due to great impacts, in 1997 the Nobel Prize was awarded to laser cooling and trapping [10, 11, 12].

Behind the development of those new technologies, it is people's growing understanding of quantum phenomena. Already in the early days of quantum mechanics, fundamental theoretical works have bean devoted by pioneer physicists. In the 1920s, Albert Einstein and Satyendra Nath Bose together predicted the atoms with the integer spin follow Bose-Einstein statistics and transfer to a new quantum statistic phase, the so-called Bose-Einstein Condensate (BEC) under center critical temperature in micro-kelvin regime [13]. Shortly later, Enrico Fermi and Paul Dirac point out that the atoms with half-integer spin are governed by Fermi-Dirac statistics resulting in a quantum-degenerate Fermi gas (DFG) [14, 15]. Taking advantage of laser cooling techniques, the first BEC was achieved with rubidium and sodium in 1995 [16, 17] and won the Nobel Prize in 2001 [18, 19]. Until now, people achieve the BEC with more than ten different atom pieces, such as the atomic Hydrogen [20], all alkali metals except unstable Francium [16, 17, 21, 22, 23], the lanthanoids Dysprosium [24], Erbium [25], Thulium [26], Ytterbium [27] and Europium [28] most recently, and so on. The different elements or even different isotopes have different laser cooling scheme and interaction properties leading to different physics questions people are interested in.

In typically quantum gases at low temperatures, the isotropic and short-range

interaction dominates the properties. While the successful achievement of BECs with large magnetic dipolar elements gives us the opportunity of going beyond to the anisotropic and long-range interaction regime [29]. The first dipolar BEC was realized with Chromium (Cr) in 2005 [30], and the BEC with Dysprosium (Dy) was first realized in 2011 by the group of Benjamin L. Lev [24]. Being the most magnetic stable element, Dysprosium presents not only a tunable short-range contact interaction but also a competing isotropic long-range dipole-dipole interaction. Making use of this competition, within the last few years a sequence of novel many-body quantum states was discovered, including liquid-like droplets, droplet crystals, and most recently supersolids, a paradoxical quantum phase where both crystalline and superfluid order coexist [29]. Our new group, Quantum Fluids in Heidelberg is designing a novel compact and robust experimental set-up with the first two-dimensional magneto-optical trap (2D-MOT) for ultracold Dysprosium atoms. Additionally, combining a 3D-MOT, a crossed-beam and a tuneable accordion lattice optical trap [31] gives us a great opportunity to gain insight into the low-dimensional (2D) world of highly magnetic gases, super-solidity, and topological ordering.

The first BEC of Rubidium (Rb) captured Rb atoms directly from a near room-temperature vapor [16]. The Zeeman slower, which was firstly demonstrated in 1980s [32], was used as a pre-cooled atomic source in the first BEC experiment of Sodium (Na) [17]. Loading the MOT from a slowed atomic source not only dramatically reduces the loading time, but also largely increases the number of atoms can be loaded. Especially, the magnetic dipolar elements, such as Cr, Dy and Erbium (Er), have a melting point higher than $1000\,^\circ$C. In the ultracold experiment with those elements, the Zeeman slower always appears as a necessary part of slowed atom source. However, the 2D-MOT provides another alternative approach, which can be loaded directly from the atomic beam produced by a high-temperature oven, and provides a continuous pre-cooled atomic beam by adding another beam pushing axially. The 2D-MOT has bean first developed for Rubidium using the atoms from thermal vapor [33, 34]. With the development of laser and vacuum technology, the 2D-MOT was also used in the experiments for atom species necessitating an oven such as Lithium [35], Sodium [36], Ytterbium [37], Strontium [38]. Compared with Zeeman slower, the design with 2D-MOT is much more compact. In the configuration of experiments with 2D-MOT, The atoms in 2D-MOT are pushed into the science chamber by a laser beam, and the oven is arranged in a perpendicular direction. There is less probability for the hot atoms from the oven get into the scientific chamber introducing noise in the experiments. Besides, the laser beams in 2D-MOT also work as an optical switcher. Fully optical control of the atomic source present a potential of high cycling rate.

In this thesis, we present a novel design aiming to create a slow beam source of Dy based on a 2D MOT, that will later serve as achieving quantum degeneracy gases. Both the experimental setup and the simulation of MOT loading process, from the oven through 2D-MOT and transfer to the 3D-MOT, will be introduced. In chapter 2, we review the theory of atomic beam effusing from an oven through apertures, and the basic working principle of a MOT. In chapter 3, our experimental apparatus is

described including: the design and building of our vacuum system, including the 2D and 3D MOT chambers and oven; the magnetic-field setups; the power distribution and locking setups for our lasers; as well as the optics used for our 2D-MOT. In chapter 4, we present the Monte-Carlo simulation of the slow atomic beam source from the effusion oven to the 3D-MOT, which sheds light upon the values of critical parameters in our experiment.

2 | Theoretical Background

The first step for ultracold atom experiments is to have a reliable atomic source. One possibility is to start with an atomic oven, followed by laser-based cooling and trapping techniques designed specifically for the targeted atomic species.

The temperature and structure of the effusion oven will be defined by the melting point of the used atoms. In the case of dysprosium (Dy) and its high melting point ($> 1400\,°C$), the temperature of the effusion oven increases to above $1000\,°C$ during operation. As a result, the atoms from the oven have not only high velocities but also a broad angular distribution. A couple of additional apertures are therefore necessary to collimate the atomic beam. Furthermore, each atomic species has a different electronic shell structure, leading to different cooling transitions.

This chapter will cover the fundamental concepts of the theoretical background, including the properties of Dy, the relationship between atomic flux and aperture geometry, and the basic theory of light-atom interaction.

2.1 The Dysprosium Atom

Dysprosium is a rare-earth metal belonging to the lanthanide group. It is usually found in the form of alloy with Holmium. Despite its classification as "rare-earth metal", the abundance of dysprosium is rather high, ranking 43rd in nature [39]. However, the main challenge is isolating dysprosium from Holmium. Historically, dysprosium was first found in form of dysprosium oxides by a French chemist, Paul Émile Lecoq de Boisbaudran, in 1886 [40, 41]. The name "Dysprosium" comes from the Greek word, $\delta\upsilon\sigma\pi\rho\sigma\iota\tau\sigma c$ (dusprósitos), which literally translates to *difficult to approach* or *hard to get at*. The first pure dysprosium sample was isolated in 1950 by Frank Spedding after the development of ion-exchange techniques [42].

2.1.1 Basic properties

Dy remains solid at room temperature and has a metallic bright silver appearance. The density of Dy is $8.55\,g/cm^3$ and its melting point is $1412\,°C$ [40, 41]. It is also quite soft so that it can be easily machined. It is considered to be chemically stable; at room temperature, it does not react with dry air, but it does react with water, therefore it will tarnish slowly in moist air and burn.

In nature, Dy has seven stable isotopes [43] shown in Tab. 2.1. Four of them have relatively similar abundances, which is of great interest in ultracold atom ex-

periments as it enables the study of different systems, e.g Bosons, Fermions, and mixtures, in the same setup. The scope of this thesis will mainly focus on ultracold bosonic ^{164}Dy samples.

Isotope	^{156}Dy	^{158}Dy	^{160}Dy	^{161}Dy	^{162}Dy	^{163}Dy	^{164}Dy
Natural Abundance	0.06%	0.1%	0.23%	18.9%	25.5%	24.9%	28.3%
Quantum Statistics	boson	boson	boson	fermion	boson	fermion	boson

Table 2.1: Stable isotopes of Dysprosium.

2.1.2 Electronic configuration

With an atomic number $Z = 66$, the ground state configuration of Dy is

$$[1s^2 2s^2 2p^6 3s^2 3p^6 3d^{10} 4s^2 4p^6 4d^1 05s^2 5p^6]_{\text{Xe}} 4f^{10} 6s^2$$

The inner shell has 54 electrons in the same structure as Xenon. The valence shell contains 10 electrons in the $4f$ orbital and 2 electrons in the $6s$ orbital. There are 7 available orbitals for 10 electrons in $4f$ orbital. According to Hund's rule, this results in three electron pairs and four single electrons. For heavy atoms, the $JJ-$coupling provides a better description than the $LS-$coupling [44]. Thus, the ground state of dysprosium has a total angular momentum $J = 8$[1], corresponding to a g-factor $g_J = 1.24$ measured in experiment [45]. The fermionic isotopes have an additional nucleus spin of $I = 5/2$.

The large electronic angular momentum defines one of the most important characteristics of Dy, as it causes it to have the largest magnetic moment $\mu \sim 10\mu_{\text{B}}$ among all elements in periodic table [44], where μ_{B} is the Bohr magneton. The magnetic moment of Dy is about 10 times larger than that of other alkali atoms, hence it is a suitable quantum gas for studying dipolar interactions in a quantum system.

2.1.3 Laser-Cooling transitions

Due to the complexity of its electronic structure, Dy has also a complex excitation spectrum. Fortunately, as shown in Fig. 2.1 two transitions can be used for laser cooling [46]:

1. The strongest broad transition at $\lambda = 421.291$ nm from the ground state $4f^{10}(^5I_8)6s^2$ to the excited state $4f^{10}(^5I_8)6s6p(^1P_1\circ)(8,1)_9\circ$. Due to its significantly high cycling rate, it is used not only in magneto-optical traps (MOTs) to achieve a large capture velocity but also in Zeeman slowing and imaging.

---

[1]Since the $6s$ is fully occupied, it does not contribute to the total angular momentum. For the ground state of ^{164}Dy, $LS-$coupling and $JJ-$coupling give the same result.

2. A narrow closed transition at $626\,\mathrm{nm}$ from the same ground state to excited state $4f^{10}(^5I_8)6s6p(^3P_1\circ)(8,1)_9\circ$ is also available in Dy. It is suitable for low-temperature MOTs, because of its narrow linewidth.

Here the terms in brackets represent the spectrum terms describing the orbital coupling. The electrons in the $4f$ orbital have a spectrum term $^5I_8(j_1 = 8)$. Both used transitions excite one electron from the $6s$ shell to the $6p$ orbital. In the so-called blue transition, the electron is excited to a singlet state $^1P_1(j_2 = 1)$. In the so-called red transition, the electron is excited to a triplet state $^3P_1(j_2' = j_2 = 1)$. Through $JJ-$coupling, the total angular momentum $J = j_1 + j_2 = 9$. In this case, this yields a spectrum term $(j_1, j_2)_J = (8, 1)_9\circ$. The symbol $\circ$ denotes an odd parity. Tab. 2.2 contains more detailed information about the blue and red transitions.
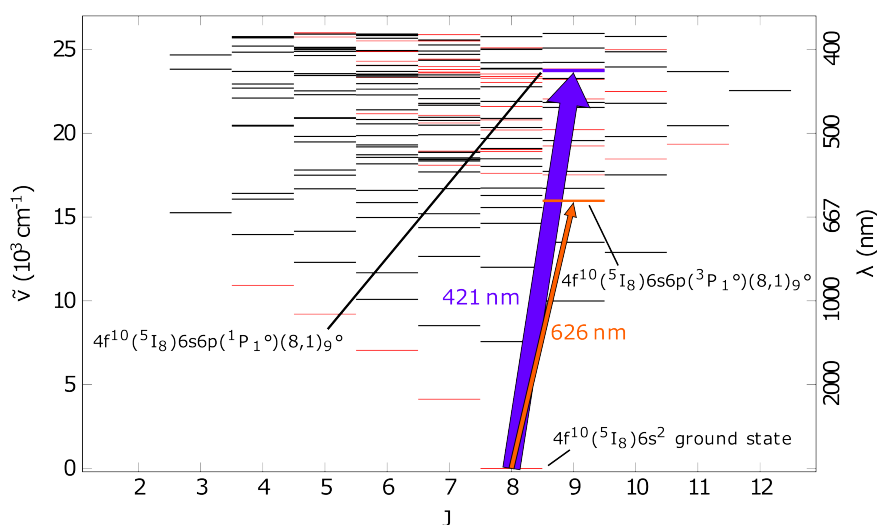
Figure 2.1: The energy levels of Dy. $\tilde{v}$ is wavenumber, λ the corresponded wavelength. Two transitions are used for laser cooling: a blue ($421\,\mathrm{nm}$) transition from ground state $4f^{10}(^5I_8)6s^2(^1P_1\circ)$ to excited state $4f^{10}(^5I_8)6s6p(^1P_1\circ)(8,1)_9\circ$; another red ($626\,\mathrm{nm}$) transition from the same ground state to excited state $4f^{10}(^5I_8)6s6p(^3P_1\circ)(8,1)_9\circ$. The term $^5I_8$, $^1P_1$ and $^3P_1$ are the spectrum terms from a $JJ-$coupling $(j_1, j_2)_J = (8, 1)_9\circ$. This figure is adapted by Joschka Schöner, a master student in our group, from Ref. [47]. P. 22.

The red transition is closed, while in the blue transition electrons can decay to the metastable states [49], as shown in Fig. 2.2. After the blue laser excites atoms f_{ex} to the excited state, there are several possible ways for the atoms to decay. In the first case, the atoms return ground state through spontaneous emission. In a second (and third), the atoms decay to metastable states at rate R_1, and further decay to ground state through a fast (slow) decay at a rate R_{fast} (R_{slow}). The rates $R_1, R_{\mathrm{fast}}, R_{\mathrm{slow}}$ of ^{164}Dy is measured by Mingwu Lu et al. [49],

$$[R_1, R_{\mathrm{fast}}, R_{\mathrm{slow}}] = [\ 1170(20),\ 19(2),\ 1.5(1)]\,\mathrm{Hz}$$

Such that the branching ratio of decaying to metastable states R_1/Γ is lower than

	Unit	421 nm	626 nm
Wavelength λ	nm	421.291	626.082
Natural linewidth Γ	$2\pi \times$ MHz	32.2	0.135
Life time τ	ns	4.94	1200
Saturation intensity I_{sat}	mW/cm^2	56.4	72×10^{-3}
g-factor of excited state $g_{J,e}$		1.22	1.29
Doppler cooling temperature limit T_{D}	µK	774	3.2

Table 2.2: Parameters related to laser cooling for Dysprosium blue (421 nm) and red (626 nm) transitions. Data from Ref. [48] and Ref. [46].

10^{-5}. In our following discussion, we consider the atoms only decay to the ground state directly through spontaneous emission.
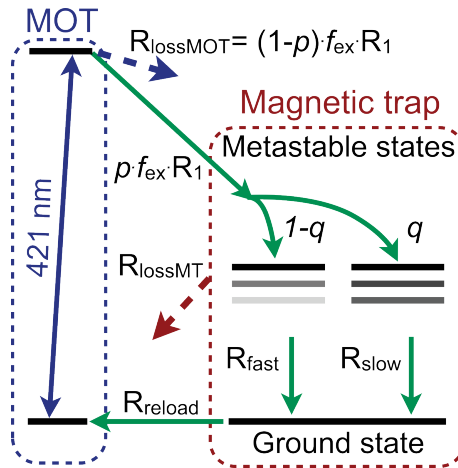
Figure 2.2: Dy MOT recycling and continuously loaded MT schematic taken from Ref. [49]. Fig. 2. (a).

2.2   Atomic Flux

In this section, we will go through the theoretical groundwork describing the physics of atoms effused from an oven through different kinds of aperture. The behavior expected from this theoretical background sets the bases for our current crucible design choices.

In many experimental cases, the so-called Zeeman-slower is the only possibility for achieving a slow atomic source. However, this design causes some unwanted effects, such as a direct light beam entering the science chamber, which causes high noise during measurements. To avoid this, our design removes the Zeeman-slower completely and instead places the oven as close as possible to a two-dimensional MOT (2D MOT). Typically, an effusion oven consists of two parts, a high-temperature

effusion cell producing atomic vapor, and a series of apertures responsible for collimating the atomic beam. In our experiment, the specific choice of slowing scheme brought us to reconsider the design of the collimation apertures. Due to the highly decreased distance between the oven and the 2D MOT, the angle from the oven towards the capture region of 2D-MOT is increased. Therefore the atoms can be loaded from a more divergent atomic beam and the atomic jet does not have to be collimated to a very small angle, in contrast to the case of the Zeeman slower. At the same oven temperature setting the 2D-MOT design can potentially achieve a higher loading rate. However, in a divergent atomic beam, most atoms are emitted from the oven under a large angle, forcing us to consider the angular distribution of atoms during the design of our oven and MOT.

2.2.1   Flow regimes

The first factor to consider is the properties of atomic gas in an effusion cell. In the effusion cell, the solid dysprosium sample is heated to above $1000\,^\circ\mathrm{C}$, but still below the melting point. Under such a high temperature and in a vacuum environment, a few dysprosium atoms effuse to gas phase filling effusion cell. This atomic gas in the effusion cell can be considered an ideal gas due to its low atomic density. Meanwhile, it is also safe to assume the sample remains in a thermal equilibrium state since only a small fraction of atoms escape or are sent back. Therefore, it follows that

$$p = k_\mathrm{B} n T, \tag{2.1}$$

where p is the pressure of Dy atomic gas, k_B the Boltzmann constant, and n the density of atoms. Surrounding by vacuum, the gradient of pressure p pushes atoms escaping from the effusion cell. The vapor pressure p is gotten from a fitting formula in Ref. [50],

$$\log p(\text{in atm}) = 9.579 - \frac{15336}{T} - 1.1114\log T. \tag{2.2}$$

At thermal equilibrium, the velocity distribution of atoms in the effusion cell obeys the 3D Maxwell-Boltzmann velocity distribution given by

$$P_\mathrm{v}(v, T) = 4\pi \left(\frac{m}{2\pi k_\mathrm{B} T} \right)^{\frac{3}{2}} v^2 \exp\left(-\frac{mv^2}{2k_\mathrm{B} T} \right). \tag{2.3}$$

The most probable velocity is $v_\mathrm{mp} = \sqrt{2k_\mathrm{B} T/m}$ and the mean velocity is $\bar{v} = 2v_\mathrm{mp}/\sqrt{\pi}$.

Additionally, the atom-atom collision plays an important role in the behavior of escaped atoms. The mean distance between two successive atom-atom collisions is defined as the mean-free-path λ,

$$\lambda_\mathrm{fp} = \frac{1}{\sqrt{2}\pi d_\mathrm{Dy}^2 n}. \tag{2.4}$$

d_Dy should be the diameter of the collision section, which is hard to define. We take the twice of Van-del Waals radius $d_\mathrm{Dy} = 281\,\mathrm{pm}$ [51] in all following calculations. In

Fig. 2.3, we show the relationship of Dy vapor pressure and mean-free-path against temperature. As the temperature increases, the vapor pressure also increases leading to a shorter mean-free-path. At $T = 1000\,^\circ$C, Dy has a mean-free-path $\lambda_{\mathrm{fp}} = 65.8\,$mm.
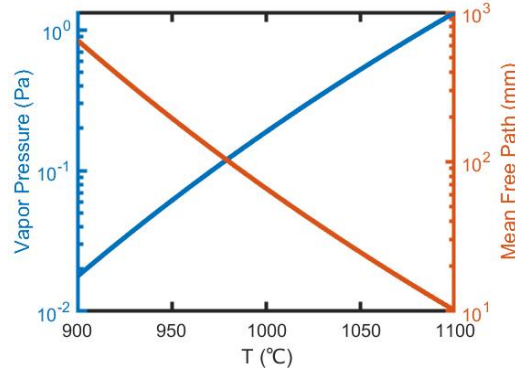

Figure 2.3: The relationship of Dy vapor pressure and mean-free-path against temperature.

Depending on the mean-free-path λ, the behavior of a flow is divided into different regime, where described by different physics models. We hereby introduce the Knudsen number K_n to scale those regimes [52], which evaluates the ratio between atom-atom collision and atom-wall collision. It is defined as,

$$K_n = \frac{\lambda_{\mathrm{fp}}}{L}. \tag{2.5}$$

L is the character length of flow. It is worthy to mention that according to specific questions L takes different physical dimension, which provides the major constrain and determines the properties of the flow. In different systems, L may represent radius or length or even something else. Tab. 2.3 shows how the Knudsen number scale those different regimes. In the this thesis, we discussion is limited in free-molecular flow regime and transitional flow regime.

Knudsen Number K_{n}	Regimes
$K_{\mathrm{n}} < 0.01$	Continuum flow
$0.01 < K_{\mathrm{n}} < 0.1$	Slip flow
$0.1 < K_{\mathrm{n}} < 10$	Transitional flow
$K_{\mathrm{n}} > 10$	Free-molecular flow

Table 2.3: Limitation of Knudsen number for different regime.

Taking an example, when we research the atomic flow rate escaping the effusion cell from a thin wall aperture, as shown in Fig. 2.4, L takes the radius of aperture r_{EC}. If r_{EC} is much larger than the mean free path, we have to take the atom-atom collision into account. In the macro-view, the flow behavior is more similar to liquid

flow, which shows viscosity. By contrast, in our case, the r_{EC} is about $\sim 1\,\text{cm}$ much smaller than the mean free path, and the atom-atom collision can be ignored. The flow behavior can be simply considered as the summation of every single atom's behavior, so it is called the free-molecular regime. The transitional regime is the regime in between, where the situation is more complex.

2.2.2 Total flow rate through a circular aperture

At this moment, let's turn our attention back to the free-molecular regime since the involved calculations are considerably less cumbersome. Usually, the effusion cell has a circular aperture with an area A. Illustrating by Fig. 2.4. (a) during a time interval $\text{d}t$, the atoms in a volume $V = A\cos(\theta)\bar{v}\,\text{d}t$ leave the effusion cell under an angle θ. Here θ is the angle atoms emerging from the effusion cell. Taking the integral of solid angle in half space, we get the formula of the flow rate leaving effusion cell Φ_{eff},

$$\Phi_{\text{eff}} = n\bar{v}A \int \cos(\theta)\frac{\text{d}\Omega}{4\pi} = \frac{1}{4}n\bar{v}A. \tag{2.6}$$
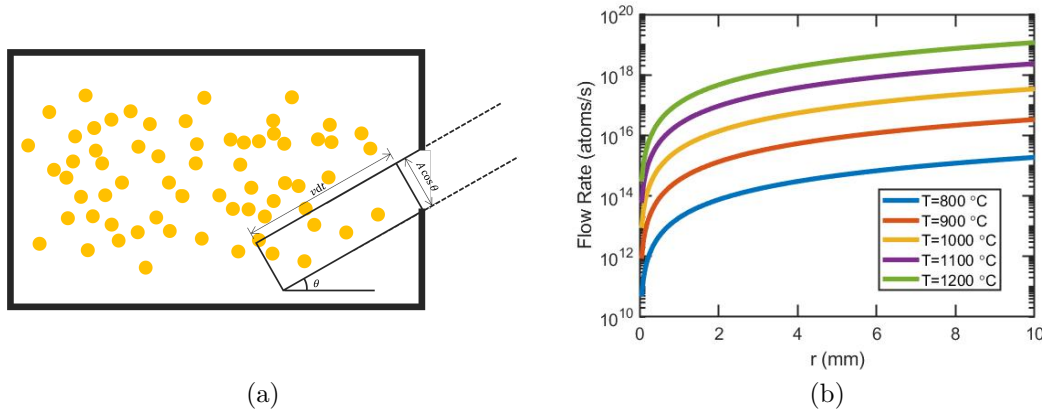
Figure 2.4: **a)** During a time interval $\text{d}t$, the atoms in a volume $V = A\cos(\theta)\bar{v}\,\text{d}t$ leave the effusion cell under an angle θ. A is the cross section area of exit, $\bar{v}$ the mean velocity of atoms in effusion cell. **b)** The atomic flow rate escaping from the effusion cell against the radius of a circular exit aperture at different temperature.

In Fig. 2.4. (b), we show the atomic flow rate escaping from the effusion cell against the exit radius at different temperatures. Agreeing with instinct, a larger exit cross area also provides a larger flow rate. Besides, the atom flow rate escaping from the effusion cell is proportional to the atomic density and average velocity in the effusion cell, which two can be both increased by increasing the temperature of the cell. So the atomic flow rate is sensitive to the temperature. We can see that with a $4\,\text{mm}$ radius of circular aperture the atomic flow rate increases about 100 times when the temperature increases from $1000\,^\circ\text{C}$ to $1200\,^\circ\text{C}$.

2.2.3 Atom-wall collision

After atoms emerge from the effusion cell, a series of apertures is used to collimator
the atomic beam. To discuss the angular distribution of the atomic beam, one should
start by understanding the effect of atom-wall collisions. We consider here such an
elementary collision: an atomic beam scatted by a metal wall, i.e. the internal wall
of an effusion cell.

At the atomic scale, it is reasonable to assume the metal surface is so rough
that atoms can be reflected in any direction, or let's say an ideal diffuse reflection
happens. A similar question for light is solved by physicist Johann Heinrich Lambert
in 1760 [53]. He proposed Lambert's cosine law to describe the intensity distribution
of light after an ideal diffuse reflection. Later, in 1909, Martin Knudsen brought his
idea into atom-wall reflection, which is then proved in experiment [54].
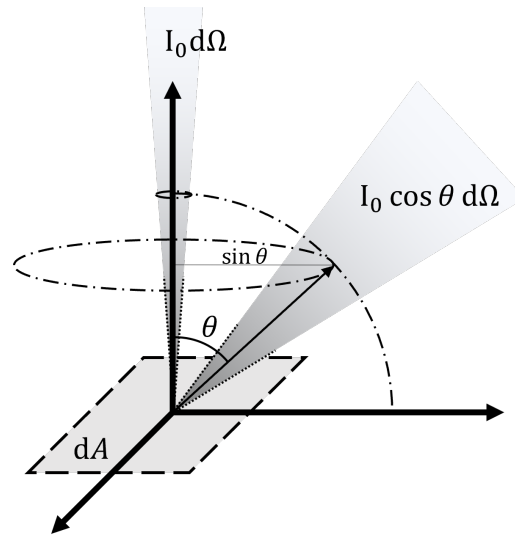
Figure 2.5: The scatted atomic beam from a surface element dA under an angle θ.

In Lambert's law, it says the scatted atomic beam is independent of the incident
beam. As shown in Fig. 2.5, if the scatted atomic beam from a surface element dA
has an intensity I_0 (atoms $\cdot$ m$^{-2}\cdot$sr^{-1}) in the direction of normal to the surface, the
reflection intensity in other directions is proportional to the cosine of reflection angel

$$I(\theta) = I_0 \cos(\theta).$$ (2.7)

And, the number of atoms $N(\theta)$ is scattered into a solid angle element $d\Omega$ at angle
θ is

$$dN(\theta) = I(\theta) \, d\Omega \, dA,$$ (2.8)

From the above information, it is easy to see that when atoms go through a metal
tube, they have an equal probability of going forward or backward after hitting on
the wall. Meanwhile, the probabilities of each scattering event get multiplied. Those
atoms experiencing much wall scattering have a very low probability of getting out

of the tube. By contrast, the atoms entering the tube with a small angle can go through the tube without any scattering. That is why a metal tube or capillary can collimate the atomic jet into the desired angle. On the other hand, it also tells us that no matter how long the tube is, it can never perfectly cut the atomic jet. There are always a few atoms coming out at even a large angle. In our experiment, An additional cold aperture is added, which can block viewports from the atomic jet.

Armed with the knowledge of single atom-wall collision, we will continue to answer the angular distribution of the atomic beam. In this thesis, only central-symmetric apertures are involved, i.e. circular thin-wall aperture and tubed aperture. Because the angular distribution is sensitive to the atom-atom collision, the situations in the free-molecular flow regime and transitional flow regime are different. The following derivations are largely taken from Ref. [55].

2.2.4 Angular distribution in the free-molecular regime

In the free-molecular flow regime, the basic assumptions in the model are following:

1. The atom-wall collision follows Lambert's cosine law

2. Marked the radius of aperture as r and length as L. The atom-wall collision rate, $v(z)$ at a distance from the entrance, is approximated to be linearly decreasing with L

$$v(z) = v_0 \left[\xi_1 - (\xi_1 - \xi_0) \frac{z}{L} \right], \tag{2.9}$$

where $\xi_0 = \alpha(\beta)$, $\xi_1 = 1 - \alpha(\beta)$, v_0 is the flow rate of atom beam entering per unit area of aperture. The two factors α and β only depend on the aperture geometry,

$$\beta = \frac{2r}{L}, \tag{2.10}$$

$$\alpha = \frac{1}{2} - \frac{1}{3\beta^2} \left(\frac{1 - 2\beta^3 + (2\beta^2 - 1)\sqrt{1 + \beta^2}}{\sqrt{1 + \beta^2} - \beta^2 \mathrm{arcsinh}(\beta^{-2})} \right). \tag{2.11}$$

It can be divided into two different regimes: the atoms going through without any collision, or the atoms hitting the wall at least one time. Since the atom-atom interaction is ignored, the regimes are only determined by the incident angle of atoms θ and aperture geometry β. Here we introduce a parameter $q = \beta \tan(\theta)$. If the atoms come with a small angle, where $q < 1$, they can travel through the aperture collision-free. In the second, if $q \geq 1$, the atoms will strike the wall at least once. With this parameter, the angular distribution of atoms emerging from the

aperture is

$$
j\left(\theta\right) =
\begin{cases}
\begin{aligned}
&\alpha\cos\left(\theta\right) + \frac{2}{\pi}\cos\left(\theta\right)\left(1-\alpha\right)R\left(q\right)\\
&\quad + \frac{2}{3q}\cos\left(\theta\right)\left(1-2\alpha\right)\left(1-\sqrt{\left(1-q^2\right)^3}\right),
\end{aligned} & \text{if } q < 1.\\[2em]
\alpha\cos\left(\theta\right) + \frac{4}{3\pi q}\cos\left(\theta\right), & \text{if } q \geq 1.
\end{cases}
\tag{2.12}
$$

where

$$
R(q) = \arccos(q) - q\sqrt{1-q^2}. \tag{2.13}
$$

The above result is calculated in Ref. [55]. Here $j(\theta)$ has a physical meaning that the probability of an atom emitting into a solid angle at a polar angle θ from the aperture axis from a unit aperture area. The central line intensity is a constant, $j(0) = 1$, since no matter how the aperture change, those atoms never collide with the wall. Since $j(\theta)$ is the probability distribution function, it must be normalized,

$$
N_j \int j(\theta)\,\mathrm{d}\Omega = 1, \tag{2.14}
$$

The normalization constant N_j of $j(\theta)$ is given by the case of thin-wall aperture. From the previous discussion on the flux leaving effusion cell in section 2.2.2, we can easily derive that $j(\theta) = \cos\theta$ for an ideal circular thin-wall aperture (aperture without thickness). Thus,

$$
N_j \int j(\theta)\,\mathrm{d}\Omega = N_j \int_0^{2\pi} d\phi \int_0^{\frac{\pi}{2}} \cos(\theta)\sin(\theta)\,\mathrm{d}\theta = 1, \tag{2.15}
$$

which leads to $N_j = 1/\pi$. The integral of $j(\theta)$ gives the probability of atoms traveling through the aperture, also known as Clausing factor W,

$$
\begin{aligned}
W &= \frac{1}{\pi}\int j(\theta)d\Omega\\
&= 1 + \frac{2}{3}(1-2\alpha)(\beta - \sqrt{1+\beta^2}) + \frac{2}{3}(1+\alpha)(1-\sqrt{1+\beta^2}).
\end{aligned}
\tag{2.16}
$$

Furthermore, it is noticed that $j(\theta)$ only involves the aperture geometry factor α and β. The other factors, such as temperature or pressure, do not contribute to the angular distribution in the free-molecular flow regime, which suggests that aperture geometry is the first thing that we need to be taken into account during oven designing. Fig. 2.6 (b) shows the angular distribution for apertures with different geometry. As β increases, the angular distribution becomes broader and broader, until at $\beta = \infty$, it recovers the cosine distribution expected from the situation of thin-wall aperture. Although the maximal atomic intensity coming out of the aperture, which is given by $j(\theta)$, is obtained at $\theta = 0$, the maximal number of emerging atoms is obtained with a small non-zero angle. This is due to the fact that the area

decreases with θ (as $\sin\theta$), as shown in Fig. 2.5. A small θ corresponds to a small area, especially at $\theta = 0$ the area is infinitely small. From this view, shortening the distance between the oven and MOT, which increases the angle from the oven towards the capture region of MOT, presents a huge potential for increasing the loading rate.
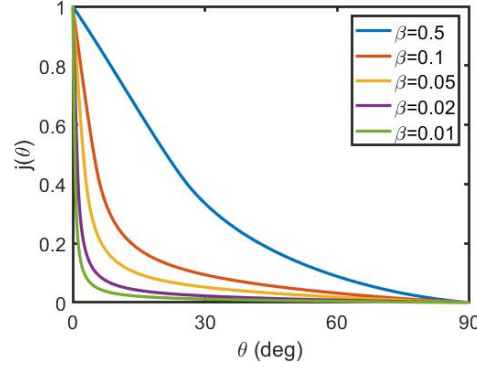

Figure 2.6: The angular distribution $j(\theta)$ in free-molecular regime with different aperture geometry factor β.

2.2.5 Angular distribution in the transition regime

Based on the knowledge of angular distribution in the free-molecular flow regime, we now are able to solve the angular distribution in the transition flow regime. As in the free-molecular flow regime, we still assume that atom-wall collision follows Lambert's cosine law. However, due to the appearance of atom-atom collision, the atom-wall collision rate $v(z)$ is no longer sufficient to determine the angular distribution. Instead, the atom-atom collision rate plays an important role, mainly determined by the atomic density profile $n(z)$ in the aperture. it is assumed to have the same linear form,

$$n(z) = n_s\left[\zeta_1 - (\zeta_1 - \zeta_0)\frac{z}{L}\right], \tag{2.17}$$

with n_s the atomic density at the entrance. Supported by experiment result, we can make the approximation $\zeta_i \approx \xi_i$ [56]. Again the explicit solution of angular is given by Ref. [55] based on Ref. [56],

$$j(\theta, T) = \begin{cases} \dfrac{2}{\sqrt{\pi}}\zeta_0\cos(\theta)\dfrac{e^{\delta^2}}{\delta} \\ \times\left[\dfrac{R(q)}{2}\left(\mathrm{erf}\left(\delta\dfrac{\zeta_1}{\zeta_0}\right) - \mathrm{erf}(\delta) + F(\zeta_0, \zeta_1, \delta)\right) + S(q)\right] & \text{if q} < 1. \\ + \zeta_0\cos(\theta), \\[2em] \zeta_0\cos(\theta) + \frac{2}{\sqrt{\pi}}\zeta_0\cos(\theta)\frac{e^{\delta^2}}{\delta}S(1), & \text{if q} \geq 1. \end{cases} \tag{2.18}$$

where,

$$S(q) = \int_0^q \sqrt{1 - t^2} \left[\text{erf}\left(\delta \left(1 + \frac{t(\zeta_1 - \zeta_0)}{q\zeta_0} \right) \right) - \text{erf}(\delta) \right], \tag{2.19}$$

$$F(\zeta_0, \zeta_1, \delta) = \frac{2}{\sqrt{\pi}} \delta \frac{1 - \zeta_1}{\zeta_0} e^{-\left(\frac{\delta \zeta_1}{\zeta_0} \right)^2}, \tag{2.20}$$

$$\delta = \frac{\zeta_0}{\sqrt{2 K_n (\zeta_1 - \zeta_0) \cos(\theta)}}. \tag{2.21}$$

Unlike the situation in the free-molecular flow regime, the angular distribution $j(\theta)$ depends on the temperature-related Knudsen number. Besides, $j(0)$ is no longer a constant, yet the normalization factor N_j in Equ. (2.14) doesn't change, since the $j(\theta)$ keeps the same physical meaning.

Fig. 2.7 reports the angular distribution in transitional flow regime. In the plots (a) and (b), $j(\theta)$ is renormalized by $j(0) = 1$ providing convenience for comparing. Fig. 2.7. (a) shows the angular distribution in transitional flow regime with different aperture geometry at temperature $T = 1000\,°\text{C}$. As same as in the free-molecular regime, a larger β (a shorter length or larger radius) makes the angular distribution broader. Fig. 2.7. (b) shows the angular distribution in the transitional flow regime with different temperatures at $\beta = 0.87$, where a higher temperature broadens the angular distribution. Additionally, as shown in Fig. 2.7. (c), $j(0)$ also decreases as temperature increasing. It means a higher temperature decreases the probability of atoms traveling through the aperture (the Clausing factor W decreases), due to the increasing atom-atom collision rate. If we let $T \to 0$ in Euq.(2.18), the angular distribution return to the same situation in free-molecular regime. Meanwhile, a higher temperature also increases the number of atoms getting into the aperture from the effusion cell. Unlike the temperature, as shown in Fig. 2.7. (c) and (d), the geometry factor β does a limited influence on the $j(0)$. Increasing β slightly decreases the $j(0)$, due to the increased atom-atom collisions. However the probability of atom-atom collisions is still limited by the low atomic density, though the atomic density is higher compared with in the free-molecular flow regime,

2.2.6   Velocity distribution

Both atom-wall collision and atom-atom collision makes a significant influence on the angular distribution. By contrast, those collisions don't change the statistical behavior of atom velocities. Therefore, we can assume the velocities of atoms traveling through a series aperture still obey the Maxwell-Boltzmann distribution. As supported by experiments, in 1970, Siekhaus et al. measured the velocity distribution along the central line of tube [57]. They found that the velocity distribution from a short tube matches the Maxwell-Boltzmann distribution, but from a long tube the slow atoms are less. And in 1975 Beijerinck and Verster measured the velocity distribution at a large angle [58]. It shows even from a long tube, at a large angle the velocity distribution turns back to the Maxwell-Boltzmann distribution. Since in our case, the atomic beam is collimated into a relatively larger angle
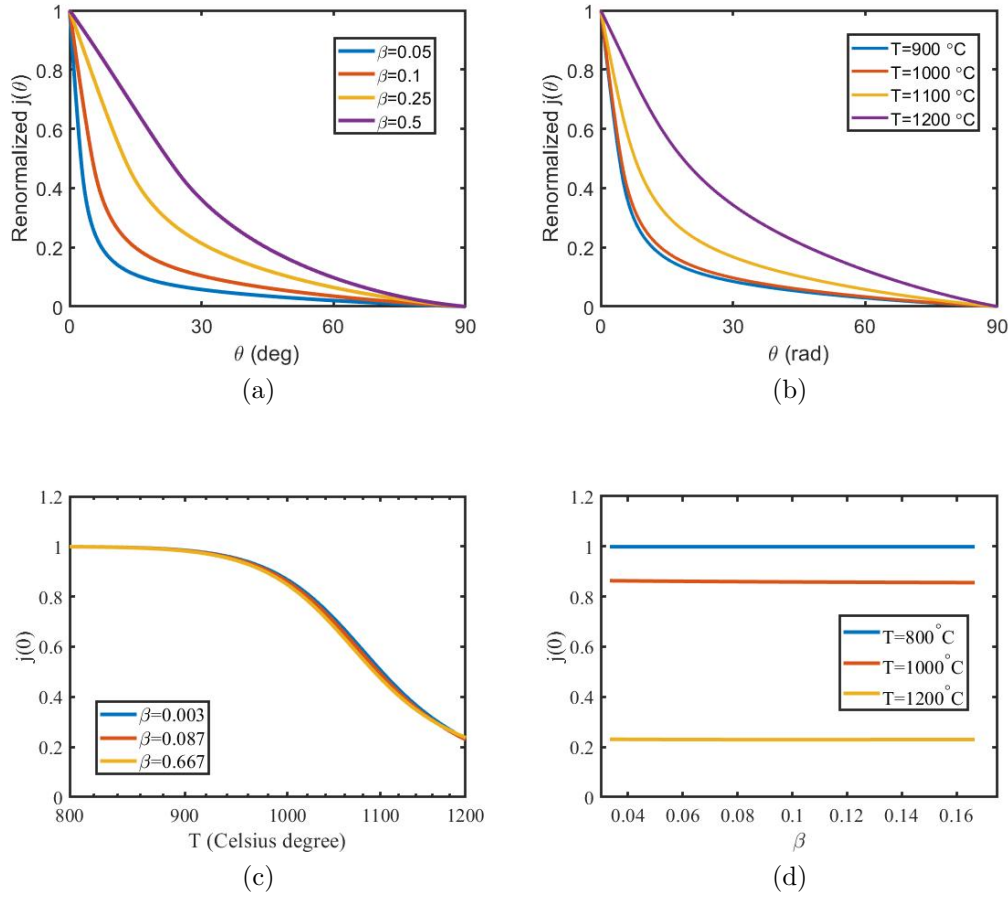
Figure 2.7: The angular distribution in transitional flow regime. **a)** with different geometry factor β at temperature $T = 1000\,°\mathrm{C}$, **b)** with different temperature at $\beta = 0.087$. $j(\theta)$ is renormalized by $j(0) = 1$. **c)** $j(0)$ against temperature with different β. **d)** $j(0)$ against β with different temperature.

($\sim 15°$), it is safe for us to take this assumption. Thus, the velocity distribution is simply taken to be the Maxwell-Boltzmann distribution.

2.2.7   Summary and conclusion

In a conclusion, we now are able to write down the explicit form for the total atomic flow rate from the oven, including the information on angular and velocity distribution,

$$\Phi_{\mathrm{Tot}}(T) = \Phi_{\mathrm{eff}}(T) \times \frac{1}{\pi} \int j(\theta, T) d\Omega \times \int P_{\mathrm{v}}(v, T)\, \mathrm{d}v. \qquad (2.22)$$

The atomic flow rate from the effusion cell $\Phi_{\mathrm{eff}}(T)$ is given by Equ. (2.6), the angular distribution $j(\theta, T)$ given by Equ. (2.12) or Equ. (2.18), the velocity distribution $P_{\mathrm{v}}(v, T)$ given by Equ. (2.3). Here, we must point out that Equ. (2.22) implies an assumption that the atomic flow rate, angular distribution, and velocity distribution

are independent of each other. The atomic flow rate is assumed to be uniform because of the large distance from the oven to the first MOT compared with the radius of apertures. The independence between angular distribution and velocity distribution is supported by experiments (see section 2.2.6 and Ref. [57, 58]). In Ch.4, we show that finally, we choose an aperture structure in the oven working in the transitional flow regime, so only Equ. (2.18) is used in the following discussion.

2.3 Light-Atom Interaction and Laser Cooling

After having introduced the physical model of atomic source, we expose the laser cooling theory for neutral atoms. Reaching extremely low temperature has been an active research topic in the past decades, as reduction of thermal excitation raises novel quantum phenomenon of atoms [3]. Laser cooling technology, which makes use of the momentum exchanging between photons and electrons around the nucleus, allows us to cool down atom and molecular gases from atomic vapor temperature, i.e. $1000\,^\circ$C for Dy, to micro-kelvin regime [49]. Meanwhile, a magnetic gradient is introduced to limit the position of atoms. Combining the cooling laser and gradient magnetic field, the magneto-optical trap (MOT) is proposed and first demonstrated in 1987 [59]. The first MOT of Dy is achieved by Benjamin L. Lev's group at the University of Illinois at Urbana-Champaign in 2010 [49]. In this section, we will briefly review the related theory of MOT cooling.

2.3.1 Optical-Bloch-Equation of two-level system

The interaction between light and atoms is always a fundamental and interesting problem in quantum mechanics. Although it is difficult to provide a full quantization description of light-atom interaction, the Optical-Bloch-Equation (ODE) [2] is an appropriate semi-classical model for laser cooling.

In the following discussion, we stay on the atomic scale, hence the complex internal structure of the atom can be ignored. The atom is approximated as a mass point with a two-level electronic structure, the ground state $|g\rangle$ and excited state $|e\rangle$. We note the energy gap between two states as $E = h\omega_{\mathrm{eg}}$, corresponding to a wavelength λ_{eg}, and the rate of spontaneous emission as Γ, also known as the natural linewidth. Defining the rising operator $\sigma^+ = |e\rangle\langle g|$ and the lowing operator $\sigma^- = |g\rangle\langle e|$, the dipole moment of atom is $\boldsymbol{d} = \langle e|\boldsymbol{r}|g\rangle(\sigma^+ + \sigma^-)$, where $\boldsymbol{r}$ is the coordinate of electron. On the other hand, in the ODE approach, the monochromatic laser field is approximated as a classical external field. It has a circular frequency $\omega_{\mathrm{L}} = 2\pi c/\lambda_{\mathrm{L}}$, and a wave-vector $k_{\mathrm{L}} = c/\omega_{\mathrm{L}}\hat{\boldsymbol{k}}$, where the unitary factor $\hat{\boldsymbol{k}}$ define the prorogation direction. Compared with the small size of atoms, the plane-wave approximation is safely introduced. The laser field is written as

$$\boldsymbol{E}(\boldsymbol{r}, t) = \boldsymbol{E}_0(\boldsymbol{r})\cos(\omega_{\mathrm{L}}t - k_{\mathrm{L}}\cdot\boldsymbol{r}), \tag{2.23}$$

with e the element charge, the Hamiltonian of this coupling system is

$$H = \hbar\omega_{\mathrm{eg}}|e\rangle\langle e| - \boldsymbol{E}(\boldsymbol{r}, t)\cdot\boldsymbol{d}. \tag{2.24}$$

Here, the first term in Hamiltonian is the energy of the atoms with excited electrons. The second term presents the interaction between atom and light. Atom-light interaction can also be expressed by Rabbi frequency $\Omega = -\boldsymbol{E}(\boldsymbol{r}, t) \cdot \boldsymbol{d}/\hbar$. We introduce the density operator ρ for simplifying the derivation,

$$\rho = \begin{pmatrix} \rho_{\text{ee}} & \rho_{\text{eg}} \\ \rho_{\text{ge}} & \rho_{\text{gg}} \end{pmatrix}, \tag{2.25}$$

where $\rho_{\text{eg}} = \rho_{\text{ge}}^*$. The atomic density matrix is governed by a Master equation,

$$\frac{d\rho}{dt} = -\frac{i}{\hbar}[H, \rho] + \left(\frac{d\rho}{dt}\right)_{\text{sp}}, \tag{2.26}$$

where the second term on the right side is a damping term contributed by spontaneous emission. The corresponding elements in the density matrix are,

$$\left(\frac{d\rho_{\text{ee}}}{dt}\right)_{\text{sp}} = -\Gamma\rho_{\text{ee}}, \quad \left(\frac{d\rho_{\text{eg}}}{dt}\right)_{\text{sp}} = -\frac{\Gamma}{2}\rho_{\text{eg}}, \quad \left(\frac{d\rho_{\text{gg}}}{dt}\right)_{\text{sp}} = \Gamma\rho_{\text{gg}}. \tag{2.27}$$

The first (last) equation describes the decay (increase) of the population of the excited (ground) state with a rate Γ, and the second equation describes the damping of the coherence between excited and ground states with a rate $\Gamma/2$.

Now the equation is solvable with Rotating Wave Approximation (RWA). In this approach, the contribution from fast dynamics is considered to be averaged, so it neglects a faster oscillation term driven by $\omega_{\text{L}} + \omega_{\text{eg}}$ in the equation. The solving procedure of this equation is well-introduced in Ref. [2]. Here we only give the important results. The population difference between excited and ground states $w \equiv \rho_{\text{ee}} - \rho_{\text{gg}}$ and the optical coherence ρ_{eg} are,

$$w = \frac{1}{1+s}, \tag{2.28}$$

$$\rho_{\text{eg}} = \frac{i\Omega}{2(1+s)\left(-\frac{\Gamma}{2} - i\Delta\right)}. \tag{2.29}$$

The detuning $\Delta \equiv \omega_{\text{L}} - \omega_{\text{eg}}$ is defined as difference between laser frequency and atomic transition frequency. Here the saturation parameter s is given by

$$s = \frac{|\Omega|^2}{2\left|\frac{\Gamma}{2} - i\Delta\right|^2} = \frac{|\Omega|^2/2}{\Delta^2 + \Gamma^2/4} = \frac{s_0}{1 + 4\left(\Delta/\Gamma\right)^2}, \tag{2.30}$$

with

$$s_0 \equiv 2\frac{|\Omega|^2}{\Gamma^2} = \frac{I}{I_{\text{sat}}}, \tag{2.31}$$

where I is the laser beam intensity, and I_{sat} is the so-called saturation intensity,

$$I_{\text{sat}} \equiv \frac{2\pi^2 \hbar c \Gamma}{3\lambda_{\text{eg}}^3}, \tag{2.32}$$

with the speed of light c. Since the population of electrons is conserved, $\rho_{\mathrm{ee}} + \rho_{\mathrm{gg}} = 1$, the population in the excited state can be calculated by

$$\rho_{\mathrm{ee}} = \frac{1}{2}(1 - w) = \frac{s}{2(1 + s)} = \frac{s_0/2}{1 + s_0 + 4(\Delta/\Gamma)^2}. \tag{2.33}$$

The population in the excited state will decay with a rate Γ because of spontaneous emission. If we keep the laser beam shining on the atom, the system will reach a dynamically balanced state, where the exaction rate equals the decay rate. Then, the total scatting rate R is given by,

$$R = \Gamma \rho_{\mathrm{ee}} = \frac{\Gamma}{2} \frac{s_0}{1 + s_0 + 4(\Delta/\Gamma)^2}. \tag{2.34}$$

The force introduced by the laser field, F, can be considered into two parts,

$$\boldsymbol{F} = \boldsymbol{F}_{\mathrm{rad}} + \boldsymbol{F}_{\mathrm{dip}}. \tag{2.35}$$

The first part is the radiation pressure $\boldsymbol{F}_{\mathrm{rad}}$ contributed by the directly momentum exchanging in absorption-spontaneous emission cycling,

$$\boldsymbol{F}_{\mathrm{rad}} = \hbar \boldsymbol{k}_{\mathrm{L}} R = \hbar \boldsymbol{k}_{\mathrm{L}} \frac{\Gamma}{2} \frac{s_0}{1 + s_0 + 4(\Delta/\Gamma)^2}. \tag{2.36}$$

Here because the photons emitted through spontaneous emission has a random direction. So the momentum taken by them is averaged out and then does not show up in Equ. (2.36). The second part is the dipole force $\boldsymbol{F}$ contributed by the power gradient of the laser field,

$$\boldsymbol{F}_{\mathrm{dip}} = -\frac{\hbar \Delta}{2} \frac{\nabla s_0}{1 + s_0 + 4(\Delta/\Gamma)^2}. \tag{2.37}$$

In the laser cooling technique, the frequency is relatively close to the transition resonance, and the intensity is relatively low that not enough to produce a strong power gradient on the atomic scale. So the radiation pressure $\boldsymbol{F}_{\mathrm{rad}}$ is dominant comparing with the dipole force $\boldsymbol{F}_{\mathrm{dip}}$. In all our following discussions, we only consider the radiation pressure.

2.3.2   Optical molasses

From the discussion on the radiation pressure in the last section, we know an on-resonance laser beam can provide a force acting on atoms. Simply adding a counter-propagating beam, a so-called optical molasses setup can be built for slowing down atoms from random thermal movements.

Let us consider the simplest one-dimension (1D) case. Two counter-propagating beams act on a moving atom. When the saturation parameter $s \ll 1^2$, an approximation is made: the total force equals the summation of the force provided by each

---

[2]In our case, especially for the red 3D-MOT, the saturation parameter does not really satisfy this condition. But it still provides a good theoretical model to find the optimized MOT parameters in simulation.

beam [60],

$$\boldsymbol{F}_{\text{tot}} = \sum_i \boldsymbol{F}_i = \hbar \boldsymbol{k}_i \frac{\Gamma}{2} \frac{s_i}{1 + \sum_i s_i}, \tag{2.38}$$

where $\boldsymbol{k}_i$ is wave vector of each beam, s_i the saturation parameter of each beam give by Equ. 2.30. Although we limit our discussion in 1D, Equ. (2.38) also holds for higher dimensional situations.

We know that when a laser beam shines on an atom with velocity v, the frequency will be shifted by the Doppler effect. Thus, the detuning of each beam should be written as[3]

$$\Delta_i = \Delta_{\text{L}} + \boldsymbol{k}_i \cdot \boldsymbol{v}, \tag{2.39}$$

with the initial detuning between laser bean and atom transition $\Delta_{\text{L}} = \omega_{\text{L}} - \omega_{\text{eg}}$. Fig. 2.8 shows the force acting on atoms with different velocities. When there is only one laser beam against the atom moving, the force has a Lorentzian shape. The peak locates at the $\Delta_{\text{L}} + \boldsymbol{k}_i \cdot \boldsymbol{v} = 0$. After adding another counter-propagating beam, we can see that in the region $\boldsymbol{k}_i \cdot \boldsymbol{v} < 0$, the total force always has a positive value, which accelerates the atom. While in the region $\boldsymbol{k}_i \cdot \boldsymbol{v} > 0$, the total force always has a negative value, which decelerates the atom. Thus, finally, atom velocity will be damped down close to 0.
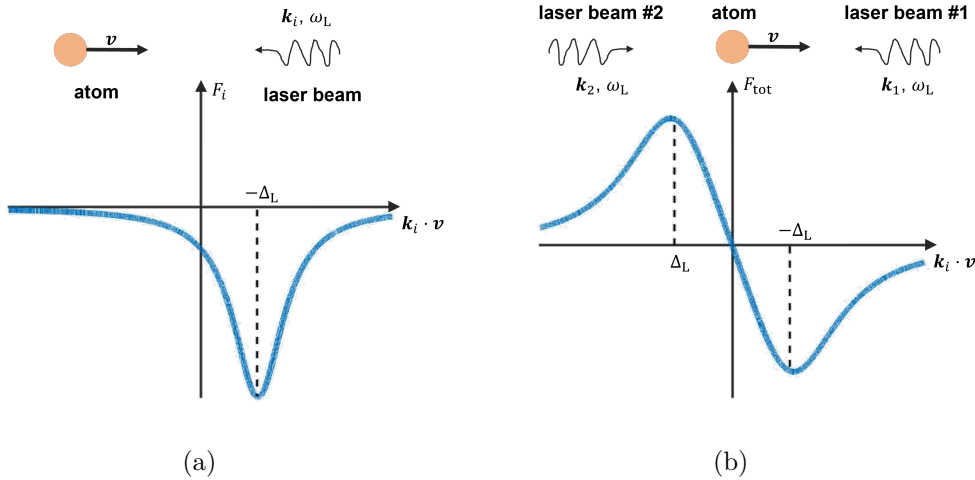

(a)   (b)

Figure 2.8: The force acting on the atom in a 1D optical molasses. **a)** with one laser beam against atom velocity. **b)** two counter-propagating beams. The $x-$axis is the frequency shift $\boldsymbol{k}_i \cdot \boldsymbol{v}$, $\Delta_{\text{L}} = \omega_{\text{L}} - \omega_{\text{eg}}$ the initial detuning between laser bean and atom transition, $\boldsymbol{k}_i$ the wave vector, ω_{L} laser frequency. The force provided by spontaneous emission scatting is ignored.

However, minimal velocity can never reach 0 due to spontaneous emission. Whenever a photon is emitted through spontaneous emission, the atom will gain some

---

[3]In some other reference, readers can find this formula is written with $\pm$ symbol. Here to make the formula more concise, we allow the velocity to take a negative value, which means the atom moving against laser propagation.

momentum in a random direction. Although the average contribution is 0, spontaneous emissions do contribute to a fluctuation in momentum. Considering in a small time duration Δt, the number of absorption-spontaneous emission cycling N_s is

$$N_s = R\Delta t = \frac{\Gamma}{2}\sum_i \frac{s_i}{1 + \sum_i s_i}\Delta t. \tag{2.40}$$

Then the recoil heating can be estimated by [61, 62],

$$\Delta \boldsymbol{p} = \hbar \boldsymbol{k}_L \sqrt{N_s}\hat{\boldsymbol{e}}, \tag{2.41}$$

where $\hat{\boldsymbol{e}}$ is a unit vector with random direction. The minimal achievable temperature is called Doppler temperature T_D [61],

$$T_D = \frac{\hbar}{2k_B}\Gamma. \tag{2.42}$$

The Doppler temperature of 421 nm and 626 nm transition are given in Tab. 2.2.

2.3.3   Magneto-optical trap

We now can successfully slow down the atoms, by using optical molasses. However, there is no limitation on the atom positions. The atoms can literally stop anywhere. In order to avoid that, we must introduce a position-dependency term in laser cooling. This can be done by taking advantage of the Zeeman effect.

The degeneracy Zeeman sub-levels are separated by introducing an external magnetic gradient in the configuration of optical molasses, as shown in Fig. 2.9. An external magnetic field $\boldsymbol{B} = b\boldsymbol{x}$ is applied along $x-$axis in optical molasses. b, the gradient of the magnetic field, is a constant. The laser frequency has a red detuning Δ_L from the transition. The two counter-propagating beams must be circular polarized. A σ^+ polarized beam comes from the left side, and another σ^- polarized beam comes from the right side. Normally the σ^+ and σ^- polarization is defined according to the direction of the local magnetic field. But here they are defined according to the direction of $x-$axis since the magnetic field changes direction at $x = 0$. The two counter-propagating beams actually have the same handedness of polarization. In Fig. 2.9, they are both right-handed circular polarized. Because of the conservation of angular momentum, σ^+ (σ^-) polarized photon can only drive a transition from $\Delta m_J = +1(\Delta m_J = -1)$. From the figure, we can directly see that in the region $x < 0$, σ^+ beam has a smaller detuning. According to Equ. (2.38) and Equ. (2.30) a smaller detuning leads to a larger force. Thus, in the region $x < 0$, the atom experience a total force towards the right side. By contrast, in the region $x > 0$, σ^- beam has a smaller detuning resulting in a total force towards the left side. Thus, the atoms can be trapped at the position $x = 0$.

The energy shifts of Zeeman sub-levels is given by [63],
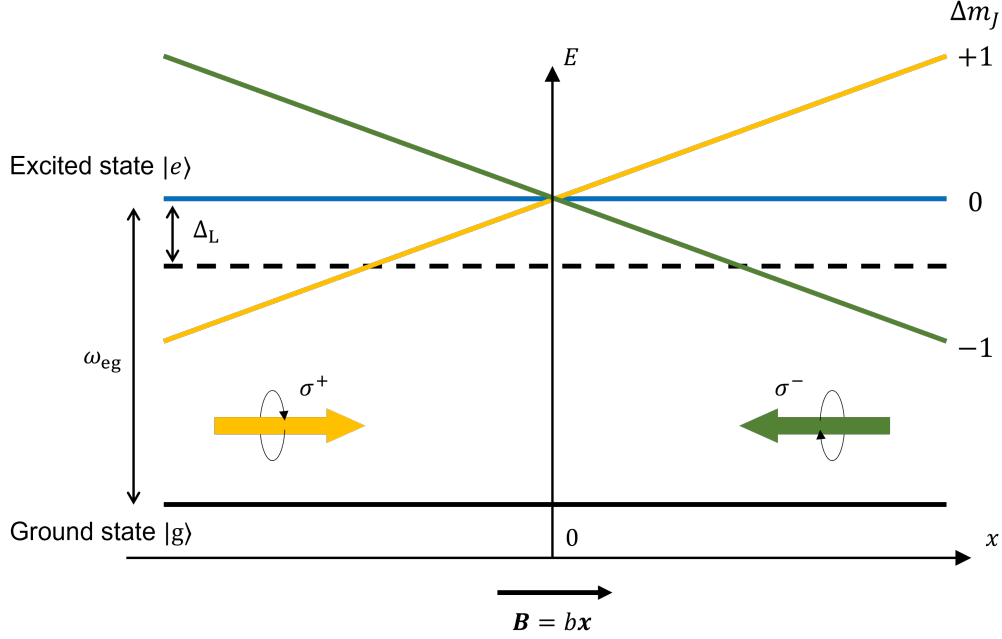
$$\Delta E = g_J m_J \mu_B |\boldsymbol{B}|. \tag{2.43}$$

Figure 2.9: Zeeman sub-levels in a MOT as a function of atom position z. m_F is the magnetic quantum number of atoms, Δ_L the detuning of laser frequency.Only two states, the ground state and excited state, are shown in the figure. Because of the conservation of angular momentum, σ^+ (σ^-) polarized photon can only drive a transition from $\Delta m_J = +1(\Delta m_J = -1)$.

with g_J the Landé factor, $\mu_B = 9.274 \times 10^{-24}$ J/T the Born magneton. Therefore, the detuning of a beam in MOT can be written as[4],

$$\Delta_i = \Delta_L + \boldsymbol{k}_i \cdot \boldsymbol{v} + \frac{\mu_B}{\hbar}(g_{J,e}m_{J,e} - g_{J,g}m_{J,g})\mathrm{sgn}\left(\boldsymbol{B} \cdot \boldsymbol{k}_i\right)|\boldsymbol{B}| \qquad (2.44)$$

where $g_{J,i}$ and $m_{J,i}, (i = e, g)$ are respectively the Landé factor and magnetic quantum number of the excited or ground state, and the $\mathrm{sgn}(x)$ is the sign function returning the sign of x,

$$\mathrm{sgn}(x) = \begin{cases} +1, & \text{if } x > 1. \\ 0, & \text{if } x = 0. \\ -1, & \text{if } x < 1. \end{cases} \qquad (2.45)$$

For ^{164}Dy, the difference between $g_{J,e}$ and $g_{J,g}$ is smaller than 5% of $g_{J,e}$, so we have the approximation,

$$g_{J,e}m_{J,e} - g_{J,g}m_{J,g} \approx (m_{J,e} - m_{J,g})g_{J,e}. \qquad (2.46)$$

Finally, the Equ. (2.38), Equ. (2.30) and Equ. (2.44) give a complete solution of the force acting on the atoms trapped in a MOT.

---

[4]Again, here we write this formula in a slightly different form with other references since it treats all the terms as constants or vectors providing convenience for simulation implement.

2.3.4   MOT in higher dimensions

From the above discussion, we know how a MOT works in 1D. In practice, the MOT is used to trap the atoms in two directions (2D-MOT) or all three directions (3D-MOT). Fig. 2.9 tells us that a MOT needs magnetic gradient alone for every laser beam. Therefore, the 2D- and 3D-MOT requires different magnetic field shape. In Fig. 2.10, we give the possible solutions of magnetic field. For 2D-MOT, there are two ways. First, the desired magnetic field can be produced by permanent magnets. Four blocks of permanent magnets are shown in Fig. 2.10. (a). However, In experiments, it is impossible to put those four magnet blocks at the central plane of 2D-MOT. Those four blocks of permanent magnets are actually not at the same plane as the laser beams. In order to make the magnetic field uniform, another four blocks of permanent magnets are symmetrically placed on the other side of 2D-MOT like a sandwich. Another way is using two pairs of anti-Helmholtz coils as shown in Fig. 2.10. (b). Both permanent magnets and anti-Helmholtz coils produce the same shape of the magnetic field $\boldsymbol{B}_{2D}$,

$$\boldsymbol{B}_{2D} = b_{2D} z \hat{\boldsymbol{x}} + b_{2D} x \hat{\boldsymbol{z}}, \tag{2.47}$$

where b_{2D} is the magnetic field gradient along $x-$ or $z-$ axis, $\hat{\boldsymbol{x}}$ and $\hat{\boldsymbol{z}}$ the unit vector along $x-$ and $z-$ axis. While only one pair of anti-Helmholtz coils is needed in 3D-MOT. It produce a magnetic field $\boldsymbol{B}_{3D}$ as,

$$\boldsymbol{B}_{3D} = -b_{3D} \boldsymbol{x} - b_{3D} \boldsymbol{y} + 2 b_{3D} \boldsymbol{z}, \tag{2.48}$$
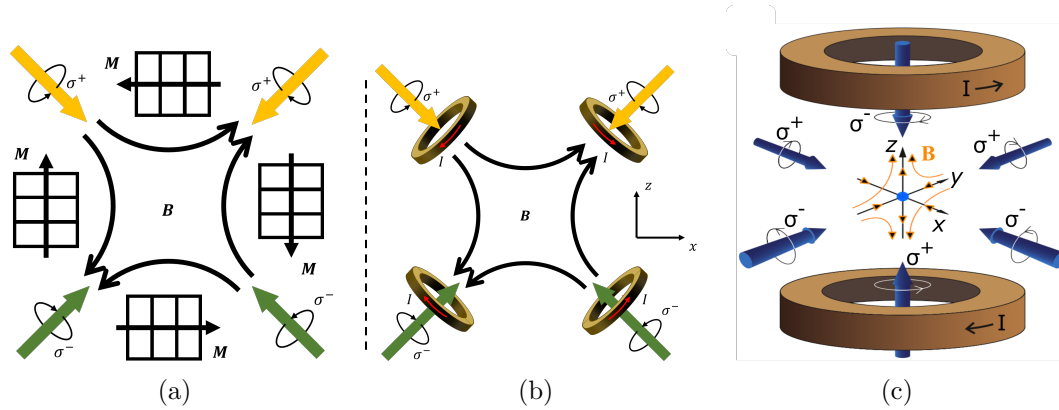

Figure 2.10: The magnetic field configuration of 2D-MOT and 3D-MOT. The colorful arrows shows the laser beam. **a)** The magnetic field produced by permanent magnets for 2D-MOT. $\boldsymbol{M}$ is the magnetic momentum of one block of permanent magnets. **b)** The magnetic field produced by two anti-Helmholtz coil pair for 2D-MOT. I is the current in coil. **c)** The magnetic field produced by one anti-Helmholtz coil pair for 3D-MOT. This plot is adapted by Joschka Schöner, a master student in our group, from Ref. [64]. P. 24.

2.3.5 Capture velocity of MOT

Armed with the above knowledge, we can get an intuitive picture of how the atoms are trapped. Fig. 2.11. (a) shows the simulated trajectories of atoms (white line) captured in a 2D-MOT and the phase-space dependence of force field acting on ^{164}Dy atoms. The specific parameters used in simulation is given in Tab. 4.1 in Ch. 4. The details of atoms trajectories calculations methods can be found in Ch. 4 section 4.1. Here we take the 2D-MOT as an example. And The situation of 3D-MOT is very similar. The atoms start from $x = -56.9$ mm, and have different initial velocities along $x-$axis (along the oven). The force field has two "clouds", one acceleration cloud at low-velocity values and another one deceleration at high-velocity values. From the figure, we can see that only the atoms below a certain velocity can be decelerated down to zero velocities at the MOT center, that is to say, be captured in a 2D-MOT. This critical velocity is defined as the capture velocity of a MOT.

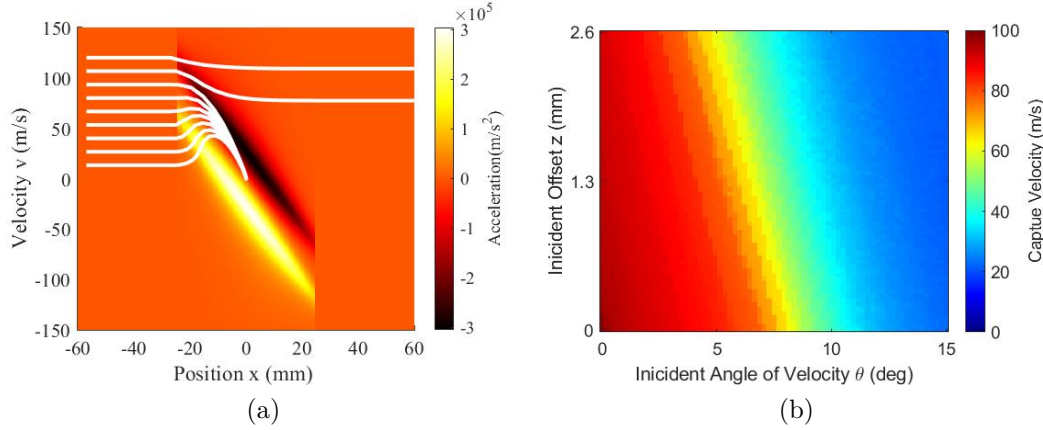(a)   (b)

Figure 2.11: **a)** The phase diagram of atoms with different initial velocity captured by a 2D-MOT. The white lines are the trajectories of atoms. The fake color background present the acceleration of atoms introduced by laser and magnetic field. **b)** The capture velocity of a 2D-MOT, with different incident angle and different position at $z-$axis, which is perpendicular to central-line of 2D-MOT.

Let us consider the ideal situation in which the laser beams have a uniform profile, and the power is so high that the absorption-spontaneous emission cycling always happens at the maximal rate $\Gamma/2$. In this case, the capture velocity is only determined by the size of the 2D-MOT,

$$v_{\text{Mcap}} = \sqrt{2\frac{\hbar k_{\text{L}}}{m}(2w)R} = \sqrt{2\frac{\hbar k_{\text{L}}}{m}\Gamma w}, \tag{2.49}$$

with k_{L} the wavevector of laser beam, m the mass of ^{164}Dy atom, w the radius of laser beam, and $R = \Gamma/2$ the rate of absorption-spontaneous emission. Equ. 2.49 actually gives the upper limitation of capture velocity v_{cap} that are experimentally

achievable,

$$v_{\mathrm{cap}} \leq v_{\mathrm{Mcap}} = \sqrt{2\frac{\hbar k_{\mathrm{L}}}{m}\Gamma w}. \qquad (2.50)$$

Until now we only discuss the capture velocity of atoms coming along the central line, $x-$axis, of the 2D-MOT. However, the capture velocity v_{cap} is also a function of incident position and incident angle of velocity. In Fig. 2.11. (b), we show the capture velocity with the same velocity magnitude, but different position offset along $z-$axis and incident angle θ of velocity. The capture velocity gets the maximal value along the central line of 2D-MOT (at $z = 0$, $\theta = 0$). And It decreases rapidly as z and θ increase. Meanwhile, the capture velocity is more sensitive to the incident angle θ of the velocity. In a conclusion, it is important to increase the atomic flow rate under a small incident angle θ from the oven. This part of the atomic flow rate is mainly contributed by atoms going through the aperture at a small angle without any collision. From the discussion in section 2.2.2 and 2.2.5, we know that part of the atomic flow rate is determined by the atomic flow rate leaving the effusion cell, which only depends on the temperature. Unfortunately, increasing the temperature does not help increase the atomic flow rate at a small angle, since it introduces more collision. In experiments, what we only can do is increase the angle from the oven towards the 2D-MOT, or let's say put the oven as close to the 2D-MOT as possible.

3 | Experimental Setup

In this chapter, the main parts of the experimental apparatus as well as the details of their installation will be presented. In section 3.1 and 3.2, we will present the basic mechanical design and main vacuum features of our experimental system operating on the ultracold atom cloud. An ultra-high vacuum environment is finally generated in our science chamber, where the optical access is also carefully optimized. In section 3.3, we show the details of our adapted atomic source aiming to achieve a fast-loading 2D-MOT. In section 3.5, we will show the arrangement of permanent magnets employed for 2D-MOT capturing and coil design employed for 3D-MOT trapping. In section 3.6, we will present our optomechanical and optical design for our 2D- and 3D-MOT. In section 3.7, we will discuss the optical setup of our laser source including frequency modulation and stabilization.

3.1 Overview

A schematic drawing of our experimental apparatus is given in Fig. 3.1. The atoms come from a high-temperature effusion oven inserted in a vertically mounted chamber (2D-MOT chamber) with six viewports providing optical access for 2D-MOT. The necessary magnetic field for the 2D-MOT is produced by eight blocks of permanent magnets placed on double sides of the 2D-MOT chamber. On the left side of the 2D-MOT chamber, there is a pumping stage attached with a CF63 viewport guaranteeing the optical access of a tilted push beam. On the right side of the 2D-MOT chamber, a differential pump stage (DPS) partially inserted in the 2D-MOT chamber divides the vacuum system into two parts: the high vacuum (HV) region containing the hot atomic source and ultra-high vacuum region (UHV) containing the science chamber (also called the main chamber). A manual gate valve and another pumping stage with CF16 viewports are connected between the DPS and science chamber. The octagon science chamber has eight CF40 flanges on the side, and two CF100 flanges for the re-entrant viewport on the top and bottom. The re-entrant viewports provide close access for objective lens to atoms with a 17 mm distance. The thickness of re-entrant viewports, the holder of magnetic coils, and the mount of the objective lens are all especially taken into account to maximize the optical access.

The atoms comes from the effusion oven along $x-$axis with a mean velocity $\sim$ 400 m/s. Then the 2D-MOT firstly captures the atoms in $x-z$ plane. A push beam

pushes the captured atoms in the 2D-MOT against $y-$axis to the science chamber through the DPS. Finally, the atoms are re-captured by a red 3D-MOT in the science chamber and are later trapped in an optical dipole trap forming the BEC.
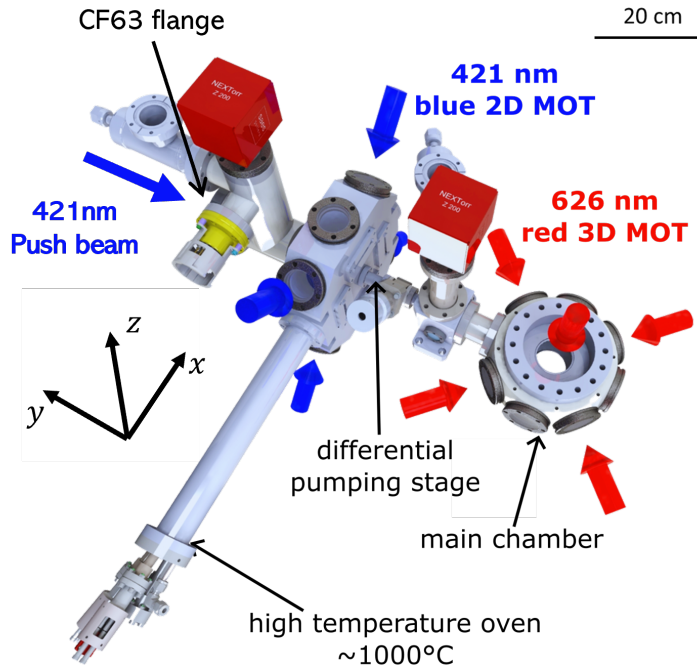

Figure 3.1: The configuration of our experimental apparatus. The atoms coming from a high-temperature effusion oven are firstly captured by a blue 2D-MOT in $x - z$ plane. Afterwards a push beam pushes the captured atoms against $y-$axis direction to the science chamber through the DPS. Finally, the atoms are re-captured by a red 3D-MOT in science chamber and further cooled to form BEC.

Our experimental design for the first time excludes the use of a Zeeman slower to produce ultracold gases of dysprosium atoms and replaces it with a 2D MOT. This new slow atomic beam source provides significant advantages:

1. The combination of 2D-MOT and push beams offers an optical switcher controlling the atomic flux to the science chamber. The presence of the 2D-MOT cooling light fully controls the flux of atoms in the science chamber, as evidenced by fluorescence measurement. Thus, no mechanical shutter in front oven for controlling atomic flux is necessary and very fast switching time can be achieved, allowing for high repetition-rate experiments.

2. There is not direct line from the high-temperature oven to the science chamber. Therefore, the noise contribution by the hot background atoms and the black body radiation [65] in science chamber is expected to be strongly reduced.

3. Removing the about one meter long Zeeman slower makes the whole setup compact. Finally it occupies about $70\,\text{cm} \times 70\,\text{cm}$ space on our optical table.

3.2   Mechanical and Vacuum System

The most of vacuum in our experiment is designed by Christian Gölzhäuser and well described in his Bachelor's thesis [66].

3.2.1   Vacuum levels

The required level of vacuum for atomic sources and experiments with ultracold atoms are different being on the order of $10^{-6} \sim 10^{-9}$ mbar and $10^{-10} \sim 10^{-12}$ mbar respectively. Therefore, a DPS is used to separate our vacuum into the HV region for atomic sources and the UHV region for the final experiments. Two same ion pumps (Nextorr Z200) are separately used in the HV region and UHV region to maintain the vacuum. The Nextorr Z200 provides a compact solution integrating the sputter ion pump and non-evaporable getter which can be mounted on a CF40 flange. A calculation of the required pumping speed can be found in the Bachelor's thesis of Christian Gölzhäuser [66]. Additionally, two of the same angled valve from VAT (54132-GE02-0001) are attached separately in HV and UHV regions aiming to provide the external connection for pre-pumps in order to establish a vacuum starting from atmospheric pressure. Under a normal operation of oven (effusion cell at $800\,^{\circ}$C and hot lip at $1100\,^{\circ}$C), we achieve a pressure $\sim 2 \times 10^{-9}$ mbar in HV region and a pressure $< 10^{-11}$ mbar in UHV region both measured by ion-pump driver.

3.2.2   2D-MOT chamber

The 2D-MOT chamber is designed by ourselves and produced by *SAES Vacuum Technology*. Fig. 3.2 is the mechanical drawing of the 2D-MOT chamber. It has an octagonal shape, with one CF40 flange port on the left side connecting to the HV pumping stage, one CF16 port on the right side connecting to the DPS, and eight CF40 flanges on the side providing optical access and connection to the oven. The bore diameter of the CF40 flange connecting to the oven is specially extended to 40.5 mm, so that the oven can be inserted into the 2D-MOT chamber. The end of the oven (including the endcap filter) is 44.5 mm away from the center of the 2D-MOT chamber, where the oven exactly does not block the optical access. The diameter of the CF40 flange facing the oven is also extended, and a blank flange is attached. On all other CF40 flanges, viewports with optical-grade fused-silica windows, AR coated at 626nm and 421nm, are attached. Both the chamber, attached viewports, and blank flange are made of titanium in order to minimize to influence on the magnetic field.

3.2.3   Differential pump stage

The pressure difference between the HV region and UHV region is maintained by a small tube, the differential pumping stage (DPS). The mechanical drawing of our DPS is given in Fig. 3.3. The DPS is inserted into the 2D-MOT chamber by 16 mm
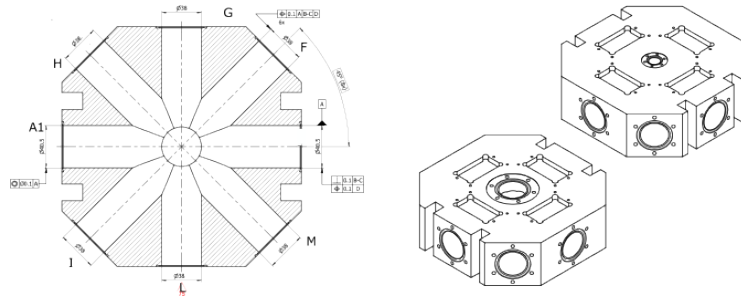
Figure 3.2: The mechanical drawing of our differential pumping stage (DPS).

aiming to minimize the small DPS aperture as well as the distance between the 2D-MOT and 3DMOT. It connects with the 2D-MOT chamber by a CF16 flange on the left side. And it is machined to be like a cone with 1.96° vertex angle in order to accommodate the divergence of the atomic beam. The length of DPS is 57 mm The diameter of DPS is 2 mm at entrance, and 5.9 mm at the end.
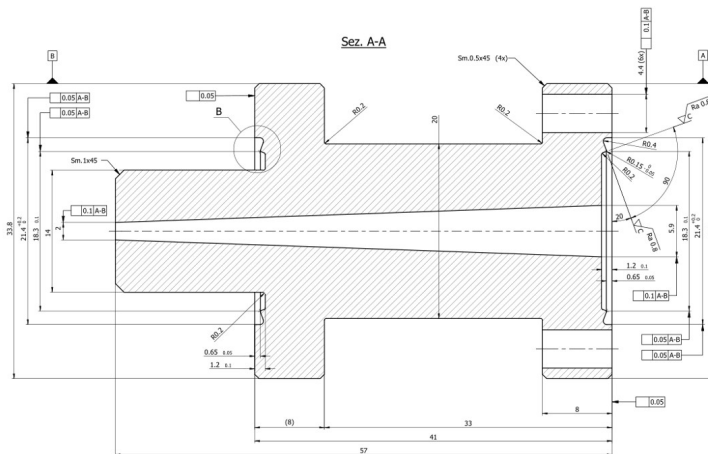

Figure 3.3: The mechanical drawing of our differential pumping stage (DPS).

3.2.4 Science chamber

Our science chamber made by *SAES Vacuum Technology* follows a standard design and has eight CF40 flanges on the side and two CF100 flanges at the top and bottom. Here, everything is made of nonmagnetic 316LN stainless steel. On seven of the CF40 flanges, viewports with optical-grade fused-silica windows, AR coated at 421 nm, 626 nm, 532 nm, and 1064 nm, are attached. The remaining CF40 flanges are attached to the rest of the experimental setup. In the two CF100 viewports, it is planned to attach 2 re-entrant viewports, specially designed by ourselves and fabricated by *Kurt J. Lesker*. As shown in Fig. 3.4, the thickness of the re-entrant viewport is decreased and the holder of the coil is also specially designed to ensure a 41° optical access. However, due to an important production delay of the re-

entrant viewports, currently, two standard fused-silica uncoated CF100 viewports
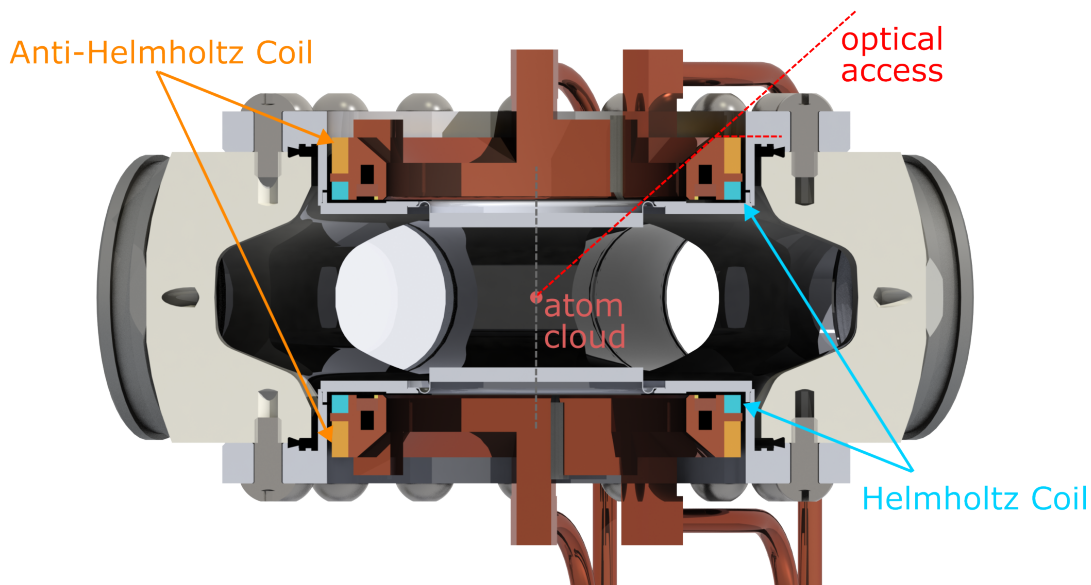are mounted.

Figure 3.4: The design of coil for the magnetic field at our science chamber.

3.2.5 Vacuum Construction

In this section, we will briefly summarize the installation of our vacuum system.
All the cleaning procedure is done by the factory. All the screws and plate nuts we
used are made of nonmagnetic 316LN stainless steel. Before tightening the screws,
a little grease was smeared on the screws making sure they can be removed. The
screws are tightened following a special order [67]. The torque range is used during
the tightening of most flanges. However, there are a few flanges that are impossible
to be accessed with torque range and are tightened by hand.

The first vacuum was established using an external oil-free mechanical pump
(MVP 015-4) and a turbo pump (HiPace 80 Neo) from *Pfeiffer Vacuum GmbH*.
Additionally, an residual gas analyzer (STRGA-100-EU from *SI Scientific Instru-
ments*) is connected to monitor the pressure of the different elements (mainly N_2,
O_2, H_2, H_2O, etc.) during the pumping. After pumping, a leak test is done with
helium gas and the residual gas analyzer.

Aiming to achieve the desired high vacuum environment, we bake the vacuum
system in two steps: firstly it is assembled with blank flanges instead of viewports
and baked at a high temperature ($\sim 300°$C); secondly we install the viewports
and bake the system at $\sim 150°$C below the tolerance of viewports ($\sim 180°$C).
The baking is done by heating wires twined on the apparatus but isolated from the
apparatus with a layer of aluminum foil. Plenty of thermal couplers are directly
attached to the apparatus for monitoring the temperature. Besides another layer of
aluminum foil covers the heating wires. The purpose of those two layers of aluminum

foil is to make the baking uniform and decrease the dissipation of heat. It took us more than three days to slowly reach the target temperature (as well as cool down), and we kept the high temperature on for more than one week.

After the first high-temperature baking, a leaking suddenly appeared when we removed the aluminum foil and thermal coupler near a blank flange on the top of the 2D-MOT chamber. It might be caused by the different thermal expansion coefficients between the titanium 2D-MOT chamber and the stainless steel blank flange. Unfortunately, due to a huge delay in our re-entrant viewport, we had to build our system with two normal CF100 viewports (), and the re-entrant viewport will be baked in another setup[1].

3.3   High-Temperature Effusion Oven

As the oven, we use a commercial solution provided by *CreaTec Fischer & Co. GmbH*. We use the standard dual filament cell DFC-40-25-WK-2B and adapted the design of the aperture set included in the crucible to match the new possibilities offered by the replacement of a Zeeman-slower source by a 2D-MOT source, see discussion in sections 4.2. The optimization and design of these apertures were made by us and are described in section 4.2.1. In the Fig. 3.5 and Fig. 3.6, we give the mechanical drawing of our effusion oven and the structure of the aperture. The oven has a heating system, which can heat the crucible up to 1400 °C while the outer wall of the oven is water-cooled to prevent heat radiation out of the crucible in the lab. The heating region is divided into two zones: the effusion cell storing the Dy sample, and the hot lip where the apertures are. The hot lip zone should be heated to a higher temperature than the effusion cell to avoid Dy accumulating inside the aperture. The effusion cell has a 25 cc volume which should be able to include 60 g dysprosium. The aperture set is composed of two apertures: a tubed aperture is used to collimate the atomic beam and control the lifetime of dysprosium to be three years; another thin-wall aperture at the end of the oven connect to cooling water is used to cut the atomic beam into 15°.

3.4   Problem of viewport coating

Unfortunately, after we run our experiment with 2D- and 3D-MOT for about three months, we found the two viewports on the 2D-MOT chamber facing the oven are coated by dysprosium. Fig. 3.7 shows a coated viewport on our setup. The upper gray semicircle is the accumulated dysprosium. By measuring the transmission of a small beam, we found that the whole viewport is coated with Dy.

Fig. 3.8. (a) is a picture taken from one of the coated viewport. The red part is the found side of the crucible which appears to be hot. The yellow-orange part that we see through a gap in the endcap is our effusion oven operating at 1100 °C. Fig. 3.8. (b) shows a temperature-measuring picture from an infrared thermal imaging camera.

---

[1]Until I write this sentence, the baking is still not finished
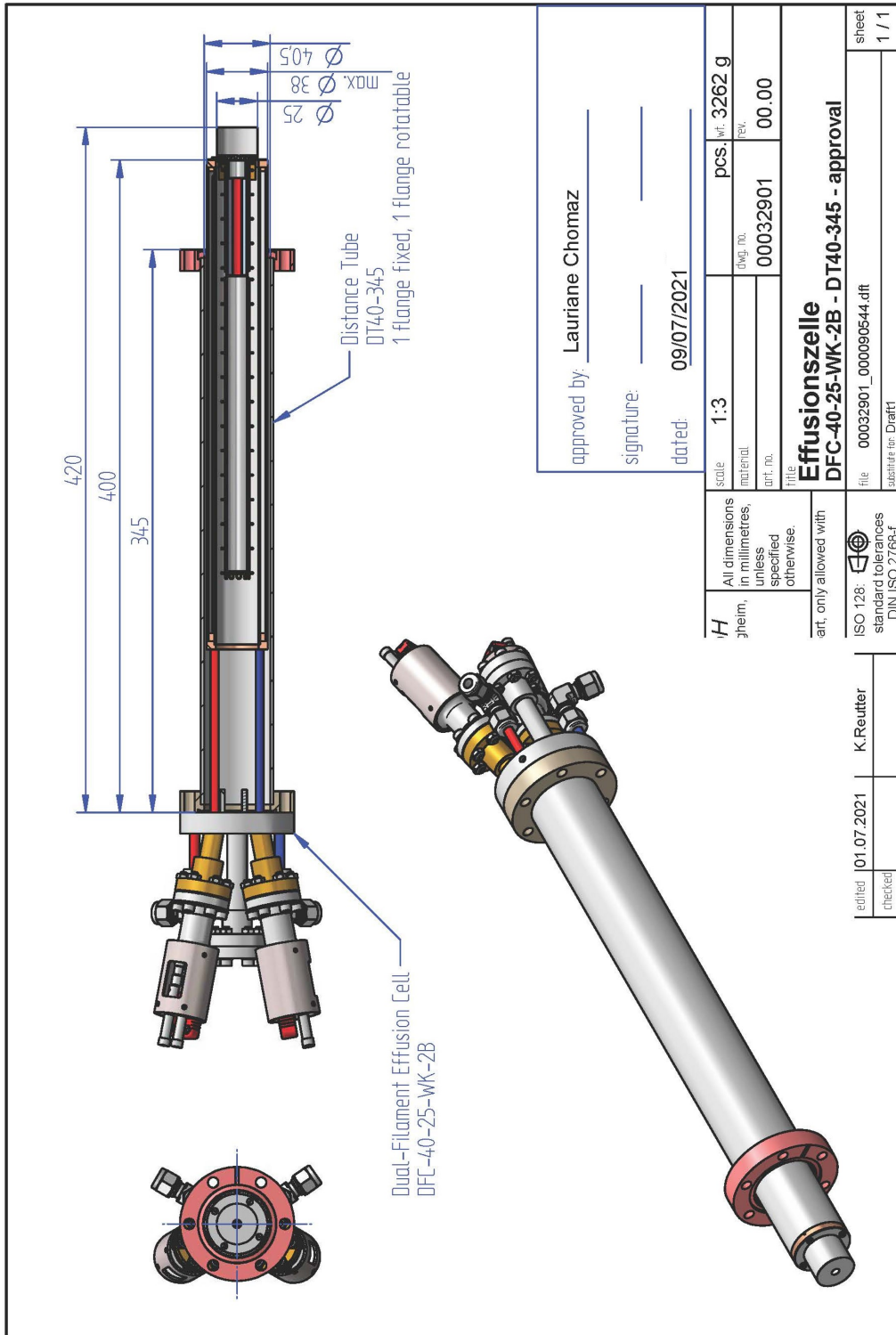
Figure 3.5: The mechanical drawing of our effusion oven.
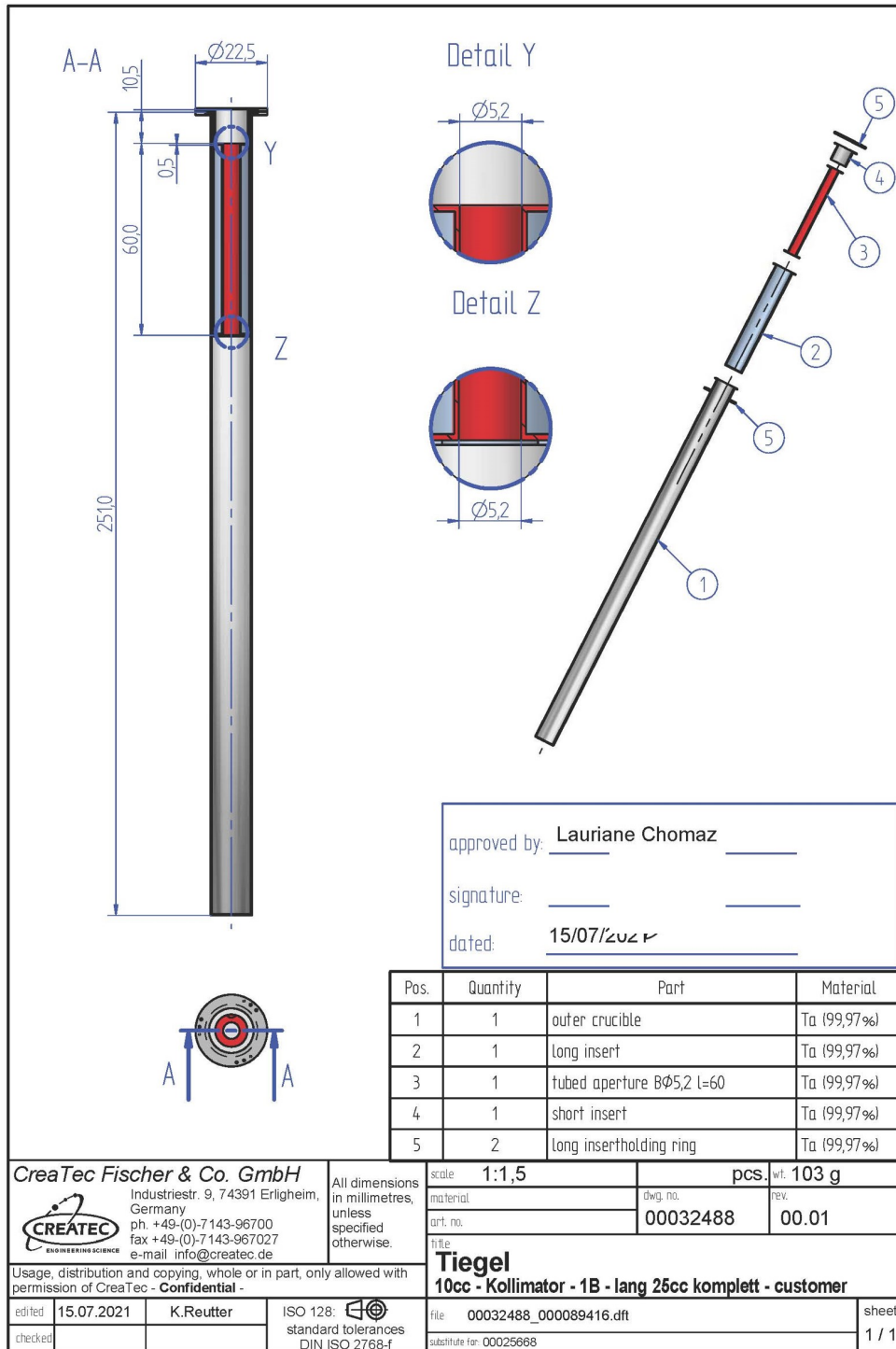
Figure 3.6: The mechanical drawing of the aperture sets in our oven.
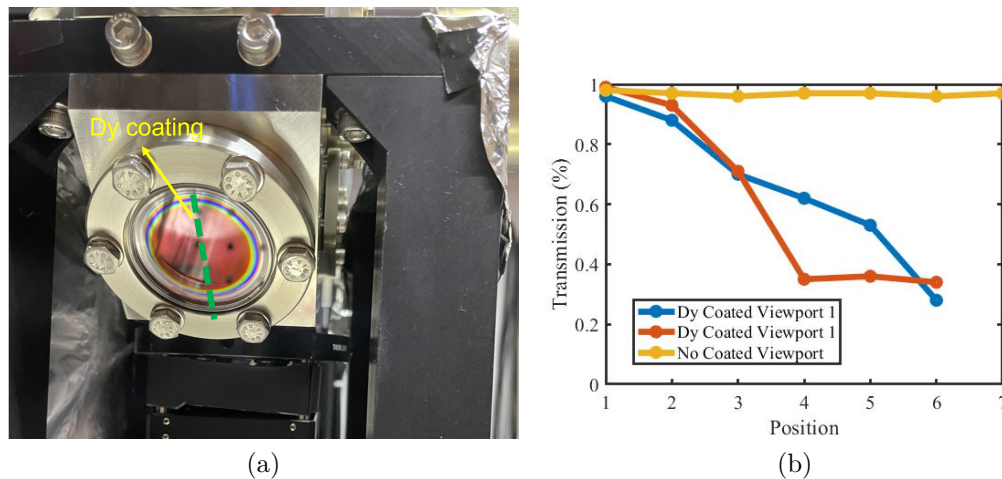
Figure 3.7: **a)** A picture of the coated viewport. **b)** The transmission of coated viewport at different position along the green dash line in the left picture.

The camera can only measure a temperature up to 300 °C, but by comparing with the colormap of black body radiation temperature of the red part is believed above 800 °C.
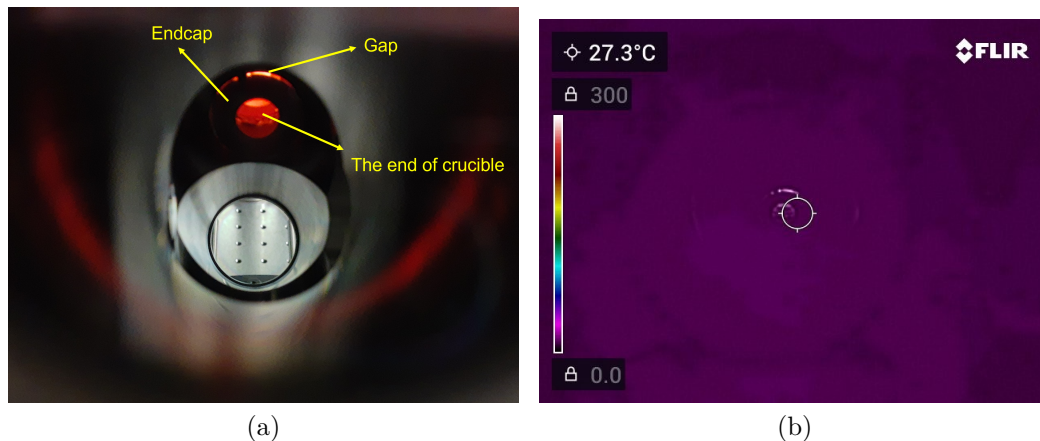
Figure 3.8: **a)** A picture of our oven endcap through a coated viewport. **b)** The temperature of the endcap measured by an infrared thermal imaging camera.

Therefore, we consider the dysprosium coating maybe is caused by the following two reason:

1. There is a gap on the endcap as shown in Fig. 3.7. (b), which makes a direct view of the oven.

2. Although the endcap attached to cooling water can cut the atomic beam into 15° as shown in Fig. 3.9, the direct line from the heated structure in the oven (the red structure in Fig. 3.8. (a)) to the viewport is not completely blocked.

Those hot structures can also absorb and emit Dy atoms like a second atomic source confirmed by the IR camera imaging in Fig. 3.8. (b)).

Figure 3.9: Design of the aperture sets in the oven with 15° collimation angle.

In all the above discussion the atomic beam is assumed to fly along a straight line, but there are also two factors that can broaden the atomic beam: the collisions between atoms, and the magnetic field. At $1100\,^\circ$C the density of Dysprosium atoms in the effusion is 7.1×10^{19} atoms/m^3 calculated by Equ. 2.1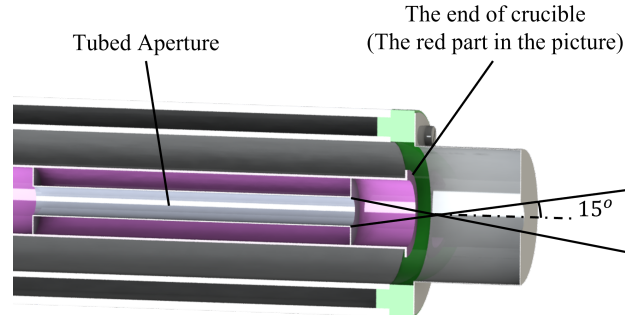. The radius of the tubed aperture is only $2.6\,$mm much smaller than the viewport-oven distance, which is tens centimeters. The atomic beam can be considered as emitting from a point and the mean-free-path of atoms at different distances away from the oven can be calculated. Besides, in order the estimate the influence of the magnetic field, we calculate the trajectories of atoms emitted at 15° angle from the oven under a $42\,$G/cm magnetic field gradient without any laser beams. The details of trajectory calculation is introduced in Ch. 4. The results of those two estimates are shown in Fig. 3.10. From the Fig. 3.10. (a)), when the atoms are $10\,$cm away from the oven, mean-free-path of atoms has already at meter scale. Thus, it is safe to neglect the atom collision. In the Fig. 3.10. (b)), we rotate the coordinate by 15° making the $x-$axis is the direction of atoms flying. The back lines represent our 2D-MOT chamber and the red lines represent the viewports. We can see that a $42\,$G/cm magnetic gradient won't make the atoms reach the viewports.

To correct for this observed design failure, we decided to:

1. Make a new endcap with a smaller radius ($4.5\,$mm)

2. Extend the length of the new endcap and the distance by $24\,$mm between the oven and 2D-MOT chamber by adding a double-side flange,

3. Remove the gap on the endcap.

4. Add some shields to prevent the front of the crucible to be hot.

After we install the new endcap and built the vacuum, the temperature of the endcap is measured by the infrared camera again as shown in Fig. 3.11. We can see now that through the viewport it can only see the cold parts of the oven, and all
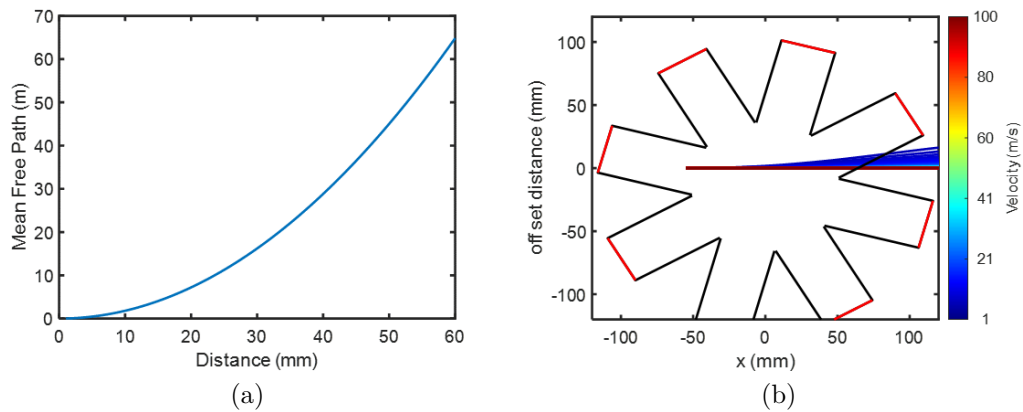
Figure 3.10: **a)** The mean-free-path of atoms at different distance after emitted from the oven. **b)** The trajectories of atom emitted at 15° angle from the oven under a 42 G/cm magnetic field gradient without any laser beams.

the hot parts are blocked by the new endcap. The yellow-orange light in figure (a) is the thermal radiation from the crucible reflected by the inner wall of the metal endcap. As I write this sentence, it has passed about two months since we recover the vacuum and 2D-MOT. The coating problem has not appeared again.

Figure 3.11: **a)** The picture of our new endcap through the same viewport. **b)** The temperature of the new endcap measured by the same infrared thermal imaging camera.

3.5   Magnetic Field

3.5.1   2D-MOT magnetic field

The magnetic field for 2D-MOT is produced by eight blocks of permanent magnets on the double sides of the 2D-MOT chamber. We choose the neodymium magnets

(ECLIPSE N750-RB), which have a magnetization $M = 8.75(10) \times 10^5$ A/m [36, 35]. The configuration of magnets is introduced in Fig. 2.10. Fig. 3.12 shows an example of magnetic field with seven magnets per block, and the block is 63.0 mm away from the chamber center in $x-$ or $z-$axis and 32.5 mm away from the chamber center in $y-$axis. At the center it achieves a 36.72 ± 0.67 G/cm gradient along $x-$axis. More details can be found in the Bachelor's thesis of Christian Gölzhäuser [66].
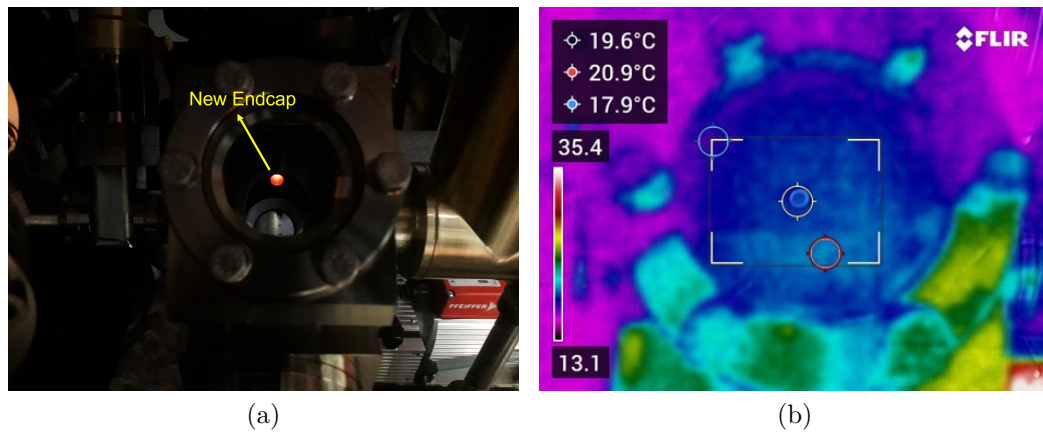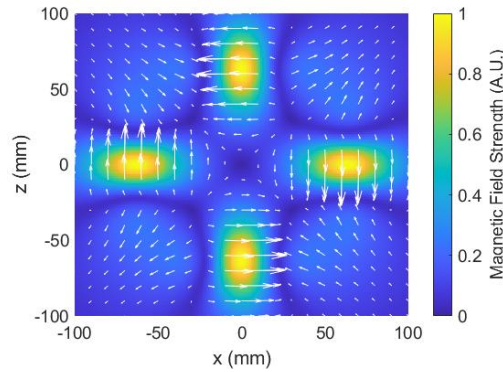

Figure 3.12: The magnetic field for the 2D-MOT.

3.5.2   Magnetic field in main chamber and 3D-MOT gradient fields.

The magnetic fields in the main chamber are produced by a set of 4 coils pairs designed by Joschka Schöner [68] and Lenny Hoenen [69]. Detailed descriptions can be found in their respective theses [69]. Three pairs of coils are designed to produce a homogeneous field in an arbitrary spatial direction. One pair of coils is designed to produce a magnetic field gradient, in particular, that is needed for the 3D-MOT.

The magnetic field gradient for 3D-MOT will be produced by an anti-Helmholtz coil pair, which is installed inside the re-entrant viewport as shown in Fig. 3.4. With a water cooling system, the coil pair can produce a magnetic gradient up to 21 G/cm, and the homogeneity of the coil pair is also optimized. In the region 17 mm from the center along $x-$ and $y-$axis, the deviation of magnetic gradient is smaller than 4.15% . A full introduction to gradient coil design and manufacturing can be found in Joschka Schöner's Master thesis [68].

3.6   2D-MOT Optics

Our 2D-MOT configuration and coordinate are shown in Fig. 3.13. To maximize the power per beam, we use a bow-tie design, and there is only one incident beam in 2D-MOT. The incident beam comes from a 3 meters optical fiber (PMC-E-400Si-3.5-NA011-3-APC.EC-300-P) and is collimated through a collimator (60FC-T-4-M25-01) with 25 mm focal length. Both optical fiber and fiber collimator are ordered from *Schäfter + Kirchhoff GmbH*. A three-lens Galileo telescope is used to magnify the beam after the fiber collimator. The first lens is a bio-concave lens with -25 mm
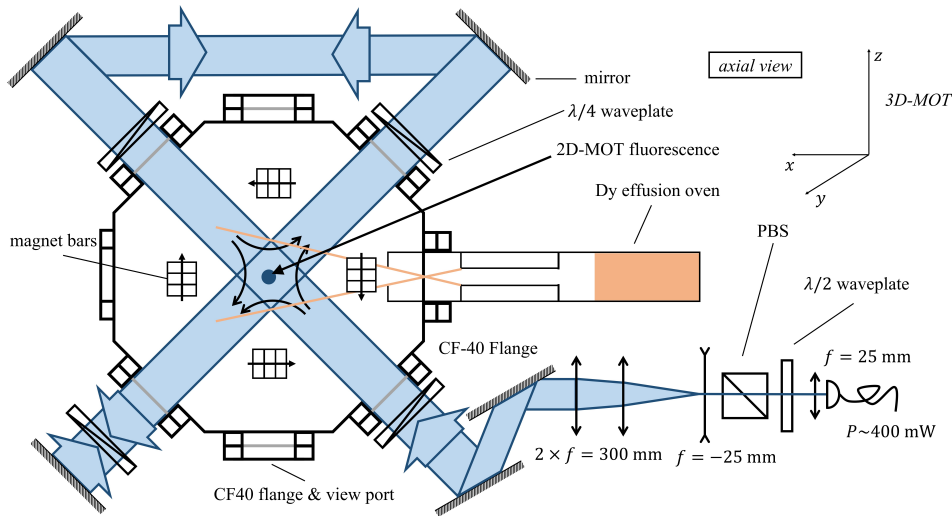
Figure 3.13: The configuration of our 2D-MOT as well as the coordinate used in simu-
lation. The origin of coordinate locates at the center of 2D-MOT chamber.
The atomic beam out of the oven comes alone the $x-$axis. The 2D-MOT
cooling beams propagates in the $x-z$ plane and a push beam (not shown in
this figure) is sent along y-axis for pushing atoms from 2D-MOT to 3D-MOT,
and $z-$axis is against gravity.

focal length, and the second and third lenses are both plano-convex lenses with
300 mm lens. The wavefront error of the combination of the collimator and telescope
is checked with *Zemax*. We carefully design a wavefront error smaller 0.25 waves
(root-mean-square value) guaranteeing the beam quality [70]. Fig 3.14 gives the
wavefront error when the distance between the first and second lens is 10 mm and
the beam waist after telescope is 18 mm. In such a three lenses telescope, the output
beam waist can be increased by shortening the distance between the first and second
lenses, and the focus of the beam can be changed by moving the third lens. The
length of the total optical path is designed as 350 mm. We use a cage system to
mount them to facilitate the alignment and two mirrors are used to fold the path
and align the input arm. Limited by the optomechanics in the experiment, the
designed 18 mm maximal beam waist is not achieved. The measured maximal beam
waist is 15.50(0.29) mm at the distance, where the beam first passes through the
2D-MOT. Besides, before the 45° reflection happens at the top of 2D-MOT, two
quart-waveplates change the circular polarization back to linear polarization due to
the different reflectivity of $s-$polarization and $p-$polarization.

Another push beam is used for pushing atoms from 2D-MOT towards 3D-MOT,
which is perpendicular to the 2D-MOT plane and against the $y-$axis. The push
beam comes from a 5-meter fiber (PMC-E-400Si-3.5-NA011-3-APC.EC-300-P) and a
collimator (60FC-4-M15-26) with 15 mm focal length leading to a 1 mm beam waist,
which is designed as the same as the radius of DPS. Both the fiber and collimator
are ordered from *Schäfter + Kirchhoff GmbH*. Then two 2 inch mirrors mounted on
mirror mounts with $100\,\mu$m/turn micrometer screws (MXI-HS-C-2-3030-M6 from

Radiant Dyes Laser Accessories GmbH) providing the necessary precision for alignment. After those two mirrors, a quarter-waveplate is used to make the push beam circular polarized.
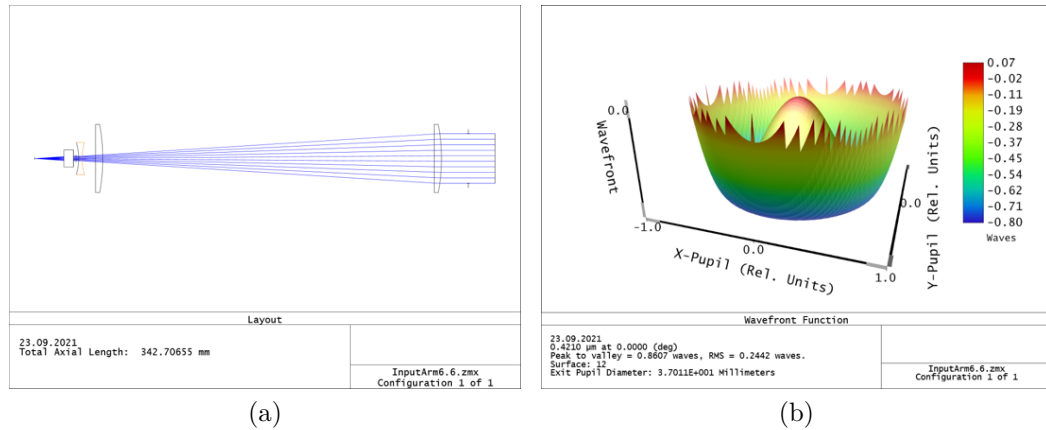
Figure 3.14: **a)** The configuration of the optics in 2D-MOT incident beam with an 18 mm output beam waist. **b)** The wavefront error of that configuration calculated in *Zemax.*

3.7   Optical Path on Laser Table

The power distribution, frequency modulation and frequency locking of our 421 nm and 626 nm laser beams are done on another optical table called laser table.

3.7.1   Power distributions

The optical path for power distribution and frequency shifts is given in Fig. 3.15. Both of our blue and red lasers are commercial frequency-doubled diode lasers (DLC TA-SHG PRO) from *TOPTICA Photonics AG*. The ability of frequency tuning of laser diode around 842 nm for blue (1252 nm for red) is realized via an grating-stabilized external cavity. The light from a laser diode is then amplified by a tapered amplifier and frequency-doubled via second harmonic generation through a crystal placed within a cavity. At the output of laser, we get $\sim 1\,\text{W}$ power for blue laser and $\sim 2\,\text{W}$ power for red laser. All the acoustic optical modulators (AOMs) we used are ordered from *EQ Photonics GmbH*. The blue laser is locked at the frequency of 2D-MOT, which is about 50 MHz red detuned from the resonance, and the red laser is locked 200 MHz blue detuned from the resonance. More information about the detuning of each beam can be found in Ch.4. It is also worth mentioning that the push beam breach is firstly separated starting from the laser output since it is most sensitive to power fluctuation.
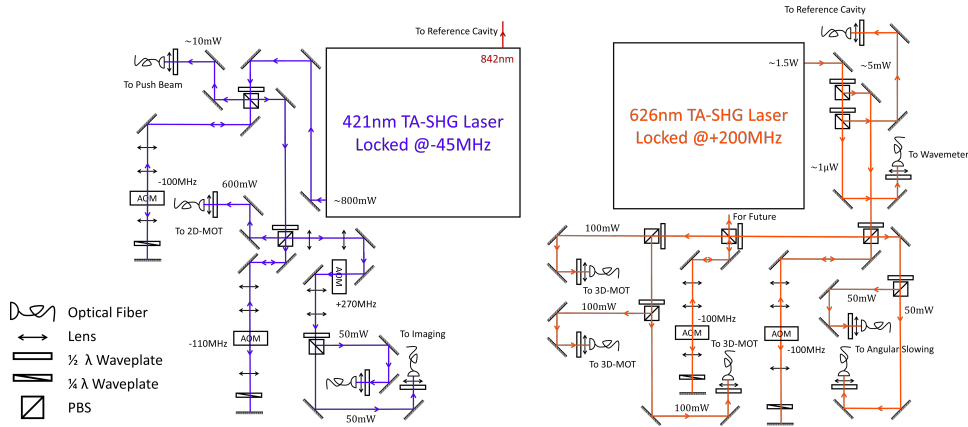
Figure 3.15: The schematic of our optical path on laser table.

3.7.2 Frequency locking

Fig. 3.16 shows a typical method, Pound-Drever-Hall (PDH) technique [71], for laser frequency locking. In our case, we replace the Pockels cell with fiber-based electro-optic modulators (EOM) (PM635 and PM830) from *JENOPTIK Optical Systems GmbH.* Meanwhile, a dichroic mirror is placed in front of the cavity, so that both blue and red lasers can be locked with the same cavity. Since it is hard to make a broad anti-reflection coating on the cavity, we use the fundamental wavelength 842 nm before the frequency doubling of the blue laser and the output wavelength 626 nm of red laser for frequency locking. The reference cavity (6010-4) is ordered from *StableLaserSystems, Inc.* It has a 1.5 GHz free spectrum space and a measured finesse 21170(60) at 842 nm and 20760(40) at 626 nm. The laser itself provides built-in software for PDH locking, but the built-in proportional–integral–derivative (PID) loop is not fast enough. For the narrow red transition, we order the *FALC pro* module from *Topica*, which provide a modulation bandwidth up to 50 MHz. For the relative broad blue transition, we use the same solution as Selim Jochim's group in Heidelberg university based on *RedPitaya STEMlab 125-14* board.

Different from the basic PDH locking, the laser is not directly locked at the mode of the cavity, but a side-band $60 \sim 500$ MHz away from the mode of the cavity created by EOM. And two other 1.5 MHz side-bands are also created by EOM for producing an error signal in PDH locking, as shown in Fig. 3.17. Thus, the locking point can be easily moved by changing the modulation frequency creating the first side-band. The blue laser is directly locked at the frequency of 2D-MOT. Therefore, without any AOM or EOM in the optical path, the power sent to 2D-MOT is maximized.

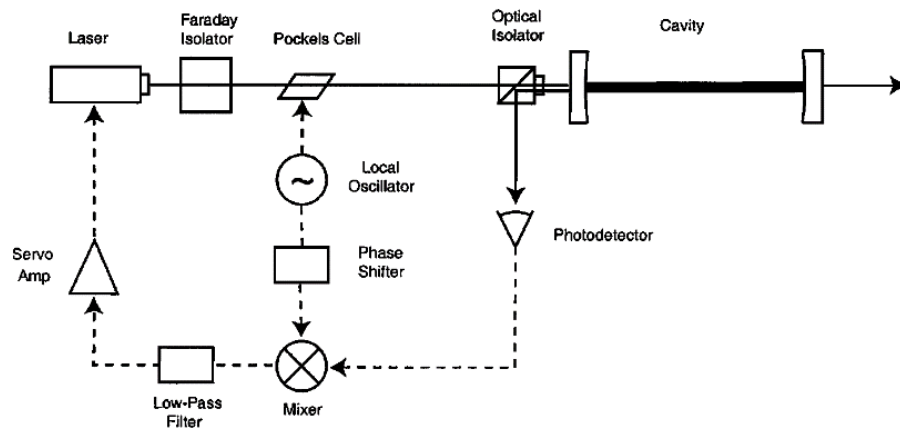Figure 3.16: The Pound-Drever-Hall (PDH) technique for laser frequency locking. This figure is taken from Ref. [71].
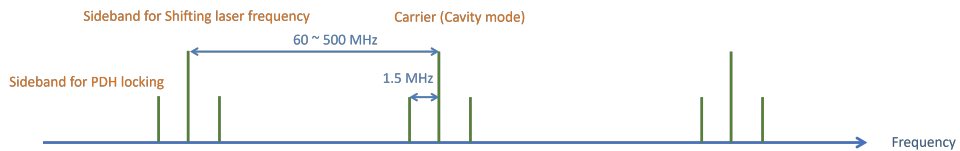

Figure 3.17: The locking point in our PDH locking system

4 | Simulations of the Slow Atomic Source and First Experimental Results

In Ch.2, the theory of atomic beam and the principle of MOT capturing is detailed introduced. In practice, however, the situation becomes more complex. We have to choose suitable parameters for laser power, detuning, beam size, and magnetic gradient for our 2D- and 3D- MOT, as well as the spontaneous emission scattering and collision with hot background atoms play a crucial role in the loading efficiency. Therefore, Simulations are done based on Monte-Carlo methods aiming to find the best parameters for our oven and MOT, which then can give us clues to design our experiment setup.

4.1 Monte-Carlo Simulation Principle

It is tricky to simulate the trajectories of more than 10^{15} atoms, as a naive simulation from the first principle would require extremely large computing resources. Thus, the so-called Monte-Carlo (MC) method is applied in our simulation. This method consists in estimating the results of a complex calculation based on computer-generated random samples from a given probability [72]. In total, three different types of simulations are done.

The first one simulates the angular distribution with different aperture structure in the oven. We sample the initial conditions (i.e. initial positions and velocities) of several hundred thousands of atoms, and the calculate their trajectories from the exit of effusion cell to the exit of the last aperture. The atom-atom collision is ignored. Each time, when an atom-wall collision happens, the velocity direction of atom will be sampled according to Lambert's cosine law. When all of atoms get out of aperture or get back to the effusion cell, the simulation stops. In practice, in order to avoid an infinite loop, the simulation is also forced to stop at 10,000 times of collision. But by checking manually, forced stopping never happens.

Another simulation is done for estimating the loading rate of our 2D-MOT. The sampled atom number decrease to several thousands due to the increased complexity. The initial conditions of atoms are sampled at the exit of the last aperture in our oven. Here, we take the probability function given by Equ. (2.3) in Ch.2 instead of

the result of the first simulation. As there, we don't take in account of the atom-atom collision, which is considered as an important factor on angular distribution of atomic beam in transitional flow regime. The atoms trajectories are then calculated in a force field induced by laser light and magnetic gradient. The loading rate is estimated according to the ratio between the number of atoms loaded into the 2D-MOT, and the total number of sampled atoms.

A third simulation is done for estimating the loading rate of our 3D-MOT, which is similar to the 2D-MOT simulation. It also starts from the exit of the last aperture in our oven, but don't stop at 2D-MOT. It continues, until the atoms are pushed and captured in 3D-MOT. For the reader who is interested in our program implement, we would like to mention that the scripts are divided into three steps: 2D-MOT, pushing, and 3D-MOT aiming to save computation resources.

In short, work-flow of each single atom in our 2D- and 3D-MOT simulation is the following.

1. Initialization

   In the beginning, the initial positions and velocities of atoms at the output of the effusion oven aperture are produced according to the acceptance-rejection sampling function introduced in section 4.1.1, where the probability functions are provided by the theory in Ch.2.

2. Trajectory calculation

   Then the dynamics of the atom position and velocity are solved based on the second Newton's Law by a four-step Runge-Kutta method. More details, as well as the time step used in our simulations, are introduced in section 4.1.1. The force field is calculated according to Equ. (2.38). The contribution from spontaneous emission is also included by a random process according to Equ. (2.41).

3. Exit condition

   The whole simulation is divided into three steps, 1)loading into the 2D-MOT, 2)pushing from 2D-MOT towards the 3D-MOT, and 3)loading into the 3D-MOT. In order to decrease the time atom stay in 2D-MOT, where they are bombarded by the hot atoms from the oven, the push beam is shining on in the first step. In the first step, we additionally include the effects of the atom-atom collision and randomly abandon a certain fraction of the atom trajectories depending on the expected collision rate, which is provided by the mean-free-path of atoms.

   In the 2D-MOT simulation, it stops after the first step. In the 3D-MOT simulation, after the first step, we select the atom which stays in a 20 mrad^2 solid angle[1], from the 2D-MOT towards the 3D-MOT. The total time of each

---

[1] 20 mrad^2 is checked by a few pre-simulation, making sure we select all the atoms possibly captured in 3D-MOT

simulation part is different, but large enough to make sure that the atom trajectory either goes far away from the 2D- or 3D-MOT region or approaches the center of 2D- or 3D-MOT, which is considered to be loaded.

In the following, detail important aspects of the MC simulation procedure is introduced, including 1) how the initial position and velocity are sampled. 2)how the dynamics of atom trajectory are solved. 3)how the loading rate of the 2D- and 3D-MOT is estimated.

4.1.1   Sampling the initial position and velocity

Since the core of the Monte-Carlo approach is estimating a statistical quantity by lots of random events, it is crucial point how to sample the random variables. As mentioned above, such a sampling procedure is involved in initializing atom positions and velocities, determining the direction of spontaneous emission, as well as abandoning the trajectory caused by atom collisions.

General principle of random sampling

Let us first consider a more general situation, we have a distribution function $y = f(x)$ of a normalized random variable $x \in [0, 1]$. If $f(x)$ have an analytic inverse function f^{-1}, we first sample the value of $y \in [0, f_{\max}]$ by a uniform random distribution, then the random variable x is obtained by following formula,

$$x = f^{-1}(y), \tag{4.1}$$

The sampling procedure continues until the demanded number of random samples is reached.

However, more usually, the analytic form of f^{-1} doesn't exist or is very hard to write down. Then we can use the acceptance-rejection sampling function, also called the Von Neumann method [73]. As shown in Fig. 4.1, if we draw the distribution function $f(x)$ in a coordinate system, in such a plane, each point (x, y) presents a situation of system and all of them have the equal probabilities, but only in the shadow area below the curve of $f(x)$ is allowed. We can easily sample a point (x_1, y_1) by two uniform random sampling procedures, once for x, once for y. If (x_1, y_1) locates beyond the shadow area, equaling to $y_1 > f(x_1)$, then we reject this combination (x_1, y_1). Otherwise, for example another point (x_2, y_2) locates in the shadow area, where $y_2 \leq f(x_2)$, we accept the combination (x_2, y_2). The procedure is also repeated until we reach the demanded number of random sampling.

Sampling initial position distribution

Although the far-field angular distribution of an atomic beam is well studied [54], due to the complexity of atom random motion what happens in the near-field is still not well understood. We keep the assumption in Ch.2 section 2.2.7: the atom position distribution from an aperture is uniform and independent of the velocity
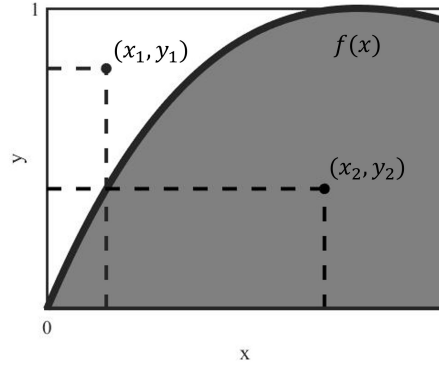
Figure 4.1: An example of acceptance-rejection random sampling. The solid black line shows the probability function $f(x)$. if a point is under $f(x)$ (in the gray area), it will be accepted, otherwise (in the white area) it will be rejected. So the point (x_2, y_2) is accepted and the point (x_1, y_1) is rejected.

(a)   (b)
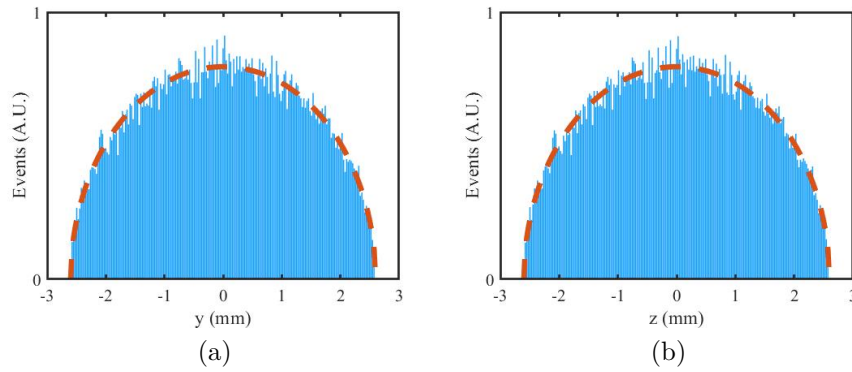
Figure 4.2: An example of sampled atom initial position (blue bars) comparing with exception value (red dash line). The oven temperature is $1000\,^\circ\mathrm{C}$, the tubed aperture radius $r_{\mathrm{tube}} = 2.6\,\mathrm{mm}$ and the length $L_{\mathrm{tube}} = 60\,\mathrm{mm}$. Histograms are calculated for $50,000$ atoms

distribution. Since our oven output aperture locates at $x = x_0$, we only need to produce two random numbers for y and z. In the following, we will only consider circular oven apertures, which are central-symmetric. It is more convenient to do it in the cylindrical coordinate system (r, α), with

$$y = r\cos\alpha, \qquad z = r\sin\alpha, \tag{4.2}$$

where $r \in [0, r_{\mathrm{aperture}}]$, $\alpha \in [0, 2\pi)$, generated from two independent uniform random sampling. The Fig. 4.2 shows the sampled position at $x = -59.6\,\mathrm{mm}$ with a $r = 2.6\,\mathrm{mm}$ aperture. The histograms show the number of sampled atoms with different y and z positions, which is proportional to the width of the aperture at the respective position. So the exception value is given by an ellipse curve, whose long-short axis ratio is $2:1$ and short axis equals r_{aperture}.

Sampling initial velocity distribution

On the other hand, the sampling for initial velocity takes more effort. Still, we hold the assumption introduced in Ch.2: the velocity magnitude and its angular distribution are uncorrelated. Thus, we sample the velocity field using the spherical coordinates (v, θ, ϕ) which define the velocity component via,

$$
\begin{aligned}
v_x &= v \cos \theta, \\
v_y &= v \sin \theta \cos \phi, \\
v_z &= v \sin \theta \sin \phi.
\end{aligned}
\tag{4.3}
$$

Firstly the velocity magnitude v is sampled according to the Maxwell-Boltzmann distribution with the acceptance-rejection sampling function (see the beginning of this section). In the simulation, we cut off the maximal velocity magnitude at $200 \, \mathrm{m/s}$ along the central line of the 2D-MOT, while the capture velocity is smaller than $120 \, \mathrm{m/s}$. We numerically checked that if the starting velocity is larger than the capture velocity, the atoms can not be captured by the MOT. Increasing the sampled velocity magnitude does not improve the precision, but only wastes more time.

Regarding to the angular distribution, θ is sampled according to Equ. (2.18), and ϕ is sampled from uniform distribution in $[0, 2\pi)$. The Fig. 4.3 shows an example of sampled velocities of $50\,000$ atoms. The temperature effusion cell is $1000 \,^\circ\mathrm{C}$ and the tubed aperture radius $r_{\text{tube}} = 2.6 \, \mathrm{mm}$ and the length $L_{\text{tube}} = 60 \, \mathrm{mm}$. In order to show the Maxwell-Boltzmann distribution, the upper limitation of sampled velocity is extended to $650 \, \mathrm{m/s}$. In our simulation, the maximal capture velocity of 2D-MOT we found is about $83.7 \, \mathrm{m/s}$. It corresponds 1.15% of the atoms from the oven according to the Maxwell-Boltzmann distribution.

4.1.2 Atom Dynamic Solution

Applying the theory of light-atom interaction introduced in Ch.2, the force acting on atoms can be computed according to Equ. (2.38). Then the trajectory of the atoms is calculated from Newton's second law with the four-step Runge-Kutta methods [74] aiming to provide a higher precision for numerical solution. Specifically, considering at time t_0, an atom locates at $\boldsymbol{r}_0 = \boldsymbol{r}(t_0)$ with a velocity $\boldsymbol{v}_0 = \boldsymbol{v}(t_0)$, the acceleration $\boldsymbol{a}_0 = \boldsymbol{a}(t_0) = F(\boldsymbol{r_0}, \boldsymbol{v_0})$ can be calculated by Equ. (2.38) in Ch.2. Now, we want to know the position and velocity of this atom after a small time step Δt, which is calculated by

$$
\begin{aligned}
\boldsymbol{r}_0 &= \boldsymbol{r}(t_0), & \boldsymbol{v}_0 &= \boldsymbol{v}(t_0), & \boldsymbol{a_0} &= F(\boldsymbol{r}_0, \boldsymbol{v}_0) \\
\boldsymbol{r}_1 &= \boldsymbol{v}_0 + 0.5\Delta t \boldsymbol{v}_0, & \boldsymbol{v}_1 &= \boldsymbol{v}_0 + 0.5\Delta t \boldsymbol{a}_0, & \boldsymbol{a}_1 &= F(\boldsymbol{r}_1, \boldsymbol{v}_1) \\
\boldsymbol{r}_2 &= \boldsymbol{v}_0 + 0.5\Delta t \boldsymbol{v}_1, & \boldsymbol{v}_2 &= \boldsymbol{v}_0 + 0.5\Delta t \boldsymbol{a}_1, & \boldsymbol{a}_2 &= F(\boldsymbol{r}_2, \boldsymbol{v}_2) \\
\boldsymbol{r}_3 &= \boldsymbol{v}_0 + \Delta t \boldsymbol{v}_2, & \boldsymbol{v}_3 &= \boldsymbol{v}_0 + \Delta t \boldsymbol{a}_2, & \boldsymbol{a}_3 &= F(\boldsymbol{r}_3, \boldsymbol{v}_3)
\end{aligned}
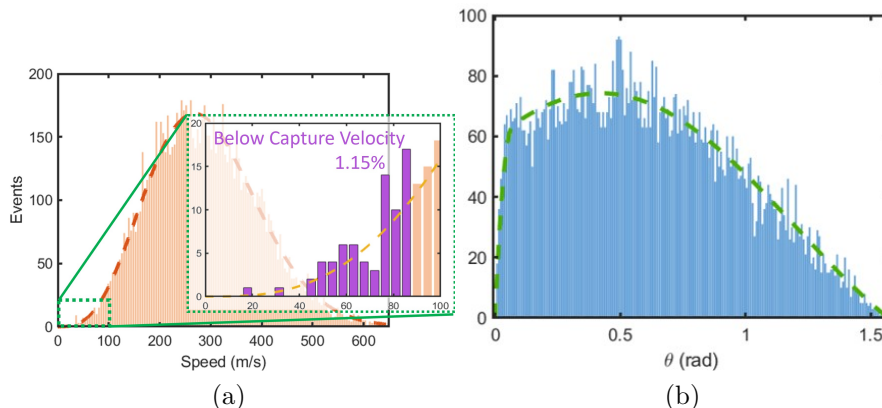\tag{4.4}
$$

Figure 4.3: An example of 50 000 sampled atom initial velocity (red and blue bars) comparing with exception value (red and green dash line). The oven temperature is 1000 °C, the tubed aperture radius $r_{\text{tube}} = 2.6$ mm and the length $L_{\text{tube}} = 60$ mm. **a)** The magnitude of sampled velocity. In order to show the Maxwell-Boltzmann distribution, it samples up to 650 m/s. But in simulation, the upper limitation is decreased. The purple bars in the small figure shows the fraction whose velocity is smaller than the capture velocity of 2D-MOT. It is only 1.15% of the total samples. **b)** The angular distribution of sampled velocity.

$$
\boldsymbol{v}(t_0 + \Delta t) = \boldsymbol{v}_0 + \frac{1}{6}\Delta t(\boldsymbol{a}_0 + 2\boldsymbol{a}_1 + 2\boldsymbol{a}_2 + \boldsymbol{a}_3)
$$
$$
\boldsymbol{r}(t_0 + \Delta t) = \boldsymbol{r}_0 + \frac{1}{6}\Delta t(\boldsymbol{v}_0 + 2\boldsymbol{v}_1 + 2\boldsymbol{v}_2 + \boldsymbol{v}_3)
$$
(4.5)

Afterwards, the new position $r(t_0 + \Delta t)$ and new velocity $v(t_0 + \Delta t)$ are used as the initial position and velocity. Such a loop repeats many times until it reaches the simulation time. Using the four-step Runge-Kutta methods, the error of the numerical solution is small than $O(\Delta t^5)$ and the accumulated error is smaller than $O(\Delta t^4)$.

4.1.3   MOT Loading Rate Estimation

In this section, we explain how we extract the MOT loading rate η from the simulation result. After simulating N_{sim} trajectories, we count the number of atoms N_{cap} which stay in a certain solid angle (for 2D-MOT) or in the MOT beam region (for the 3D-MOT). The total simulation time step is as large as all of the trajectories either converging to the center of the MOT or flying far away. We then estimate the loading rate via,

$$
\eta = \frac{N_{\text{cap}}}{N_{\text{sim}}}\Phi_{\text{sim}},
$$
(4.6)

where Φ_{sim} is the atomic flux which is accounted for in the simulation, specifically whose velocity is smaller than the cutting of velocity v_{cut}, and divergence angle θ_{lim} are under the limitation given by oven aperture. Then, we get

$$\Phi_{\text{sim}} = \Phi_{\text{oven}}(T) \times \int_0^{v_{\text{cut}}} P_{\text{v}}(v, T) \, \mathrm{d}v \times 2 \int_0^{\cos \theta_{\text{lim}}} j(\theta, T) \, \mathrm{d}\cos\theta, \qquad (4.7)$$

where Φ_{oven} is the atomic flow rate from Equ. (2.6), $P_{\text{v}}(v, T)$ the Maxwell-Boltzmann distribution from Equ. (2.3), and $j(\theta, T)$ is the angular distribution in transitional flow regime from Equ. (2.18).

4.2   Atomic Source Simulation

In this section, we go into more detail regarding our oven aperture design. In Ch.2, the theory of an atomic flux from a single aperture is introduced. The situation is more complex when a series of apertures is used. Fig. 4.4 shows the structure of our Dy effusion oven. It contains three apertures, 1) a tubed aperture starting from the end of the effusion cell and extending into the hot lip, 2) a thin-wall aperture at the end of the hot lip, and 3) another cold thin-wall aperture on the endcap aiming to cut the atomic beam at all angles larger than θ_{lim}. As described in the Master's Thesis of Johannes Schindler [75], in such a design the region between the first and second aperture forms a reservoir, the so-called hot lip reservoir. Here, we define a critical angle of atomic beam: the maximally allowed divergence angle θ_{lim} as the angle from an edge of the tubed aperture to the edge of the third aperture on the other side, as shown in Fig. 4.4. (a). The θ_{lim} gives the maximal divergence angle of the atomic beam from our oven. In order to avoid atoms coating on viewports, the θ_{lim} must be smaller than 15°. Especially, in our following discussion, the second aperture sometimes is so small that invading the 15° cone. In such a situation, the θ_{lim} will be defined by the edge of the second aperture instead of the third aperture.

In the situation with a Zeeman slower, the atomic beam is usually collimated into a small angle $\sim 3°$ [76, 75], because of the distance between the effusion oven and the first MOT. By contrast, in our design, the distance between the oven and 2D-MOT is significantly shortened. Therefore, the atomic beam is planned to be collimated into a relatively large angle of 15°, and the apertures 1 and 2 are designed such that the maximum of atoms stays within this cone. The first aperture is aiming to regulate the output atom flow rate from the effusion cell and perform initial collimation of the atomic beam. The second aperture at the end of the hot lip provides further collimation of the atomic beam. Finally, the cold third aperture cut the atomic beam at a certain angle in order to avoid atoms coating the viewports. Unlike the aperture-set design used with a Zeeman slower, in our case, the radius of all three apertures is extended for matching the large collimation angle. From the theory in Ch.2 section 2.2.3, we know that a hot aperture will always emit over the full space. In particular, there are always some atoms that get into the hot lip reservoir with a large angle. As a consequence, those atoms will hit and be reflected by the wall of the hot lip reservoir. After many reflections, a part of them goes back to the

(a)

(b)
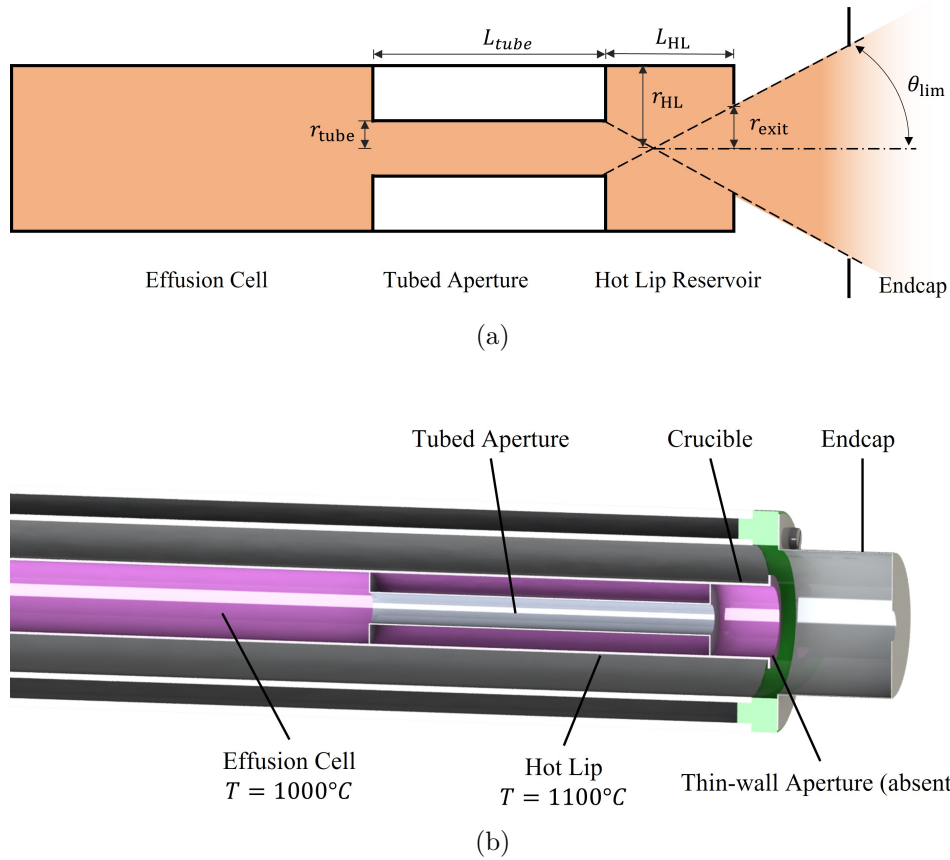
Figure 4.4: The structure of Dy effusion oven. **a)** A schematic **b)** 3D model of our oven. The thin-wall aperture between hot lip and endcap is absent. The endcap is connected to cooling water, such that it can act as a filter cutting the atomic beam.

effusion cell, but another part is still able to go through the second aperture. This part of atoms contributes to an angle out of our desired collimation, which makes the angular distribution far away from a single aperture. Aiming to investigate the angular distribution of atomic beam from our aperture set and optimize it, another MC simulation is done with a different aperture and hot lip geometries.

4.2.1   Tubed aperture

The first tubed aperture geometry is determined according to the lifetime of Dy in the effusion cell, as well as the MC simulation of the 2D-MOT loading rate (more details are introduced in the next section, section 4.3). The 2D-MOT simulation parameters are in Tab. 4.1. The volume of the effusion cell is limited to $25\,\mathrm{cc}^2$, and in order to produce a uniform atomic vapor, only less than one-third can be filled by Dy. The density of Dy is $8.540\,\mathrm{g/cm}^3$, so about $60\,\mathrm{g}$ of Dy can be filled into our oven. The upper limitation of atomic flow rate is 2.33×10^{15} atoms/s calculated

---
[2]The largest model from Createc

for a three-year and 24-7 running lifetime. While we found that we can only load about 20 g Dy into the effusion cell during installing our oven. On the other hand, in practice since the oven temperature is only increased when there is an experiment running, the lifetime is still expected to reach three years. Besides, the atomic flow rate is sensitive to temperature. Decreasing (increasing) a little bit of temperature can significantly extend(shorten) the lifetime of Dy. In our following calculation, we consider all of the atoms getting out of the tubed aperture are lost.

Fig. 4.5 reports the simulated loading rate and loading efficiency of 2D-MOT with different tubed aperture geometry. The loading efficiency is defined as the ratio of the loading rate and atomic flow rate. A higher loading efficiency means we have higher efficiency in making use of the atoms coming from the oven. The simulation starts at the end of the tubed aperture, and the influence of the hot lip reservoir is ignored (the reason is explained in the next section). A shorter length and a larger radius always provide a larger loading rate, since there are more atoms coming out of the oven. While the loaded efficiency is higher when a longer length and smaller radius are applied. Finally, the $L_{\text{tube}} = 60$ mm, $r_{\text{tube}} = 2.6$ mm is chosen. It provides a large atomic flux, but still stays within the limits of a three-year lifetime. With a certain atomic flux, a longer tube always provides a larger loading efficiency. But if the tube is much longer than the mean-free-path, 65.8 mm at 1000 °C, the atom-atom collision in the tubed aperture, which has been ignored, will have an influence. Accordingly, we choose a length $L_{\text{tube}} = 60$ mm on the order of mean free path. And a 2.6 mm radius is chosen in order to keep us away from the risk of being stacked.
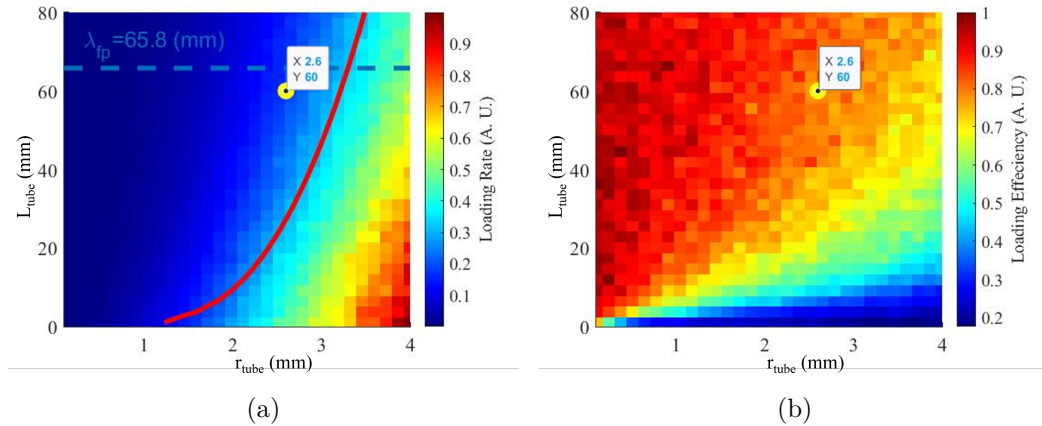
Figure 4.5: The simulation of 2D-MOT **a)** loading rate and **b)** loading efficiency with different tubed aperture. The red solid line is the contour line of 2.33×10^{15} atoms/s atomic flow rate out of the tubed aperture. On the its left (right) the atomic flow rate is lower(higher). The dash light blue line present the mean-free-path λ_{fp} of Dy at 1000 °C. The yellow dot shows our choice of tubed aperture geometry.

4.2.2   Hot lip reservoir

After determining the geometry of the first aperture, we then analyze the influence of the hot lip reservoir. Considering a fact, the Clausing factor (probability for atom traveling through) of the tubed aperture is smaller than 0.1. In addition, the hot lip reservoir has a larger radius than the tubed aperture. Thence the atomic density in the hot lip reservoir is smaller than that in the tubed aperture. In our following simulation, we assume the flow to be in the free molecular regime and make the same assumptions in Ch.2 section 2.2.4 for the free-molecular regime:

1. In each atom-wall collision, the Lambert's cosine law can be applied.

2. The collision between atoms can be ignored. And the atom-wall collision has a linear relationship Equ. (2.9) with the distance from the entrance of aperture.

Simulation for tubed aperture

We first check our simulation by calculating the angular distribution of the tubed aperture. Fig. 4.6 reports both theoretical prediction and MC simulation results of it, which are in good agreement. The theoretical prediction is given by the theory of free-molecular flow regime in Ch.2 (Equ. (2.12)). In MC simulation, after each collision, the atom velocity is resampled according to Lambert's cosine law.
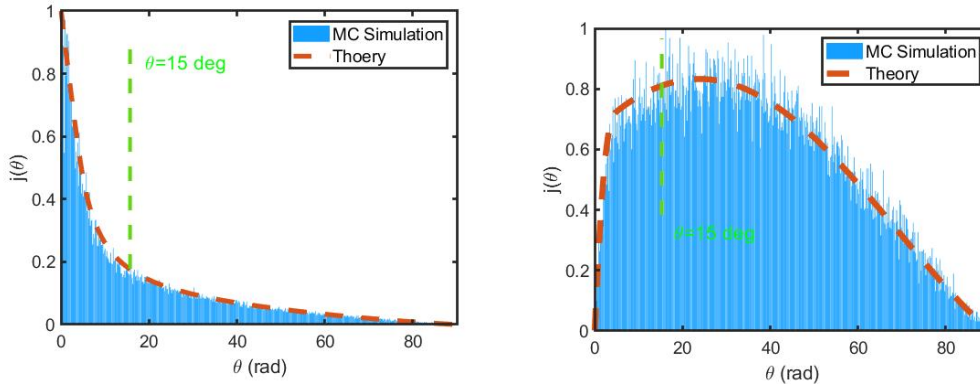
Figure 4.6: Angular distribution from a $L_{\text{tube}} = 60\,\text{mm}$, $r_{\text{tube}} = 2.6\,\text{mm}$ tubed aperture at $1000\,°\text{C}$. **a)** The angular distribution function. **b)** The number of atoms against emitting angle. Red dash line is the distribution function predicted by the theory in Chapter.2. The blue bar is the histogram figure of MC simulation results with 5×10^5 atoms. The atom emission angle $[0, 2\pi)$ is divided into 501 sub-region. The theoretical distribution without hot lip and simulation results are normalized with same factor. So the area under curve (for the theoretical distribution) and the summation area of blue bars (for the simulation result) represent the same number of atoms emitted from hot lip.

Simulation with fixed exit radius

Now we continue our simulation for a hot lip reservoir. Since the tubed aperture works in the transitional flow regime, instead of using the above result, we sampled the initial position and velocity of atoms at the exit of the tubed aperture. The angular distribution function of velocity is give by Equ. (2.18).

In order to give a general picture of how the hot lip reservoir influences the angular distribution, we firstly fixed the radius of the second aperture (the exit of the hot lip reservoir) at $r_{\text{exit}} = 2.6\,\text{mm}$ equaling to the radius of tubed aperture. The length of hop lip reservoir L_{HL} is changed from $20\,\text{mm}$ to $60\,\text{mm}$. The radius of the hot lip reservoir $r_{\text{HL}} = 5\,\text{mm}$ is given by the geometry of the crucible in our oven. Fig. 4.7 reports the simulation results of the angular distribution of the atoms at the output of the second aperture, together with the theoretical expectation without a hot lip reservoir. Both the theoretical distribution without the hot lip and simulation results are normalized to represent the same number of atoms emitted from the hot lip. Differently from the theoretical prediction without the reservoir (red dashed line), the angular distribution with the hot lip reservoir has two peaks. A narrow peak at a small angle, and another broader one at a large angle. As the length of the hot lip reservoir increases, the narrow peak becomes more and more narrow. This narrow peak is mostly resulting from the atoms traveling through the hot lip without collision, while the broader peak are resulting from the atoms "redistributed" by the wall of the hot lip reservoir. Since the radius of the second aperture is fixed, the atomic beam is collimated into a smaller angle with a long hot lip reservoir. As a result, the narrow peak shrinks when the length of the hot lip reservoir increases. The atoms, that collide with the hot lip wall, are reflected in all kinds of directions after at least once ideal diffuse reflection. In the case of reflected atoms, the collimation effect from the tubed aperture disappears and the angular distribution of those atoms is mainly like the angular distribution directly from a reservoir through a thin-wall aperture, which explains the broad peak. Moreover, in the simulation, all the atoms either go back to the tubed aperture or get out of the hot lip. Fig. 4.7.(f) shows the fraction of those two situations. when the length of the hot lip reservoir increases, the fraction of atoms that can go through the third cold aperture (staying in 15°) decreases, and the fraction of atoms going back also increases. An increased chance of an atom going back increases the density of atoms in the tubed aperture, which can lead to an increase in collision rate in the tubed aperture and further broaden the angular distribution.

From the above information, we can see that a hot lip reservoir can collimate the atomic beam by the second aperture at the exit. But it also decreases the total atomic flow rate getting out of the oven by sending a part of atoms back to the tubed aperture, which can also broaden the angular distribution. Besides, for the atoms that can not directly travel through, the hot lip reservoir decreases the collimation effect of the tubed aperture. So we then get clues for our design. First, with a $2.6\,\text{mm}$ radius of the second thin-wall aperture, the atomic beam is over-collimated compared with our requirement. Its radius r_{exit} should be changed for different hot lip reservoir length for matching with the 15° allowed divergence angle,

Figure 4.7: The number of atoms against emitting angle with different hot lip reservoir. The radius of the hot lip reservoir is fixed at $r_{HL} = 5\,\text{mm}$, while the length is changed among **a)** $20\,\text{mm}$, **b)** $30\,\text{mm}$, **c)** $40\,\text{mm}$, **d)** $50\,\text{mm}$, and **e)** $60\,\text{mm}$. The radius of the thin-wall aperture at the end of hot lip $r_{exit} = 2.6\,\text{mm}$. The red solid line is the theoretical prediction without any hot lip. The blue bar is the histogram figure of MC simulation results with 5×10^5 atoms. The theoretical distribution without hot lip and simulation results are both normalized by the total number of atoms leaving hot lip. The area under curve and the summation area of blue bars represent the same number of atoms emitted from hot lip. **f)** The fraction of atoms coming out of the hot lip and the fraction of useful atoms (which emitted into the 15° angle. The dash line shows the useful fraction without hot lip reservoir.

θ_{lim} in Fig. 4.4. Moreover, the atomic flow rate is better to not be decreased too much. In the experiment, we can only increase the atomic flow rate by increasing the temperature of the oven, which not only broadens the angular distribution but also decreases the lifetime of filled Dy rapidly. Last, if possible, we should also minimize the number of atoms going back.

Simulation with fixed divergence angle

In the next simulation, we change the length of hot lip reservoir L_{HL} from 20 mm to 28 mm. Meanwhile, the radius of second aperture r_{exit} is also changed for matching with the 15° allowed divergence angle, denoting as θ_{lim} (see Fig. 4.4). The upper bound of 28 mm is imposed by the radius of the hot lip. The lower bound of 20 mm is chosen to make sure $r_{\mathrm{exit}} > r_{\mathrm{tube}} = 2.6$ mm. This constraint ensures that the flux coming into the hot lip does not become larger than the flux coming out and the density of the atoms in the reservoir remains moderate. In the case where the density is large, multi-collisions are more likely to happen before an atom exits the hot lip, which makes the angular distribution broader. The simulation results are shown in Fig. 4.8. By changing the radius of the second aperture, we observe that the angular distribution keeps its two-peak shape. As expected from the fixed divergence angle, we observe that the width of the narrow peak at a small angle does not change with the length of the hot lip reservoir. On the other hand, the relative height of the narrow peak increases as the hot lip reservoir length increases. Meanwhile, both the fraction of useful atoms and getting back atoms to become higher with a long hot lip reservoir as reported in Fig. 4.8. (d). Because here a larger length corresponds to a larger aperture, and the probability of atoms hitting on the wall of the aperture and then reflecting back is smaller. On the other hand, a longer hot lip reservoir also means more collisions with the walls, which increases the risk of sending atoms back. From the unchanged width and increased height of the narrow peak, we can see that a longer hot lip reservoir helps send the atoms colliding with the walls back to the tubed aperture. Thus, we can make an important conclusion: it is also better to make the aperture as large as possible since it decreases the risk of atoms hitting on the aperture. In our design, we remove the second aperture, or in another word, use the end of the crucible as the second aperture.
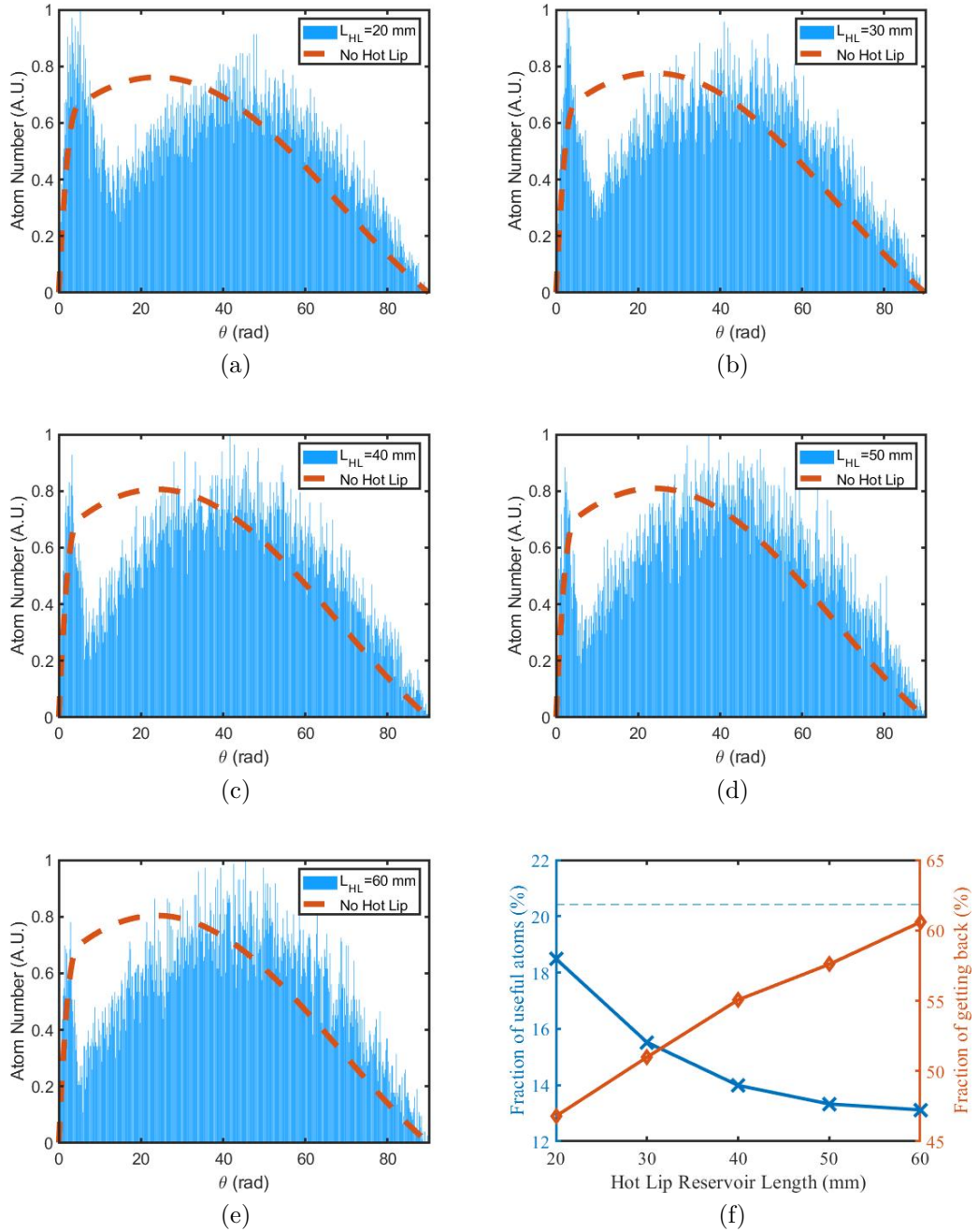
(a)

(b)

(c)

(d)
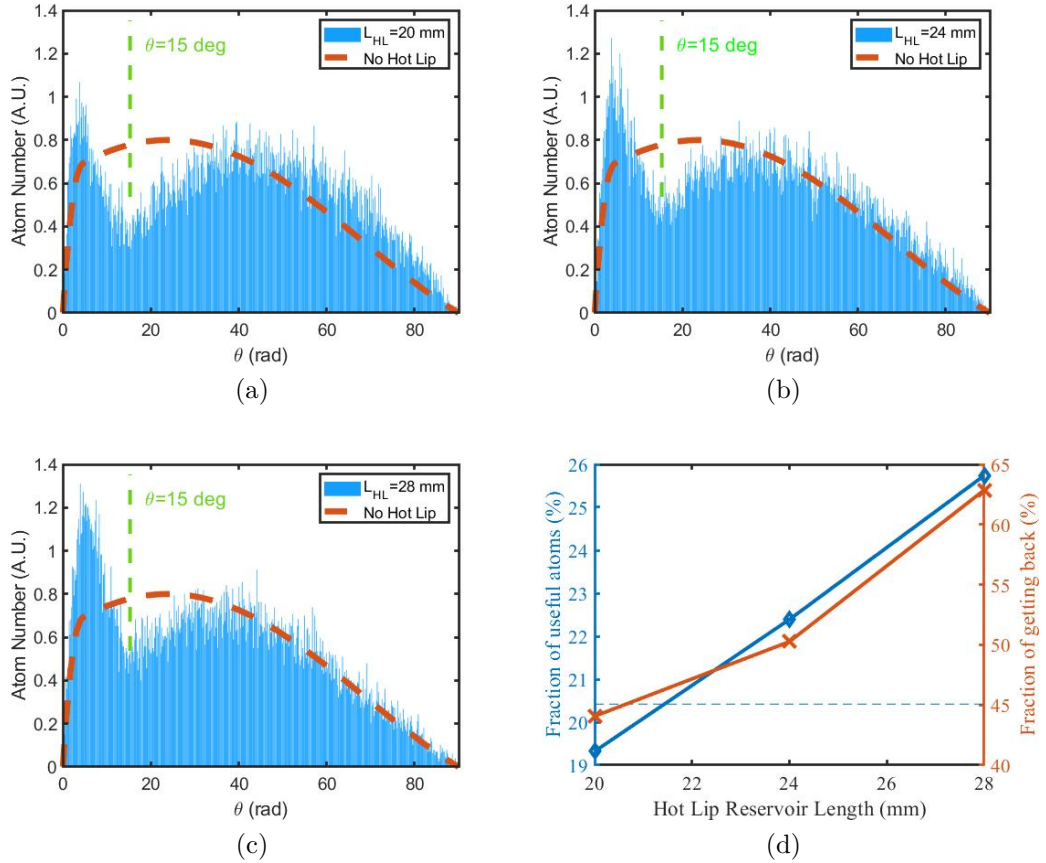
Figure 4.8: The number of atoms against emitting angle with different hot lip reservoir. The radius of the hot lip reservoir is fixed at $r_{\mathrm{HL}} = 5\,\mathrm{mm}$, while the length is changed among **a)** $20\,\mathrm{mm}$, **b)** $24\,\mathrm{mm}$, **c)** $28\,\mathrm{mm}$. Keeping the maximal allowed diverge angle to be $15°$, the radius of the thin-wall aperture at the end of hot lip is adapted with length. The atoms come from the effusion cell through a $r_{\mathrm{tube}} = 2.6\,\mathrm{mm}$ and $L_{\mathrm{tube}} = 60\,\mathrm{mm}$ tubed aperture. The red solid line is the theoretical prediction without any hot lip. The blue bar is the histogram figure of MC simulation results with 5×10^5 atoms. Both of them are normalized by the total number of atoms leaving hot lip. **d)** The fraction of atoms coming out of the hot lip and the fraction of useful atoms. The dash line shows the useful fraction without tubed aperture.

Simulation of our finial design

From the previous simulations, it seems now we find the best design of hot lip reservoir, $L_{\mathrm{HL}} = 28\,\mathrm{mm}$ and $r_{\mathrm{exit}} = 5\,\mathrm{mm}$. However, we notice that the maximum of the narrow peak in Fig. 4.8 locates at a relatively small angle compared to 15°. This design does not necessarily maximize the flow rate in the 15° angle out of the hot lip. Our purpose is not only to maximize the useful fraction of the atomic beam but also to maximize the atomic flow rate at 15°. Therefore, a third simulation is done, where we fixed the radius of second aperture at $r_{\mathrm{exit}} = 5\,\mathrm{mm}$, and decrease the hot lip reservoir L_{HL} from 28 mm to 17 mm and 10 mm. The simulation results are shown in Fig. 4.9. By decreasing the length of the hot lip reservoir, the width of the narrow peak increases, and the fraction of useful atoms first increases and then decreases. Meanwhile, the fraction of atoms getting back to the tubed aperture decrease, and the atomic flow rate out of the hot lip (given by the fraction of useful atoms times one minus the fraction of atoms going back) increases. Finally, we choose a length of the hot lip as $L_{\mathrm{HL}} = 10\,\mathrm{mm}$ to maximize the atomic flow rate, though it does not minimize the fraction of atoms out of 15°

(a)

(b)

(c)

(d)
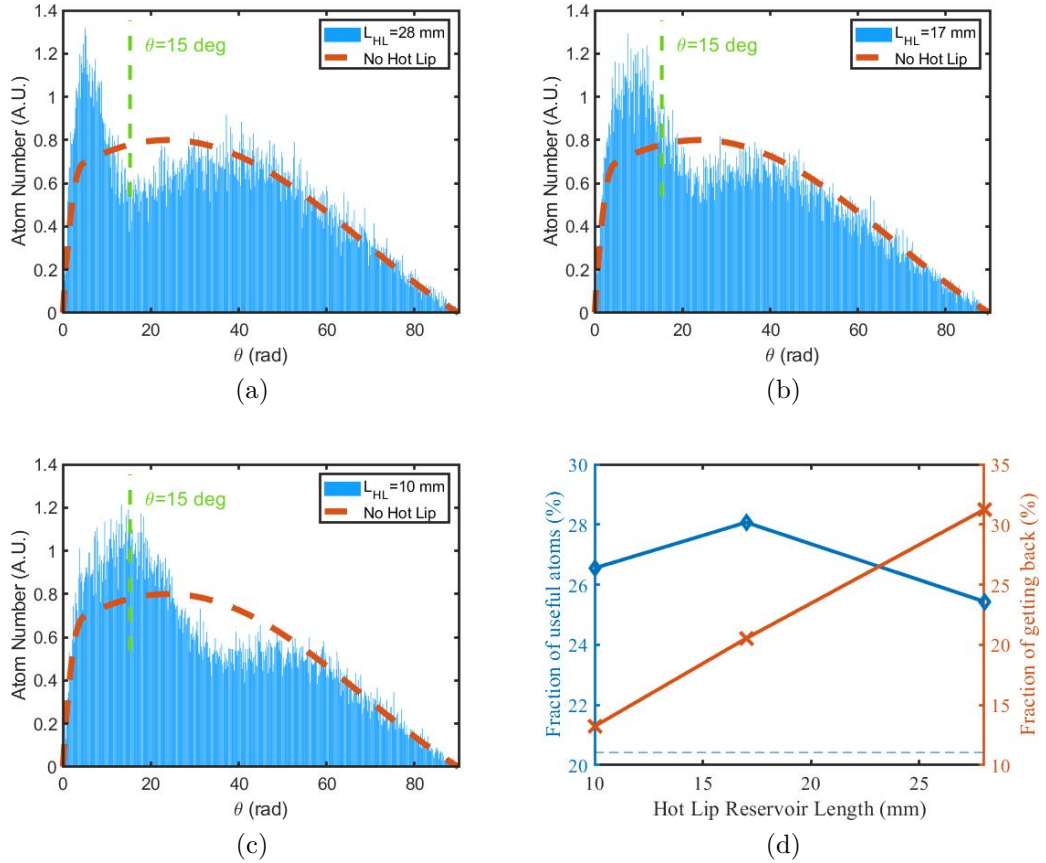
Figure 4.9: The number of atoms against emitting angle with different hot lip reservoir. The second thin-wall aperture at the end of hot lip is removed. The radius of the hot lip reservoir is fixed at $r_{\mathrm{HL}} = 5\,\mathrm{mm}$, while the length is changed among **a)** $28\,\mathrm{mm}$, **b)** $17\,\mathrm{mm}$, **c)** $10\,\mathrm{mm}$. The atoms come from the effusion cell through a $r_{\mathrm{tube}} = 2.6\,\mathrm{mm}$ and $L_{\mathrm{tube}} = 60\,\mathrm{mm}$ tubed aperture. The green dash line mark the position $\theta = 15°$. The red solid line is the theoretical prediction without any hot lip. The blue bar is the histogram figure of MC simulation results with 5×10^5 atoms. Both of them are normalized by the total number of atoms leaving hot lip. **d)** The fraction of atoms coming out of the hot lip and the fraction of useful atoms (which emitted into the $15°$ angle). The dash line shows the useful fraction without hot lip reservoir.

4.3   2D-MOT Loading Simulation

In this section, the MC simulation results for our 2D-MOT are discussed. The simulation parameters used for our 2D-MOT simulations are reported in Tab. 4.1. In each simulation, several parameters are changed, while all the other parameters are fixed to the values given in Tab. 4.1.

	symbol	value
Sampled Starting of Atom Position		
oven tubed aperture position (old endcap)	x_0	$-56.9\,\mathrm{mm}$
oven tubed aperture position (new endcap)	x_0	$-80.9\,\mathrm{mm}$
oven tubed aperture radius	r_{tube}	$2.6\,\mathrm{mm}$
oven tubed aperture length	L_{tube}	$60\,\mathrm{mm}$
Sampling Starting of Atom Velocity		
oven temperature	T_{oven}	$1000\,^{\circ}\mathrm{C}$
maximal allowed diverge angle (old endcap)	θ_{lim}	$15\,^{\circ}$
maximal allowed diverge angle (new endcap)	θ_{lim}	$7.5\,^{\circ}$
cutting off velocity	v_{cutoff}	$200\,\mathrm{m/s}$
2D-MOT Parameter		
magnetic gradient	b_{2D}	$34\,\mathrm{G/cm}$
laser power (per beam)	P_{2D}	$400\,\mathrm{mW}$
detuning	Δ_{2D}	$-1.8\,\Gamma$
e^{-2} beam waist	w_{2D}	$16\,\mathrm{mm}$
central saturation parameter (per beam)	s_{2D}	1.76
viewport clear aperture radius	r_{2D}	$17.5\,\mathrm{mm}$
Trajectory Solution Parameter		
time step	t_{step}	$50\,\mu\mathrm{s}$
total simulation time	t_{tot}	$4\,\mathrm{ms}$
simulated atom number	N_{atom}	50000

Table 4.1: The simulation parameter of 2D-MOT.

The simulation starts from the end of the tubed aperture in the Dy effusion oven and stops at the entrance of the differential pumping stage (19 mm away from the chamber center). In our case, the major constraints are laser power and chamber geometry. Although there is $\sim 800\,\mathrm{mW}$ at laser output, we have to divide our laser power into 2D-MOT, pushing beam, and also imaging. Besides, the maximal power we can send into a signal mode PM fiber is limited by heating effect, non-

linear scattering, and stimulated emission of color centers[3] [77, 78]. Meanwhile, the diameter of the CF40 viewport determines the maximal capture region of the MOT. Thus in the simulation, the laser power is fixed at $400\,\text{mW}$, and the laser beam is cut out by a circular aperture of $35\,\text{mm}$ diameter. The magnetic gradient, laser beam waist, and detuning are scanned to find the maximal loading rate. In addition, the influence of the distance between oven output and the 2D-MOT chamber is also investigated.

Fig. 4.10 shows the results of our parameter scanning for 2D-MOT loading rate. The maximal loading rate of $\sim 4.3 \times 10^{11}$ atoms/s[4] is found with a magnetic gradient $b_{2\text{D}} = 34\,\text{G/cm}$, beam waist $w_{2\text{D}} = 19\,\text{mm}$, and detuning $\Delta_{2\text{D}} = -1.6\,\Gamma$. We observe that the optimum beam waist $w_{2\text{D}} = 19\,\text{mm}$ is larger than the radius of viewport $r_{2\text{D}} = 17.5\,\text{mm}$. This suggests that the power distribution of the laser beam also has a significant influence on the loading rate. When the total saturation parameter from the effect of the four beams combined at the center of 2D-MOT is larger than 1 ($4 \times s_{2\text{D}} = 5.56$), increasing laser power gives a limited contribution to the increase of radiation pressure according to Equ. (2.38) and Equ. (2.30). In such a saturated situation, distributing the laser power more uniformly may lead to an increasing loading rate. In fact, the group of Selim Jochim at Heidelberg university founds theoretically that the loading rate of a MOT can be increased by using flat-top beams [79].

The simulation of Fig. 4.10 were performed using our initial oven aperture geometry, presented in section 3.3. Unfortunately, we met a problem of Dy coating in our experiment (see Ch. 3 section 3.4) and had to change the endcap in our oven. We had to increase $24\,\text{mm}$ to the distance between our oven and 2D-MOT, and decrease the allowed diverge angle of atomic beam θ_{lim} to $7.49°$. In order to analyse the changes in loading rate, two new simulations were done. In the first one, we change the position of tubed aperture x_0 from $-56.9\,\text{mm}$ to $-80.9\,\text{mm}$, and keep the θ_{lim} as $15°$. Fig. 4.11 reports the results of parameter scanning in the same range. The maximal loading rate $\sim 2.5 \times 10^{11}$ atoms/s is found at $b_{2\text{D}} = 34\,\text{G/cm}$, $w_{2\text{D}} = 16\,\text{mm}$, and $\Delta_{2\text{D}} = -1.8\,\Gamma$.

Due to the increased distance of oven, the angle from our oven towards the 2D-MOT becomes smaller. There are less atoms can reach the capture region of 2D-MOT. From the discussion in section 4.2.2, we know that most of atoms comes from the oven with an angle sightly smaller than $15°$, who can no longer reach the 2D-MOT after increasing the distance.

A third simulation is done with all the geometry given by our new endcap. The position of tubed aperture x_0 increases from $-56.9\,\text{mm}$ to $-80.9\,\text{mm}$, and the allowed diverge angle of atomic beam θ_{lim} decrease to $7.49°$. The simulation result is reported in Fig. 4.12. The maximal loading rate $\sim 2.5 \times 10^{11}$ atoms/s is found at $b_{2\text{D}} =$

---

[3]The calculation from my colleague, Karthik Chandrashekara, shows at $421\,\text{nm}$ maximal about $620\,\text{mW}$ can be transferred by a $3\,\text{m}$ PM fiber with a $3.5\,\mu\text{m}$ core based on stimulated Brillouin scattering.

[4]Here and in all the following simulations we did not take the abundance of ^{164}Dy in account, so the loading rate should be multiplied by 28.3%.
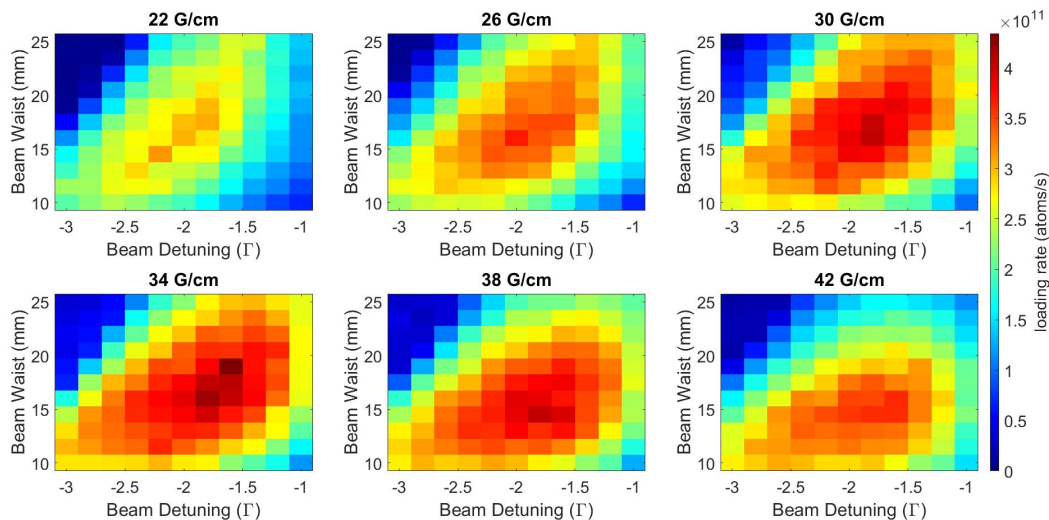
Figure 4.10: The parameter scanning simulation of 2D-MOT loading rate. The magnetic gradient b_{2D} is scanned from $22\,\mathrm{G/cm}$ to $42\,\mathrm{G/cm}$ in 6 steps, beam waist w_{2D} from $10\,\mathrm{mm}$ to $25\,\mathrm{mm}$ in 11 steps and detuning Δ_{2D} from $-3\,\Gamma$ to $-1\,\Gamma$ in 11 steps. The maximal loading rate $\sim 4.3 \times 10^{11}$ atoms/s is found at $b_{2D} = 34\,\mathrm{G/cm}$, $w_{2D} = 19\,\mathrm{mm}$, and $\Delta_{2D} = -1.6\,\Gamma$

$34\,\mathrm{G/cm}$, $w_{2D} = 16\,\mathrm{mm}$, and $\Delta_{2D} = -1.8\,\Gamma$. As a result of the increased oven and 2D-MOT distance, fewer atoms are likely to be captured. Therefore, the loading rate almost does not change, even if the θ_{lim} decreases by half. Additionally from a numerical perspective, using a smaller angle allowance, i.e. a more concentrated atomic beam also introduce less noise in the simulation, since fewer unnecessary trajectories are simulated.

To conclude, the new endcap design yields a reduction of 40% of the 2D-MOT loading rate, still keeping it very large with $\sim 2.5 \times 10^{11}$ atoms per second loaded in an optimal configuration. The optimal configuration is slightly shifted to small cooling beam waist ($w_{2D} = 16\,\mathrm{mm}$), smaller gradients ($b_{2D} = 34\,\mathrm{G/cm}$) and larger detuning ($\Delta_{2D} = -1.8\,\Gamma$)

4.4   Transferring and 3D-MOT Loading Simulation

After being loaded in the 2D-MOT, the atoms are transferred to the science chamber and re-captured by a 3D-MOT. Given by Equ. (2.50), the maximal capture velocity of a red 3D-MOT limited by CF40 flange is,

$$v_{\mathrm{3Dcap}} \approx 9.6\,\mathrm{m/s}. \tag{4.8}$$

This low capture velocity is problematic for loading the 3D MOT from 2D MOT due to the long distance between the centers of our 2 chambers ($34.7\,\mathrm{cm}$). As the atoms travel over this distance, they simultaneously fall under the effect of gravity and their fall is bigger when the atoms travel at low velocity. Even if the atoms fly
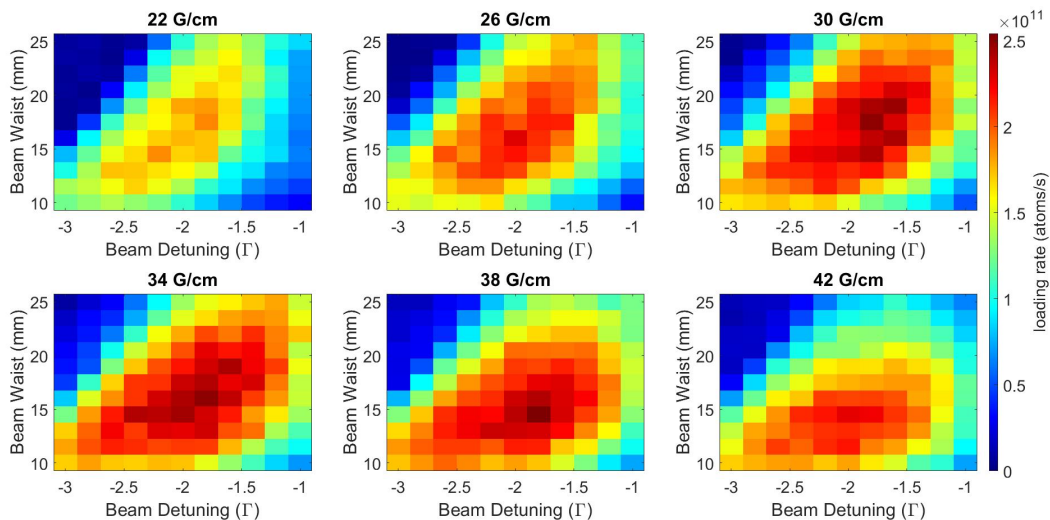
Figure 4.11: The parameter scanning simulation of 2D-MOT loading rate for new endcap. In this simulation the atomic beam is still cut in to $15°$. However the distance between tubed aperture and 2D-MOT chamber center is extended $24\,\text{mm}$ to $80.9\,\text{mm}$. The magnetic gradient is scanned from $22\,\text{G/cm}$ to $42\,\text{G/cm}$ in 6 steps, beam waist from $10\,\text{mm}$ to $25\,\text{mm}$ in 11 steps and detuning from $-3\,\Gamma$ to $-1\,\Gamma$ in 11 steps. The maximal loading rate $\sim 2.5 \times 10^{11}$ atoms/s is found at $b_{2D} = 34\,\text{G/cm}$, $w_{2D} = 16\,\text{mm}$, and $\Delta_{2D} = -1.8\,\Gamma$.

the distance $34.7\,\text{cm}$ between 2D- and 3D-MOT with a velocity equal to v_{3Dcap}, they will still fall more than $5\,\text{mm}$. Furthermore, from the discussion in Ch. 2 section 2.3.5, we know that the capture velocity will decrease if the atoms do not come along the central line of a MOT. In Fig. 4.13, we quantify how much an atom fall as a function of its initial velocity, for a traveling distance of $34.7\,\text{cm}$. A vicious circle is formed: a falling due to gravity leads to a decrease in capture velocity, and a decreased capture velocity leads to an increase in falling distance. Besides making the atoms fall, the gravity also makes the atomic beam more divergent as the small difference of atom velocity when exiting in the 2D-MOT yields different falling trajectories during traveling to 3D-MOT which amplifies the differences in velocities directions.

Inspired by the work of Jeff Thompson's group at Princeton university with ytterbium [80], a first solution is proposed: the push beam should be tilted and push the atoms with an angle so that when the atoms arrive at the 3D-MOT, they only have a horizontal velocity direction as shown in Fig. 4.14.(a). This solution solves the problem caused by falling, but also avoids the push beam going through the 3D-MOT and blowing atoms away. However, such a solution also requires a precision alignment of 2D- and 3D-MOT and fine control on the velocity of pushed atoms, which both are challenges in the experiment, and an exact agreement between simulation and experiments. Therefore, inspired by the work of Wolfgang Ketterle's group [81, 82], the idea of an angled slowing beam is proposed to increase the capture velocity of 3D-MOT. In this solution, two additional beams are shot against the
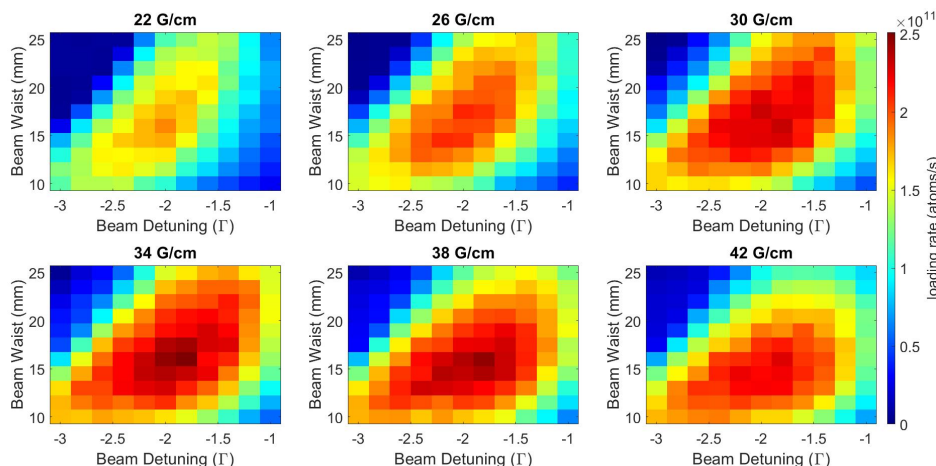
61

Figure 4.12: The parameter scanning simulation of 2D-MOT loading rate for new endcap. The new endcap length increases to $54\,\mathrm{mm}$ and the radius decreases to $9\,\mathrm{mm}$. The atomic beam is cut into a $7.49°$ angle. In this simulation, the position of tubed aperture and limited angle of atomic beam is changed accordingly. The magnetic gradient is scanned from $22\,\mathrm{G/cm}$ to $42\,\mathrm{G/cm}$ in 6 steps, beam waist from $10\,\mathrm{mm}$ to $25\,\mathrm{mm}$ in 11 steps and detuning from $-3\,\Gamma$ to $-1\,\Gamma$ in 11 steps. The maximal loading rate $\sim 2.5 \times 10^{11}$ atoms/s is found at $b_{2\mathrm{D}} = 34\,\mathrm{G/cm}$, $w_{2\mathrm{D}} = 16\,\mathrm{mm}$, and $\Delta_{2\mathrm{D}} = -1.8\,\Gamma$.

atoms towards the 3D-MOT in front of the 3D-MOT providing more deceleration as shown in Fig. 4.14.(b).

It is tricky to find the optimized parameters for the push beam, angled slowing beam, and 3D-MOT at the same time since they are all coupled to each other. With limited computing resources, it is impossible to scan all the involved parameters simultaneously. Therefore, we divide the optimization into three steps. First, we find the maximal capture velocity of the bare 3D-MOT by scanning its parameters. Then we add the two angled slowing beams and scan their parameters to maximize the increased capture velocity. Finally, another MC simulation is done to find the best parameter for the push beam.

4.4.1   Capture velocity of 3D-MOT

Fig. 4.15 reports the parameter scanning results of 3D-MOT capture velocity. The atoms start $30\,\mathrm{mm}$ away from the center of 3D-MOT. The maximal capture velocity $9.1\,\mathrm{m/s}$ is found with a magnetic gradient $b_{3\mathrm{D}} = 1\,\mathrm{G/cm}$, beam waist $w_{3\mathrm{D}} = 14.5 \sim 19.0\,\mathrm{mm}$, and detuning $\Delta_{3\mathrm{D}} = -45\,\Gamma$. In following discussion, the beam waist of 3D-MOT $w_{3\mathrm{D}}$ is decided to be $15\,\mathrm{mm}$.

It is noticed that from small detuning the capture velocity increases as the detuning increases, but the capture velocity suddenly decreases at center detuning. From the discussion in Ch. 2 section 2.3.5 as well as shown in Fig. 4.16 .(b), we know that the MOT create two "cloud" of decelerating force in phase space. According to
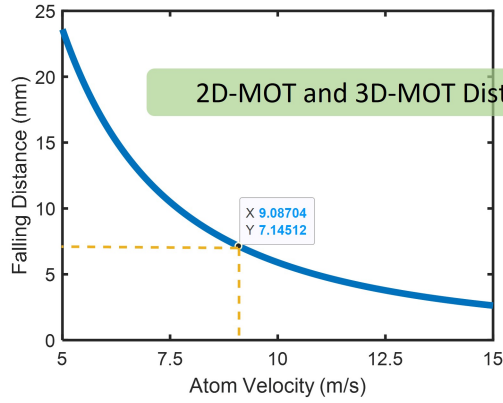
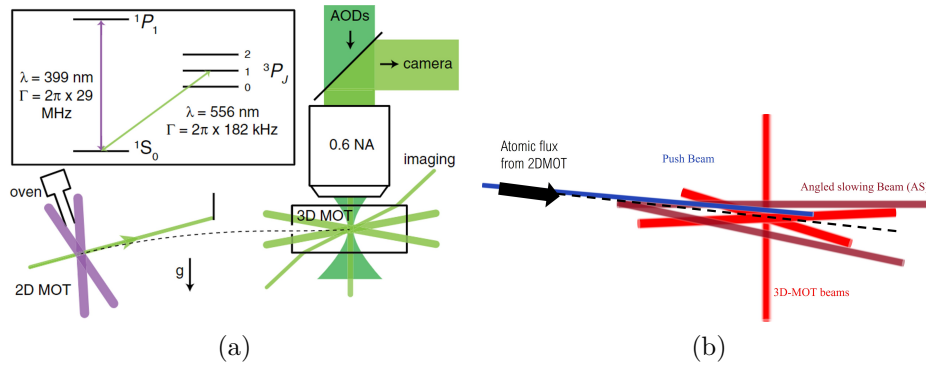Figure 4.13: The relationship of atom velocity and falling distance during transferring from 2D-MOT to 3D-MOT.

(a) (b)

Figure 4.14: **a)**The idea of using a tilted push beam with ytterbium experiment used in Jeff Thompson group in Princeton university. The picture is taken from Ref. [80].**b)**The configuration of 3D-MOT with a tilted push beam and two angled slowing beams.

Equ. (2.44), the vertical separation of those two "clouds" is determined by laser detuning. Starting from small detuning, a larger detuning leads to a larger separation corresponding to a larger capture velocity. However, if the detuning is too large, the atoms can be decelerated but not down to zero velocity: the trapping effect of the MOT is too weak to trap those atoms.

4.4.2 Capture velocity increased using angled slowing beams

As discussed before, the angle slowing beams provide additional deceleration before 3D-MOT. If we used the blue transition for angled slowing beams, an extremely large detuning would be necessary due to the large natural linewidth, otherwise the atoms would be decelerated too much and pushed away from 3D-MOT. Therefore, we decided to use the red transition for the angled slowing beams. From the discussion in Ch. 2 section 2.3.5, when the laser power is fully saturated, the deceleration mainly depends on the size of the beam. Therefore, the angled slowing beams provide the
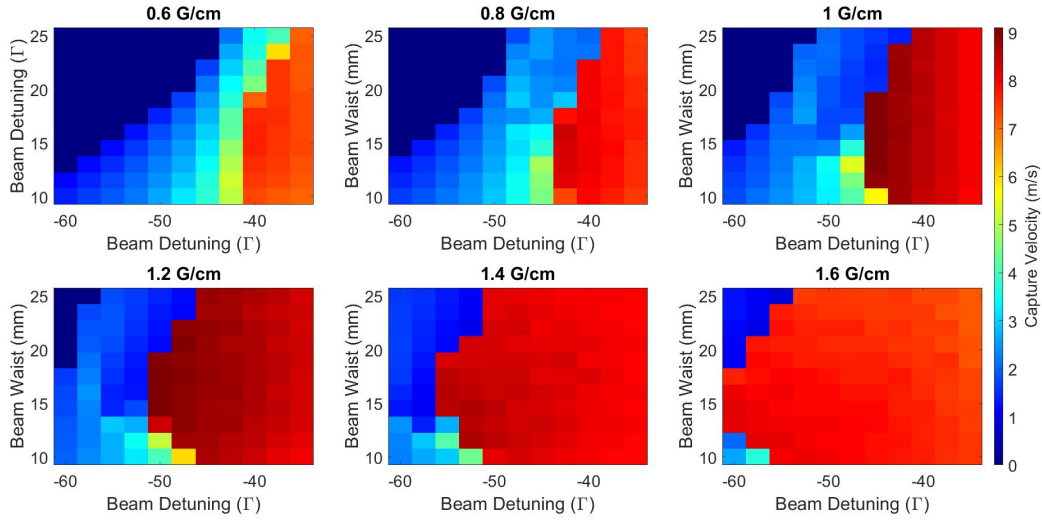
Figure 4.15: The parameter scanning to find the largest central-line capture velocity of 3D-MOT. The magnetic gradient b_{3D} is scanned from $0.6\,\mathrm{G/cm}$ to $1.6\,\mathrm{G/cm}$ in 6 steps, beam waist w_{3D} from $10\,\mathrm{mm}$ to $25\,\mathrm{mm}$ in 11 steps and detuning Δ_{3D} from $-35\,\Gamma$ to $-60\,\Gamma$ in 11 steps. The maximal capture velocity $9.1\,\mathrm{m/s}$ is found at $b_{3D} = 1\,\mathrm{G/cm}$, $w_{3D} = 14.5 \sim 19.0\,\mathrm{mm}$, and $\Delta_{3D} = -45\,\Gamma$.

maximal deceleration, when the projection of the light beams onto the atomic beam from 2D-MOT is maximized. Combining the geometry constraints of the science chamber, it turns out that the angle between the angled slowing beams and atomic beam from 2D-MOT is 22.5°.

In the following simulation, the angled slowing beam is set to be π polarized excluding the influence of the magnetic field on the detuning of the transition. This is experimentally relevant since in the region far away from the 3D-MOT center, the Equ. (2.48) is no longer a good approximation and the magnetic field values are not well known in the angled slowing regions. Fig. 4.16. (a) reports the trajectories of atoms in the 3D-MOT with angled slowing beams. The two tilted deceleration "clouds" are contributed by the 3D-MOT and another horizontal one is contributed by the angled slowing beams. In this figure, the detuning of angled slowing beams is $-120\,\mathrm{Gamma}$ corresponds to a $10.14\,\mathrm{m/s}$ velocity. We can see that if the detuning of the angled slowing beams is too larger, it can still decelerate the atoms, but the slowed atoms will not be captured in the 3D-MOT. On the other hand, if the detuning of the angled slowing beams is too small, it will overlap with the 3D-MOT. Therefore, we scan the detuning and beam waist of the angled slowing beams to find the maximal capture velocity, and the results are reported in Fig. 4.16. (b). From the scanning results, we observed a suitable detuning for the angled slowing beams is about $-120\,\mathrm{Gamma}$. Besides, when the beam waist the smaller, the power broaden is larger. Therefore, for a smaller beam waist, the range of suitable detuning is larger. Finally, the beam waist of the angled slowing beam is chosen as $14.5\,\mathrm{mm}$, which is similar to the 3D-MOT beam, and they can share the design of the fiber collimator and telescope. The complete list of parameters for angled slowing beams

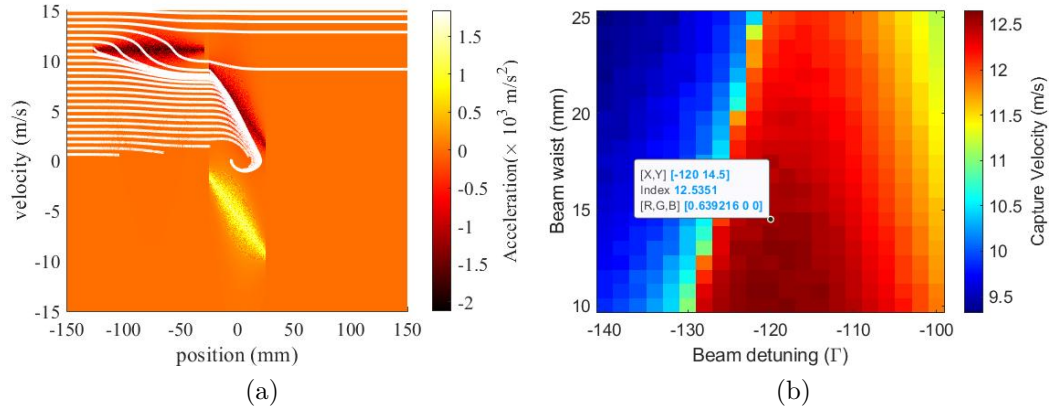is decided to be similar to 3D-MOT given in Tab. 4.2.

Figure 4.16: **a)** The phase space plot of the atoms trajectories in the 3D-MOT with angled slowing beams. **b)** The parameter scanning of 3D-MOT capture velocity with angled slowing beams. The parameters used in this simulation is given in Tab. 4.2

4.4.3   Push beam

After determining the parameters for 2D- and 3D-MOT, only the push beam remains to be optimized. There are three parameters for the push beam: the tilting angle, the power, and the detuning. The velocity distribution of atoms trapped in the 2D-MOT can be considered as a broad distribution centered around zero since there is no trapping along the push beam.

Before going further, there is one important question need to be answered: which transition should be used for the push beam. In the following, we will show the optimization principle for both the blue and red push beam. For the blue push beam, due to the broad linewidth, it has to be tilted to avoid going through the 3D-MOT, which is unnecessary for the red push beam. As illustrated in the previous application of Fig. 4.16. (a), the narrow red transition can only interact with atoms in a relatively small velocity range. We decided to study the influence of the red push beam without angled slowing beams, which also matches our current configuration of experiments.

Tilted blue pushing beam

The beam waist of blue push beams w_{push} is chosen to match the 1 mm radius of the differential pumping stage (DPS). And the beam intensity is cut off at 1.2 mm radius since the size of 2D-MOT is much smaller than the beam waist. In the simulation, the blue push beam is set as π polarized since the magnetic gradient along the push beam is very small. From Equ. (2.30), it is noticed that both the power and detuning contribute to radiation pressure through and only through the saturation parameter.

	symbol	value
3D-MOT Parameter		
maggnetic gradient	b_{3D}	$1\,G/cm$
laser power (per beam)	P_{3D}	$100\,mW$
detuning	Δ_{3D}	$-45\,\Gamma$
$e^{-}2$ beam waist	w_{3D}	$17.5\,mm$
central saturation parameter (per beam)	s_{3D}	1.39
viewport clear aperture radius	r_{3D}	$17.5\,mm$
Angled slowing beam Parameter		
laser power (per beam)	P_{Ang}	$50\,mW$
detuning	Δ_{Ang}	$-120\,\Gamma$
$e^{-}2$ beam waist	w_{Ang}	$17.5\,mm$
central saturation parameter (per beam)	s_{Ang}	1.39
Trajectory Solution Parameter		
time step	t_{step}	$3000\,\mu s$
total simulation time	t_{tot}	$75\,ms$
simulated atom number	N_{atom}	50000

Table 4.2: The simulation parameter of the 3D-MOT.

Therefore, in the first place, the influence of the power and detuning of the blue push beam can be considered the same factor. We first fix the power of the blue push beam at $3\,mW$ and scan the detuning and tilting angle. The scanning result is shown in Fig. 4.17 (a). The maximal loading rate $\sim 5 \times 10^{10}$ atoms/s is found with tilting angle $2° \sim 2.5°$ and detuning $-10 \sim -8\,\Gamma$. With center beam power, a smaller detuning leads to a larger velocity after pushing. A larger tilting angle is necessary to make sure the horizontal velocity component is smaller than the capture velocity of the 3D-MOT. Afterward, we also scan the beam power and detuning with a fixed tilting angle at $2.5°$. The scanning result is reported in Fig. 4.17 (b). The maximal loading rate is found not only at the center point, but as a line in the plot. It confirms that the influence of the power and detuning of the blue push beam can be considered the same factor. However, with a small beam power, the range of suitable detuning is smaller. It shows that when the power is smaller, the loading rate will be more sensitive to the detuning, which may bring difficulties in experiments. On the other hand, it is also not very easy to produce a large detuning in experiments. Eventually, we decided to choose a detuning around $-8\,\Gamma$ for the blue push beam yielding optimal power on the order of few mW.
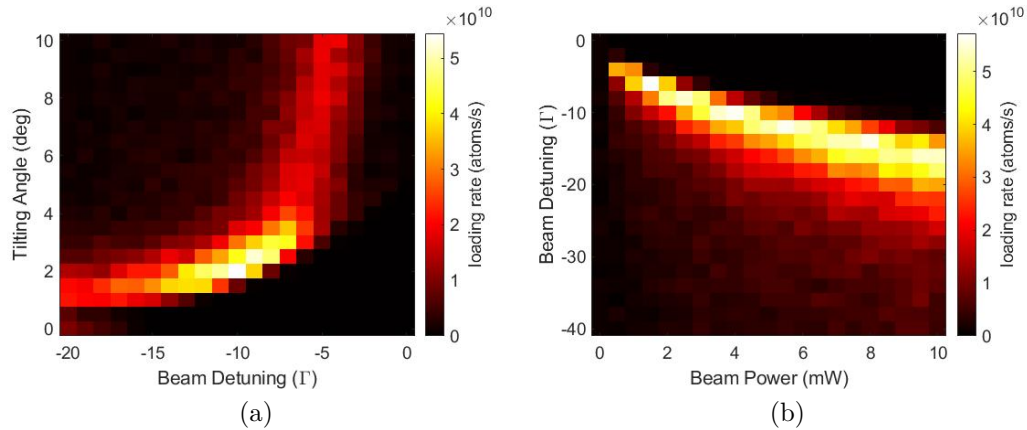
Figure 4.17: **a)**The parameter scanning of the blue push beam tilting angle and detuning with 3 mW power. **b)**The parameter scanning of the blue push beam power and detuning with 2.5° tilting angle. The parameters used in this simulation is given in Tab. 4.3

	symbol	value
Blue Push Beam Parameter		
laser power (per beam)	P_{Bpush}	3 mW
detuning	Δ_{Bpush}	$-8\,\Gamma$
e^-2 beam waist	w_{Bpush}	1 mm
central saturation parameter (per beam)	s_{Bpush}	3.39
cutoff beam radius	r_{Bpush}	1.2 mm
tilting angle		2.5°
Trajectory Solution Parameter		
time step	t_{step}	200 μs
total simulation time	t_{tot}	100 ms
simulated atom number	N_{atom}	50000

Table 4.3: The simulation parameters of the blue push beam.

Red pushing beam without angled slowing beam

The beam waist of the red push beams w_{push} is chosen to be 0.72 mm, which is close to the radius of DPS and can be easily achieved with our current fiber and collimator. The beam intensity is still cutoff at 1.2 mm radius. The polarization also keeps being π polarization. Fig. 4.18 reports the scanning results of beam power and detuning for the red push beam. We can see that at 0 detuning, almost no atoms are loaded into the 3D-MOT since an on-resonance push beam can push all the loaded atoms away from the 3D-MOT. When the red push beam is red detuned (detuning

is negative), it can push the atoms going in the wrong direction back towards the 3D-MOT. In this regime, it is favorable to use more power to broaden the transition in order to interact with a large velocity range. On the other hand, when the red push beam is blue detuned (detuning is positive), it can accelerate the atoms going towards the 3D-MOT but slower than the capture velocity of 3D-MOT to the capture velocity. However, if the atoms are accelerated beyond the capture velocity, they can never be captured by the 3D-MOT. In this regime, the maximal loading rate is found at a small beam power, and there are no atoms loaded with large beam power. In this simulation, we find an overall optimum for the loading rate in the blue-detuned region (5×10^8 atoms/s) but this is very narrow in detuning and power ranges. A broader but weaker optimum is found in the red-detuning regime (with $\approx 3.5 \times 10^8$ atoms/s).
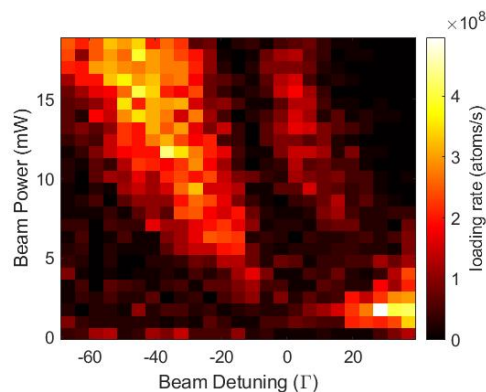

Figure 4.18: The parameter scanning of the red push beam power and detuning. The parameters used in this simulation is given in Tab. 4.4

4.5   First Experiment Result

Up to now, we successfully observed the 2D-MOT and 3D-MOT without the push in the experiment, and the optimization of our system is still ongoing. Here we can only give the experiment results we have in the first step. Fig. 4.19 shows the current state of our lab with 2D-MOT and 3D-MOT laser beams on.

Fig. 4.20 (a) and (b) show pictures of our 2D-MOT with the old oven endcap and the new endcap, respectively. In the pictures, the 2D-MOT is achieved with a beam power about 460 mW, magnetic gradient about 33 G/cm and a detuning about 2 Γ. The narrow bright blue line is the fluorescence of the 2D-MOT and the blue cone is the fluorescence of the atomic beam from the oven. Compared with the fluorescence, it is clear the atomic beam coming from the oven is at a smaller angle after changing the new endcap. Fig. 4.20 (c) shows pictures of our 3D-MOT with the old oven endcap. The 3D-MOT is achieved with a beam power about 90 mW, magnetic gradient about 4.2 G/cm and a detuning about −50 Γ.

The process of the optimization of our MOT is still ongoing. An absorption imaging system for the 3D-MOT is also built with a C11440-36U Complementary

	symbol	value
Red Push Beam Parameter		
laser power (per beam)	P_{Rpush}	$1.73\,\mathrm{mW}$
detuning	Δ_{Rpush}	$28.4\,\Gamma$
e^{-2} beam waist	w_{Rpush}	$0.72\,\mathrm{mm}$
central saturation parameter (per beam)	s_{Rpush}	2950
cutoff beam radius	r_{Rpush}	$1.2\,\mathrm{mm}$
tilting angle		$0°$
Trajectory Solution Parameter		
time step	t_{step}	$200\,\mu\mathrm{s}$
total simulation time	t_{tot}	$100\,\mathrm{ms}$
simulated atom number	N_{atom}	50000

Table 4.4: The simulation parameters of the red push beam.
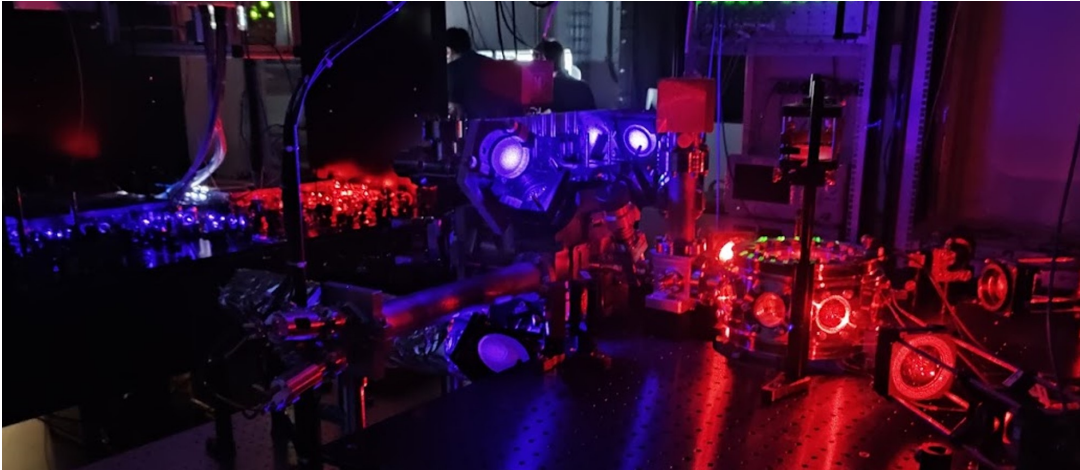
Figure 4.19: A picture of our lab with 2D-MOT and 3D-MOT laser beams on

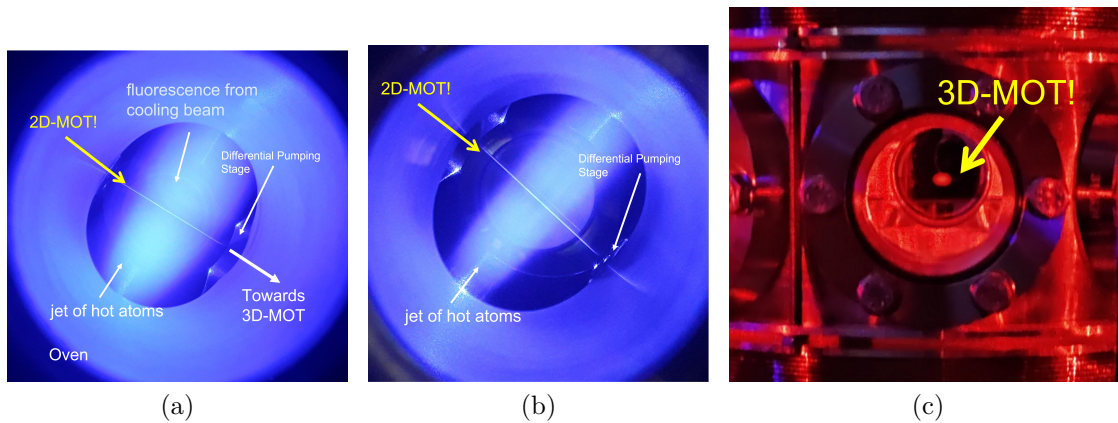|	unit	Simulation	Experiments
Laser power (per beam)	mW	400	~ 460
Magnetic gradient	G/cm	34	31.0
Beam waist	mm	16	15.50(0.29)
Saturation parameter (per beam)		1.39	2.14
Detuning	Γ	-1.8	-2.36

Table 4.5: The simulation parameter of the push beam.

Figure 4.20: **a)**A picture of our 2D-MOT with the old oven endcap. **b)**A picture of our 2D-MOT with the new oven endcap. **c)** An picture of our 3D-MOT. All three pictures are taken by phone.

metal–oxide–semiconductor (CMOS) camera from *Hamamatsu Photonics*. The 3D-MOT is firstly optimized and the 2D-MOT is then optimized based on the optimized 3D-MOT. During both the optimization of 2D- and 3D-MOT, we always try to find the maximal absorption signal in 3D-MOT after a fixed loading time. So far the optimized parameters we found for the 2D-MOT are reported in Tab. 4.5 and the optimized parameters of 3D-MOT are reported in Joschka Schöner's Master thesis [68]. However, we also noticed that it is possible to realize the MOT over a wide range of quite different parameters. The final optimized parameters might be different from what we found now. As the imaging system is not fully calibrated, we can not give an accurate number of atoms we loaded into our 3D-MOT. But we estimate it to be in the order of 10^8 atoms with a loading rate of 3×10^7 atoms/s without push beam.

5 | Conclusion and Outlook

The main aim of this thesis is to design and build a novel slow beam source of ^{164}Dy based on a 2D MOT, that will later serve as achieving quantum degeneracy gases. Up to now, we successfully built the vacuum and laser system, and observe the fluorescence signal in 2D-MOT and 3D-MOT (without the push beam and angled slowing beams). In Ch. 3, we report the building process of our vacuum system generating a necessary vacuum environment, as well as the laser system with frequency stabilized by the PDH locking method. In Ch. 4, we report the design process of our 2D-MOT as the first slow atomic source of Dy applied in ultracold atom experiments. A set of simulations based on Monte-Carlo methods are done providing clues and guidelines for the apparatus design and experimental realization.

In our novel experiment design, based on a 2D-MOT source, the oven is directly inserted into the 2D-MOT chamber. A short oven-MOT distance has the potential of increasing the loading rate by increasing the capturing probabilities of those atoms with a large incident angle. Due to the different requirements of the atomic beam compared to Zeeman slower apparatus, the set of apertures in the oven is also re-designed by ourselves. We extend the length of the first tubed aperture to 60 mm and the radius to 2.6 mm matching our new collimation requirement of the atomic beam and avoiding the risk of being stuck the aperture. Besides, the second thin-wall aperture is removed, or in another word, the end of the crucible works as the second thin-wall aperture. The distance between the first tubed aperture and the end of the crucible is also optimized according to the atomic flow rate. A third water-cooled aperture on the endcap of the oven is used to block the direct line of the atomic beam to the viewports.

The range of the parameters of 2D-MOT is determined by a Monte-Carlo simulation of the atom trajectories. By scanning the parameters, we found the maximal loading rate is achieved with a magnetic gradient $b_{2D} = 34$ G/cm, beam waist $w_{2D} = 16$ mm, and detuning $\Delta_{2D} = -1.8\,\Gamma$. Afterward, it is found that gravity combined with the small linewidth of the 3D-MOT transition caused difficulties in transferring the atoms from 2D-MOT to 3D-MOT. We optimized our chance of capturing atoms by designing large 3d-MOT beams and planned for additional schemes to further increase the capture velocity, in particular, based on angled slowing beams. In the simulation, only a few atoms can be re-captured in a 3D MOT without angled slowing beams. We propose two solutions: tilt the push beam by a 2.5° angle and add two angled slowing beams in the front of 3D-MOT. The range of the parameters for 3D-MOT, push beam, and angled slowing beam is also deter-

mined by Monte-Carlo simulations. Until now, the optimization of both 2D- and 3D-MOT in the experiment is still ongoing, but we already successfully load about 10^8 atoms to the 3D-MOT without push beam and angled slowing beams. Such a result in experiments is surprisingly good compared to simulation.

On the other hand, we also noticed that there is space for future improvements. In our current setup, the endcap is re-designed to avoid Dy atoms coating the viewports. However, the design of apertures in the oven is optimized for the old endcap design. The unmatched design makes a few Dy atoms unnecessarily wasted. We would like to suggest re-optimize the design of the oven aperture in order to match the new endcap design.

All in all, the successful observation of our 3D-MOT already shows we are on a good track and we are confident to achieve the BEC state of Dy in the near future.

A | Implementation of Simulation Program

A.1 Program structure

Our simulation program is accessible from our git serves by following link,

`https://git.physi.uni-heidelberg.de/DyLab/Calculations/src/branch/master/2DMOT_Simulation`

In this section, we introduce the basic structure of our codes. After several development iterations, the main body of simulation program is written in C++ based on objections and classes, aiming to accelerate calculation speed and keep compatibility with any ohter MOT configurations or even other atom pieces. Meanwhile, benefiting from the easy-use interface between C++ and Matlab, the initialization, data analization and plotting parts are still finished in Matlab, because of the fully developed tool boxes in Matlab. Besides, the user-friend parallel computation in Matlab also help us saving plenty of calculation time. All in one sentence, we find a balance point bewteen time consumption and user friendship by making a Matlab shell of a C++ program. Then the C++ program can be treated as a black box for calculating the atom trajectory in a light field. Our program can be easy adapted for other atoms just by changing the constants in the Matlab shell.

A.2 Simulation System Environment

All of the simulations in this thesis in run by the same computer. The operation system of the computer is *Windows 11 Home* of version 21H2 (64-bit). It has a 3.10 GHz i5-10500 CPU from *Intel* and 16.0 GB RAM. We use the 2021a version of *MATLAB* and *Microsoft Visual C++ 2019* for building the C++ scripts.

B | Bibliography

[1] Steven Chu and Carl Wieman. Laser cooling and trapping of atoms: Introduction. *JOSA B*, 6(11):2020–2022, 1989.

[2] H.J. Metcalf, P. Van der Straten, J.L. Birman, J.W. Lynn, H.E. Stanley, M.P. Silverman, and M. Voloshin. *Laser Cooling and Trapping*. Graduate texts in contemporary physics. Springer, 1999.

[3] Florian Schreck and Klaasjan van Druten. Laser cooling for quantum gases. *Nature Physics*, 17(12):1296–1304, 2021.

[4] Christopher J Pethick and Henrik Smith. *Bose–Einstein condensation in dilute gases*. Cambridge university press, 2008.

[5] Andrew D Ludlow, Martin M Boyd, Jun Ye, Ekkehard Peik, and Piet O Schmidt. Optical atomic clocks. *Reviews of Modern Physics*, 87(2):637, 2015.

[6] Alexander D Cronin, Jörg Schmiedmayer, and David E Pritchard. Optics and interferometry with atoms and molecules. *Reviews of Modern Physics*, 81(3):1051, 2009.

[7] B Canuel, A Bertoldi, L Amand, E Pozzo di Borgo, T Chantrait, C Danquigny, Miguel Dovale Álvarez, B Fang, Andreas Freise, R Geiger, et al. Exploring gravity with the miga large scale atom interferometer. *Scientific Reports*, 8(1):1–23, 2018.

[8] Marco Cerezo, Andrew Arrasmith, Ryan Babbush, Simon C Benjamin, Suguru Endo, Keisuke Fujii, Jarrod R McClean, Kosuke Mitarai, Xiao Yuan, Lukasz Cincio, et al. Variational quantum algorithms. *Nature Reviews Physics*, 3(9):625–644, 2021.

[9] Khabat Heshami, Duncan G England, Peter C Humphreys, Philip J Bustard, Victor M Acosta, Joshua Nunn, and Benjamin J Sussman. Quantum memories: emerging applications and recent advances. *Journal of modern optics*, 63(20):2005–2028, 2016.

[10] William D Phillips. Nobel lecture: Laser cooling and trapping of neutral atoms. *Reviews of Modern Physics*, 70(3):721, 1998.

[11] Steven Chu. Nobel lecture: The manipulation of neutral particles. *Reviews of Modern Physics*, 70(3):685, 1998.

[12] Claude N Cohen-Tannoudji. Nobel lecture: Manipulating atoms with photons. *Reviews of Modern Physics*, 70(3):707, 1998.

[13] A Einstein. Quantum theory of a monoatomic ideal gas a translation of quantentheorie des einatomigen idealen gases (einstein, 1924), 1925.

[14] Enrico Fermi. Zur quantelung des idealen einatomigen gases. *Zeitschrift für Physik*, 36(11):902–912, 1926.

[15] Paul Adrien Maurice Dirac. On the theory of quantum mechanics. *Proceedings of the Royal Society of London. Series A, Containing Papers of a Mathematical and Physical Character*, 112(762):661–677, 1926.

[16] Mike H Anderson, Jason R Ensher, Michael R Matthews, Carl E Wieman, and Eric A Cornell. Observation of bose-einstein condensation in a dilute atomic vapor. *science*, 269(5221):198–201, 1995.

[17] Kendall B Davis, M-O Mewes, Michael R Andrews, Nicolaas J van Druten, Dallin S Durfee, DM Kurn, and Wolfgang Ketterle. Bose-einstein condensation in a gas of sodium atoms. *Physical review letters*, 75(22):3969, 1995.

[18] Eric A Cornell and Carl E Wieman. Nobel lecture: Bose-einstein condensation in a dilute gas, the first 70 years and some recent experiments. *Reviews of Modern Physics*, 74(3):875, 2002.

[19] Wolfgang Ketterle. Nobel lecture: When atoms behave as waves: Bose-einstein condensation and the atom laser. *Reviews of Modern Physics*, 74(4):1131, 2002.

[20] Dale G Fried, Thomas C Killian, Lorenz Willmann, David Landhuis, Stephen C Moss, Daniel Kleppner, and Thomas J Greytak. Bose-einstein condensation of atomic hydrogen. *Physical Review Letters*, 81(18):3811, 1998.

[21] Cl C Bradley, CA Sackett, JJ Tollett, and Randall G Hulet. Evidence of bose-einstein condensation in an atomic gas with attractive interactions. *Physical review letters*, 75(9):1687, 1995.

[22] Giovanni Modugno, Giacomo Roati, Francesco Riboli, Francesca Ferlaino, Robert J Brecha, and Massimo Inguscio. Collapse of a degenerate fermi gas. *Science*, 297(5590):2240–2243, 2002.

[23] Tino Weber, Jens Herbig, Michael Mark, Hanns-Christoph Nagerl, and Rudolf Grimm. Bose-einstein condensation of cesium. *Science*, 299(5604):232–235, 2003.

[24] Mingwu Lu, Nathaniel Q Burdick, Seo Ho Youn, and Benjamin L Lev. Strongly dipolar bose-einstein condensate of dysprosium. *Physical review letters*, 107(19):190401, 2011.

[25] K Aikawa, A Frisch, M Mark, S Baier, A Rietzler, R Grimm, and F Ferlaino. Bose-einstein condensation of erbium. *Physical review letters*, 108(21):210401, 2012.

[26] ET Davletov, VV Tsyganok, VA Khlebnikov, DA Pershin, DV Shaykin, and AV Akimov. Machine learning for achieving bose-einstein condensation of thulium atoms. *Physical Review A*, 102(1):011302, 2020.

[27] Yosuke Takasu, Kenichi Maki, Kaduki Komori, Tetsushi Takano, Kazuhito Honda, Mitsutaka Kumakura, Tsutomu Yabuzaki, and Yoshiro Takahashi. Spin-singlet bose-einstein condensation of two-electron atoms. *Physical Review Letters*, 91(4):040404, 2003.

[28] Yuki Miyazawa, Ryotaro Inoue, Hiroki Matsui, Gyohei Nomura, and Mikio Kozuma. Bose-einstein condensation of europium. *arXiv preprint arXiv:2207.11692*, 2022.

[29] Lauriane Chomaz, Igor Ferrier-Barbut, Francesca Ferlaino, Bruno Laburthe-Tolra, Benjamin L Lev, and Tilman Pfau. Dipolar physics: A review of experiments with magnetic quantum gases. *arXiv preprint arXiv:2201.02672*, 2022.

[30] Axel Griesmaier, Jörg Werner, Sven Hensler, Jürgen Stuhler, and Tilman Pfau. Bose-einstein condensation of chromium. *Physical Review Letters*, 94(16):160401, 2005.

[31] JL Ville, Tom Bienaimé, R Saint-Jalm, Laura Corman, Monika Aidelsburger, Lauriane Chomaz, Katharina Kleinlein, David Perconte, Sylvain Nascimbène, Jean Dalibard, et al. Loading and compression of a single two-dimensional bose gas in an optical accordion. *Physical Review A*, 95(1):013632, 2017.

[32] William D Phillips and Harold Metcalf. Laser deceleration of an atomic beam. *Physical Review Letters*, 48(9):596, 1982.

[33] S Weyers, E Aucouturier, C Valentin, and N Dimarcq. A continuous beam of cold cesium atoms extracted from a two-dimensional magneto-optical trap. *Optics Communications*, 143(1-3):30–34, 1997.

[34] K Dieckmann, RJC Spreeuw, M Weidemüller, and JTM Walraven. Two-dimensional magneto-optical trap as a source of slow atoms. *Physical Review A*, 58(5):3891, 1998.

[35] TG Tiecke, SD Gensemer, A Ludewig, and JTM Walraven. High-flux two-dimensional magneto-optical-trap source for cold lithium atoms. *Physical Review A*, 80(1):013409, 2009.

[36] Giacomo Lamporesi, Simone Donadello, Simone Serafini, and Gabriele Ferrari. Compact high-flux source of cold sodium atoms. *Review of Scientific Instruments*, 84(6):063102, 2013.

[37] Sören Dörscher, Alexander Thobe, Bastian Hundt, André Kochanke, Rodolphe Le Targat, Patrick Windpassinger, Christoph Becker, and Klaus Sengstock. Creation of quantum-degenerate gases of ytterbium in a compact 2d-/3d-magneto-optical trap setup. *Review of Scientific Instruments*, 84(4):043109, 2013.

[38] Ingo Nosske, Luc Couturier, Fachao Hu, Canzhu Tan, Chang Qiao, Jan Blume, YH Jiang, Peng Chen, and Matthias Weidemüller. Two-dimensional magneto-optical trap as a source for cold strontium atoms. *Physical Review A*, 96(5):053415, 2017.

[39] Ian Baker. Rare earth magnets. In *Fifty Materials That Make the World*, pages 187–194. Springer, 2018.

[40] DR Lide. *Properties of ice and supercooled water CRC Handbook of Chemistry and Physics.* Boca Raton, FL: CRC Press, 2007.

[41] John Emsley. *Nature's building blocks: an AZ guide to the elements.* Oxford University Press, 2011.

[42] Mary Elvira Weeks. *Discovery of the Elements.* 1968.

[43] Chayma Bouazza. *Ultracold dysprosium gas in optical dipole traps: control of interactions between highly magnetic atoms.* Ph.d. thesis, PSL Research University, 2018.

[44] WC Martin, Romuald Zalubas, and Lucy Hagan. Atomic energy levels-the rare earth elements.(the spectra of lanthanum, cerium, praseodymium, neodymium, promethium, samarium, europium, gadolinium, terbium, dysprosium, holmium, erbium, thulium, ytterbium, and lutetium).[66 atoms and ions]. Technical report, Manchester Coll. of Science and Technology (UK). Dept. of Chemistry, 1978.

[45] J Ferch, W Dankwort, and H Gebauer. Hyperfine structure investigations in dyi with the atomic beam magnetic resonance method. *Physics Letters A*, 49(4):287–288, 1974.

[46] Davide Dreon. *Designing and building an ultracold Dysprosium experiment : a new framework for light-spin interaction.* Ph.d. thesis, Université Paris sciences et lettres, July 2017.

[47] Philipp Ilzhöfer. *Creation of Dipolar Quantum Mixturesof Erbium and Dysprosium.* Ph.d. thesis, University of Innsbruck, 2020.

[48] Mingwu Lu, Seo Ho Youn, and Benjamin L Lev. Spectroscopy of a narrow-line laser-cooling transition in atomic dysprosium. *Physical Review A*, 83(1):012510, 2011.

[49] Mingwu Lu, Seo Ho Youn, and Benjamin L. Lev. Trapping ultracold dysprosium: A highly magnetic gas for dipolar physics. *Phys. Rev. Lett.*, 104:063001, Feb 2010.

[50] CB Alcock, VP Itkin, and MK Horrigan. Vapour pressure equations for the metallic elements: 298–2500k. *Canadian Metallurgical Quarterly*, 23(3):309–313, 1984.

[51] M.J. Winter. Dysprosium: radii of atoms and ions, 1993.

[52] George Karniadakis, Ali Beskok, and Narayan Aluru. *Microflows and nanoflows: fundamentals and simulation*, volume 29. Springer Science & Business Media, 2006.

[53] Wikipedia. Lambert's cosine law — Wikipedia, the free encyclopedia. `http://en.wikipedia.org/w/index.php?title=Lambert's%20cosine%20law&oldid=1101304627`, 2022. [Online; accessed 23-August-2022].

[54] W. Steckelmacher. Knudsen-flow 75 years on - the current state-of-the-art for flow of rarefied-gases in tubes and systems. *Reports on Progress in Physics*, 49(10):1083–1107, 1986. F6380 Times Cited:90 Cited References Count:191.

[55] Donald R Olander and Valerie Kruger. Molecular beam sources fabricated from multichannel arrays. iii. the exit density problem. *Journal of Applied Physics*, 41(7):2769–2776, 1970.

[56] J. A. Giordmaine and T. C. Wang. Molecular beam formation by long parallel tubes. *Journal of Applied Physics*, 31(3):463–471, 1960.

[57] D. R. Olander, R. H. Jones, and W. J. Siekhaus. Molecular beam sources fabricated from multichannel arrays. iv. speed distribution in the centerline beam. *Journal of Applied Physics*, 41(11):4388–4391, 1970.

[58] H. C. W. Beijerinck and N. F. Verster. Velocity distribution and angular distribution of molecular beams from multichannel arrays. *Journal of Applied Physics*, 46(5):2083–2091, 1975.

[59] Eric L Raab, Mara Prentiss, Alex Cable, Steven Chu, and David E Pritchard. Trapping of neutral sodium atoms with radiation pressure. *Physical review letters*, 59(23):2631, 1987.

[60] W Wohlleben, Frédéric Chevy, K Madison, and Jean Dalibard. An atom faucet. *The European Physical Journal D-Atomic, Molecular, Optical and Plasma Physics*, 15(2):237–244, 2001.

[61] Paul D Lett, William D Phillips, SL Rolston, Carol E Tanner, RN Watts, and CI Westbrook. Optical molasses. *JOSA B*, 6(11):2084–2107, 1989.

[62] James M Kohel, Jaime Ramirez-Serrano, Robert J Thompson, Lute Maleki, Joshua L Bliss, and Kenneth G Libbrecht. Generation of an intense cold-atom beam from a pyramidal magneto-optical trap: experiment and simulation. *JOSA B*, 20(6):1161–1168, 2003.

[63] Wolfgang Demtröder. *Atoms, molecules and photons*, volume 3. Springer, 2010.

[64] Matteo Barbiero. *Novel techniques for a strontium optical lattice clock*. PhD thesis, PhD thesis, Polytechnic University of Turin, 2019.

[65] Thomas Middelmann, Christian Lisdat, Stephan Falke, Joseph S. R. Vellore Winfred, Fritz Riehle, and Uwe Sterr. Tackling the blackbody shift in a strontium optical lattice clock. *IEEE Transactions on Instrumentation and Measurement*, 60(7):2550–2557, 2011.

[66] Christian Gölzhäuser. *Building a new Dy quantum gas experiment*. Bachelor's thesis, 2021.

[67] Faebian Bastiman. Essential maintenance: how to tighten a CF flange. `https://faebianbastiman.wordpress.com/2014/02/02/mbe-maintenance-how-to-tighten-a-cf-flange/`, 2014. [Online; accessed 23-August-2022].

[68] Joschka Schöner. *Magnetic-Field Setup for Magneto-Optical-Trapping and Interaction-Tuning in Novel Dysprosium Quantum Gas Experiment*. Master's thesis, 2022.

[69] Lennart Hoenen. *Fast, High Precision Low Noise Bipolar Power Supply for Magnetic Field Coils in Ultra-Cold Dysprosium Experiment*. Bachelor's thesis, 2022.

[70] WN Charman. Wavefront technology: past, present and future. *Contact Lens and Anterior Eye*, 28(2):75–92, 2005.

[71] Eric D Black. An introduction to pound–drever–hall laser frequency stabilization. *American journal of physics*, 69(1):79–87, 2001.

[72] F. James. Monte carlo theory and practice. *Reports on Progress in Physics*, 43(9):1145–1189, 1980.

[73] George Casella, Christian P Robert, and Martin T Wells. Generalized accept-reject sampling schemes. *Lecture Notes-Monograph Series*, pages 342–347, 2004.

[74] Philipp OJ Scherer. *Computational Physics*. Springer, 2010.

[75] Johannes Schindler. *Characterization of an Erbium Atomic Beam.* Master's thesis, University of Innsbruck, 2011.

[76] Julian Kluge. *Design of a Zeeman slower for asecond generation experimentalsetup on quantum degenerate Dysprosium gases.* Master's thesis, Universität Stuttgart, 2019.

[77] D. Cotter. Stimulated brillouin scattering in monomode optical fiber. *Journal of Optical Communications*, 4(1), 1983.

[78] Michalis N. Zervas and Christophe A. Codemard. High power fiber lasers: A review. *IEEE Journal of Selected Topics in Quantum Electronics*, 20(5):219–241, 2014.

[79] Tobias Hammel. *Design and Construction of a New Experiment for Programmable Quantum Simulation using Ultracold 6Li Fermions.* Master's thesis, 2021.

[80] Samuel Saskin, JT Wilson, Brandon Grinkemeyer, and JD Thompson. Narrowline cooling and imaging of ytterbium atoms in an optical tweezer array. *Physical review letters*, 122(14):143002, 2019.

[81] William Lunden, Li Du, Michael Cantara, Pierre Barral, Alan O Jamison, and Wolfgang Ketterle. Enhancing the capture velocity of a dy magneto-optical trap with two-stage slowing. *Physical Review A*, 101(6):063403, 2020.

[82] Bojeong Seo, Peng Chen, Ziting Chen, Weijun Yuan, Mingchen Huang, Shengwang Du, and Gyu-Boong Jo. Efficient production of a narrow-line erbium magneto-optical trap with two-stage slowing. *Physical Review A*, 102(1):013319, 2020.

C │ Acknowledgment

At the end of this thesis, I would like to say thank you to a few people, who have supported me after I arrived at Heidelberg and made this thesis possible.

First of all, with all my sincerity and heart I would like to thank my supervisor Prof. Dr. Lauriane Chomaz for not only giving me this great opportunity to join her group but also for her excellent and patient supervision at any time. I've never forgotten the time she helped me correct all the bugs in my simulation and enriched my shallow understanding of physics step by step. Her wisdom, patience, and tolerance are the flames in dark encouraging me to explore the most interesting knowledge. Apart from science, I would like to greatly thank her for organizing and holding all the group parties, where I experienced the most wonderful time and learned so much about the culture of this charming land. Together with the other people in our group, she makes it a great privilege and joy to study in the Quantum Fluids group at Heidelberg University. Last, I must give a special and huge thanks to Lauriane for her additional efforts in training my English speaking, writing, and presentation. Thanks also to my co-supervisors Prof. Dr. Selim Jochim and Prof. Dr. Matthias Weidemüller, who gives us lots of important inspiration at many crucial moments. A great thanks to Dr. Shuwei Jin, who contributed so much to building our new experiment platform and taught me plenty of knowledge and skills. His rich experience and unquenchable passion are our secrets to success. Additionally, I would like to thanks Dr. Shuwei Jin again for inviting us to the *JiuMei* restaurant, where we enjoyed so much unforgettable time.

I am also extremely grateful to all the other people in the Quantum Fluids group. An extreme thanks to Karthik Chandrashekara, who helped me check all the details in my simulations with great patients. He is always a reliable partner with keen insight and profound knowledge. It was and will be a pleasure to spend time in our lab with him. A huge warm hug to Christian Gölzhäuser, who helped me so much at the very beginning during designing a completely novel setup. Not only he did an outstanding job, but also he is the one I can always discuss with, share new ideas and together enjoy lunch in the sunshine. A special thank you to Joschka Schöner, who did the best magnetic coils, I believe, with Lenny Hoenen in the whole world. He is also my absolute best language pattern for English, a German food critic, and a true master of drinking. It is my honor to share a desk with him. Hereby, I wish him a nice journey in California. Tons of thanks to Valentina Salazar Silva, who always easily helps me with all the things I can not do. Her passion for life like the spring breeze inspired me deeply. Thanks to her very much for reminding me

to have lunch and attend my German classes all the time. Besides, I would like to thank her also for designing the mugs and the temple of the poster for our group, which are super pretty. Sincere gratitude should also go to Lennart Hoenen, who contributed four of the most stable power supplies in the world besides coils, and Paul Holzenkamp, who is always our organizer for going to lunch. And many thanks also go to Prachi Nagpal and Britta Bader for the time we spent together.

A very special thank goes to Lauriane and Joschka, which is worth a single paragraph, for guiding me to drink by ordering four cases of beer.

I would like to thank the LiCs group in Heidelberg, especially Binh Tran, Manuel Gerken, and Eleonora Lippi, who are also my first friends in Germany. Thanks for sharing the office with me in my first several months. I've never forgotten the time we stayed together and the help from you. Also, many thanks go to Michael Rautenberg for lending me the computer at my start and Tobias Krom for lending me all the special tools and fibers timely. I would like to thank as well as The HQA group, who is our neighbor and helped me a lot. Many thanks go to Tobias Hammel for discussing and sharing the information about 2D-MOT. Lots of thanks should also go to Guoxian Su and Zhaoyu Zhou in Pan's group, who lend us the vacuum pumps and so many small but super useful stuff. I would like to also thank everyone in the mechanical and electronic workshop for helping us build our setup, everyone in the post office and Dr. Maarten DeKieviet for taking care of the order, and Mr. Stephan Sanchez Deckert for drilling holes and installing the whiteboard.

I especially and greatly thank the Max Planck Institute for Nuclear Physics (MPIK) and the International Max Planck Research School for providing the funding for my study. And I would like also to thank all the people from there for helping me all the time. Many thanks should also go to all my friends in MPIK. With limited space, please forgive I can not mention all your names here.

I would like to also thank all the people who helped me in my life. First thanks to my parents for bringing me up. Without them, I won't be the person I am today. I would like also to thank all the professors at Nankai University, who took care of my start in physics, especially my first supervisor Prof. Dr. Qiang Wu. Last, I would like to say thanks to my classmate from junior high school, my soul friend, and my love, Ms. Weiyu Zhang. It was and will always be my pleasure and honor to experience and enjoy a colorful life with you.

Erklärung:

Ich versichere, dass ich diese Arbeit selbstständig verfasst habe und keine anderen als die angegebenen Quellen und Hilfsmittel benutzt habe.

Heidelberg, den 06. October 2022

Jianshun Gao